

## An investigation into the formation of squats in rails: modelling, characterization and testing

Naeimi, M.

**DOI**

[10.4233/uuid:21922fff-e385-4de1-9957-8423221ef5a0](https://doi.org/10.4233/uuid:21922fff-e385-4de1-9957-8423221ef5a0)

**Publication date**

2020

**Citation (APA)**

Naeimi, M. (2020). *An investigation into the formation of squats in rails: modelling, characterization and testing*. [Dissertation (TU Delft), Delft University of Technology]. <https://doi.org/10.4233/uuid:21922fff-e385-4de1-9957-8423221ef5a0>

**Important note**

To cite this publication, please use the final published version (if applicable). Please check the document version above.

**Copyright**

Other than for strictly personal use, it is not permitted to download, forward or distribute the text or part of it, without the consent of the author(s) and/or copyright holder(s), unless the work is under an open content license such as Creative Commons.

**Takedown policy**

Please contact us and provide details if you believe this document breaches copyrights. We will remove access to the work immediately and investigate your claim.

# An investigation into the formation of squats in rails: modelling, characterization and testing



**AN INVESTIGATION INTO THE FORMATION OF SQUATS IN RAILS:  
MODELLING, CHARACTERIZATION AND TESTING**

**Meysam Naeimi**

# **An investigation into the formation of squats in rails: modelling, characterization and testing**

**Dissertation**

for the purpose of obtaining the degree of doctor  
at Delft University of Technology  
by the authority of the Rector Magnificus Prof.dr.ir. T.H.J.J. van der Hagen,  
chair of the Board for Doctorates  
to be defended publicly on  
Wednesday 28 October 2020 at 10:00 o'clock

by

**Meysam NAEIMI**

Master of Science, Railway Track Engineering  
Iran University of Science and Technology, Iran  
born in Tehran, Iran

This dissertation has been approved by the promotor.

Composition of the doctoral committee:

Rector Magnificus,	chairperson
Prof.dr. Z. Li	Delft University of Technology, promotor
Prof.dr.ir. R.P.B.J. Dollevoet	Delft University of Technology, promotor

Independent members:

Prof.dr.ir. J. Sietsma	Delft University of Technology
Prof.dr. H. Li	University of Wollongong, Australia
Prof.dr. D. Fletcher	University of Sheffield, UK
Prof.dr.ir. R. Wolfert	Delft University of Technology
Dr. A. Núñez Vicencio	Delft University of Technology
Prof.dr. M.J. Santofimia Navarro	Delft University of Technology, reserve member



This doctoral research has been part of an ExploRail project, namely, Development of High-Performance Rail through Intelligent Metallurgy and Engineering (PRIME), which was conducted at Delft University of Technology. This project (Code: 11247) is funded by Dutch rail infra manager ProRail and the Netherlands organization for scientific research (STW/NWO).

**Keywords:** wheel-rail contact, squat, test rig, impact, thermomechanical modelling, finite element method, CT scan, crack detection, 3D visualization, crack geometry

Printed by: Gildeprint – Enschede

Cover by: Meysam Naeimi

Copyright © 2020 by Meysam Naeimi (meysam\_naeimi@yahoo.com)

ISBN: 978-94-6366-326-7

An electronic version of this dissertation is available at

<http://repository.tudelft.nl>

*Dedicated to*  
*My parents, my wife Sara and my children Ryan and Adrian*

هدیه به پدر و مادرم، همسرم سارا و فرزندانم رایان و آدریان



## Acknowledgment

Performing this doctoral research was only possible thanks to the support of my friends, colleagues and collaborators. I would like to start by thanking my promoter Prof. Zili Li who has also been my daily supervisor during the entire PhD research. I am deeply grateful to him for his supportive attitude, sharp ideas, technical assistance and constant guidance during the past years. He offered me a valuable opportunity to do research on various aspects surrounding my thesis, e.g. laboratory testing, field measurements and modelling. I would also like to thank my copromoter Prof. Rolf Dollevoet for his constant support, inspiring words and technical feedbacks. His suggestions were always constructive and his attitude on offering a world-class research and education in the field of Railway Engineering in the TU Delft was impressive.

I would also like to appreciate people who were involved in the PRIME project, especially Prof. Jilt Sietsma, Prof. Roumen Petrov, Frédéric Fau and Dr. Jun Wu for their close cooperation, valuable feedbacks, and fruitful outputs. This project (PRIME) was funded by Dutch rail infra manager ProRail and the Netherlands organization for scientific research (STW/NWO); their support is greatly acknowledged. PRIME was a great opportunity to experience teamwork in a high-quality project environment and to learn more about other disciplines relevant to my research field e.g. metallography, microstructural observations and lab techniques.

I appreciate Jan Moraal, Steve van Herk and Giel Hermans who have contributed a lot to the design, construction, tuning, validating and initializing of the new test setup in the CITG lab. My sincere gratitude to Dr. Alfredo Núñez and Shaoguang Li who helped me improve the quality of my research and publications.

Many thanks to Ali Jamshidi and Omid Hajizad for being my colleague and good friends during the past years and for having many lunch and tea discussions together about life and research; also thanks for the wonderful journey together to China for the Beijing Summer School. With Ali, I have an unspoken agreement to laugh together for the rest of our life.

I am grateful to other colleagues and employees at the Railway Engineering group of CITG, TU Delft, among them, Dr. Michaël Steenbergen, Dr. Valeri Markine, Dr. Emile van der Heide, Jacqueline Baarnhoorn, Ellard Groenewegen, Joris van Dijk, Maider Oregui, Chang Wan, Nico Burgelman, Yuewei Ma, Siamak Hajizadeh, Xiangyun Deng, Chen Shen, Zhen Yang, Zilong Wei, Haoyo Wang, Xiangming Liu, Lizuo Xin, Siamand Rahimi, Hongrui Wang, Pan Zhang, Evert van Veldhuizen, Harm Visser, Behzad Naeinian, Jurjen Hendriks, Maha Messaadi, Mehran Sadri, Zhiwei Qian, Ling Chang and Anthonie Boogaard. We spent unforgettable moments together and it was my great pleasure to work with you all during my PhD at TU Delft.

The support from ProRail especially from Chris Verstegen, Bart Schotsman, Arjen Zoeteman, Sytse Bisschop, Chris Nunez Sosa, Coen Valkenburg, Alf Smolders, Brenda Struve and Manon Kiers is much appreciated especially for discussions about the results of my research in the progress meetings of ExploRail projects.

My sincere gratitude goes out to my former colleagues at Royal HaskoningDHV and DEKRA Rail, among them, Niels van der Hoog, Dirk van der Meer, Christiaan Eisma (who checked my Dutch summary of the thesis), Daan Verbruggen, Tarik Yajeb, Eva Italiaander, Roderik Mennens, Mark Linders, Martin Hiensch, Pieter Dings, Soheil Rostami and Rob van Bruchem for giving inspiration and motivation about my research specially in the last stage of my PhD work. I appreciate my current colleague Femke Skirving at Inspectie Leefomgeving



en Transport (ILT) for trust and encouragement on joining ILT, considering the fact that I was about to receive a doctoral degree from the TU Delft.

Further, I would like to appreciate the experienced railway specialists in the Dutch railway industry who were often present for open discussions especially during the monthly colloquiums at the TU Delft, among them, Ruud van Bezooijen, Greg Lambert, Gerard van der Werf and Dr. Amy De Man.

The support from the friends, whom I met within the initial years in the Netherlands, is kindly acknowledged. For them, there is a long list, however, I would like to selectively mention Mohammad Mohajeri, Sadegh Akbarnejad, Hamid Saeedi, Erfan Hoseini, Somayeh Lotfi, Fatemeh Anisi, Afshin Jalali Sohi and Hussein Farahani as some of those friendly and helpful individuals.

I must express my very deep gratitude to my parents for the loving upbringing and the constant support and encouragement. My greatest gratitude goes to my wife Sara for her spiritual support during my PhD work and while establishing in the Netherlands. My children Ryan and Adrian, who were both born during my PhD in the Netherlands, one day will be able to read this text (when they go to school). I have occasionally spent our free time working on my thesis, the time that normally belonged to the family; thank you for allowing that.

Last, but not least, Hossein (Daniel) Saket, killed together with 175 other innocents in the plane crash Flight 752, rest in peace, my friend; your good memories will remain in my heart.

Meysam Naeimi

September, 2020

The Netherlands

# Contents

Acknowledgment .....	v
Summary .....	xi
Samenvatting .....	xiii
Chapter 1 Introduction .....	1
1.1 Rolling contact fatigue in wheels and rails .....	1
1.2 Problem statement.....	2
1.2.1 Thermomechanical modelling .....	3
1.2.2 Testing method .....	3
1.2.3 Characterization technique .....	4
1.3 Research questions.....	4
1.4 Research approach .....	5
1.4.1 Thermomechanical modelling of the wheel–rail contact .....	5
1.4.2 A new test setup for testing the wheel–rail contact system.....	5
1.4.3 A new technique for early detection of rail squats .....	5
1.5 Dissertation outline .....	5
1.6 References.....	6
Chapter 2 A new modelling tool for thermomechanical analysis of the wheel–rail contact	9
2.1 Introduction.....	10
2.2 Thermomechanical modelling of the wheel–rail contact.....	11
2.2.1 Thermomechanical coupling .....	13
2.2.2 Mechanical solver.....	13
2.2.3 The thermal solver .....	14
2.2.4 Thermomechanical parameters.....	15
2.3 Results of numerical simulations .....	18
2.3.1 Thermomechanical stresses .....	18
2.3.2 Temperature results .....	20
2.4 Discussion.....	23
2.4.1 Potential of martensitic transformation at supercritical temperatures .....	23
2.4.2 Potential of fatigue at subcritical temperatures .....	24

2.5	Conclusions.....	26
2.6	References.....	27
Chapter 3	A new test rig for experimental study of the wheel–rail contact .....	31
3.1	Introduction.....	32
3.2	Review of the existing test rigs for wheel–rail contact studies.....	33
3.2.1	High–frequency vibrations .....	34
3.2.2	Details down to track components .....	35
3.2.3	Scaling concept.....	35
3.2.4	The ring track mechanism .....	36
3.3	Development of the new rig under the selected category.....	37
3.3.1	Scalability in the new test rig .....	37
3.3.2	Numerical modelling of the wheel–rail contact in the new test rig.....	39
3.3.3	Numerical modelling of the rail bending in the new test rig.....	40
3.4	Summary of the comparisons and final choice for the test rig .....	42
3.4.1	Rail track stability.....	42
3.4.2	Analogy of loading conditions to the actual railway.....	42
3.4.3	Final choice for the test rig.....	43
3.4.4	Description of the new test rig.....	45
3.5	FE modelling and experiments using the newly–built test rig.....	46
3.5.1	FE modelling with squat defect.....	46
3.5.2	FE modelling and experiments of the rail joint.....	47
3.5.3	Scalability of track dynamic characteristics by impact measurements .....	49
3.6	Conclusions.....	51
3.7	References.....	52
Chapter 4	A new characterization procedure for reconstructing RCF defects based on computed tomography.....	57
4.1	Introduction.....	58
4.1.1	Computed tomography vs. ultrasonic and eddy current measurement.....	58
4.1.2	CT vs. SEM, TEM and EBSD.....	59
4.1.3	Relevant history of CT technology.....	60
4.2	Sample preparation .....	60
4.3	CT scan settings .....	62
4.4	Collection and process of the CT scan data.....	64
4.4.1	Crack reconstruction in the moderate squat .....	66
4.4.2	Crack reconstruction in the light squat.....	68
4.4.3	Crack reconstruction in the baby squat .....	70
4.5	Validation.....	71

4.5.1 The moderate squat.....	71
4.5.2 The light squat .....	73
4.5.3 The baby squat.....	73
4.6 Discussion.....	74
4.7 Conclusions.....	76
4.8 References.....	77
Chapter 5 Determining the angles of squat cracks using CT scanning and metallographic observations .....	79
5.1 Introduction.....	80
5.2 Measuring squat crack angles that are formed at the rail surface .....	81
5.2.1 Definitions and conventions on the crack plane and crack angles .....	83
5.2.2 Measurement of the crack angles in various squats .....	84
5.3 Calculation of crack angles by numerical modelling.....	90
5.3.1 Finite element modelling.....	90
5.3.2 Fatigue initiation criteria .....	91
5.3.3 Results of numerical simulations.....	93
5.4 Discussion.....	94
5.4.1 Categorization of the crack planes into orientations .....	94
5.4.2 Order of crack initiation in multiple cracks.....	97
5.4.3 Numerical results compared to measured crack angles.....	98
5.5 Conclusions.....	99
5.6 References.....	100
Chapter 6 Conclusions and recommendations .....	105
6.1 Conclusions.....	105
6.2 Recommendations.....	108
Curriculum Vitæ.....	111
List of Publications.....	113



## Summary

Rolling contact fatigue (RCF) is an important form of damage in wheels and rails that typically has surface and subsurface cracks. Squats are one of the major RCF defects that occur in the running band of rails and can create high dynamic forces and cause rail fracture if they are not detected and treated in time. In the current research, three advanced methods are developed in order to obtain a better understanding of the formation mechanism of RCF defects and, especially, squats in rails: 1) A new thermomechanical tool for numerically modelling the wheel–rail contact, 2) A new experimental setup for physically simulating the wheel–rail interaction and 3) A new computed tomography (CT) procedure for characterizing the wheel–rail defects.

The first research presents a coupled thermomechanical modelling procedure for the wheel–rail contact problem and computes the flash–temperature and stress–strain responses when thermal effects are included. The contact temperature and thermal stresses could be driving factors for squats initiation. A three–dimensional (3D) elasto–plastic finite element model is built considering the wheel–track interaction. When the wheel is running on the rail, frictional energy is generated in the contact interface. The model is able to convert this energy into heat by using a coupled thermomechanical approach. To evaluate the contribution of thermal effects and plasticity, five different material models, i.e., linear elastic (E), elasto–plastic (EP), elastic thermal (ET), thermo–elasto–plastic (TEP) and thermo–elasto–plastic with thermal softening (TEPS), are built up. The numerical models calculate the flash–temperature and thermomechanical stresses in the wheel and rail. Discussions are made on the effects of the solution types (pure mechanical vs. thermomechanical coupling) and of material types (elastic vs. nonlinear, temperature–independent vs. thermal–softening). The rail temperature is calculated for a critical case caused by severe friction and creepage. The results are used to investigate the potential of white etching layer (WEL) formation via martensitic phase transformation. The WEL formation is often reported to be associated with rail squats. The temperature calculated for this case (756°C) was higher than the critical temperature needed to transform pearlite to austenite (700°C). It was concluded that martensitic phase transformation is a likely behaviour under the high creepage that causes supercritical temperature. Thermal effects were also found to be important in lower creepage cases, where subcritical temperatures occurred (below 700°C). The results indicated a synchronization effect, i.e., the lower yielding limits and higher stresses, which can cause earlier fatigue initiation.

In the second research, a new downscale test setup is designed and built for investigating the interaction between wheel and rail, especially under impact–like loading conditions, which are supposed to be often associated with rail squats. The test rig is intended to remedy the lack of dynamic similarity between the actual railway and the existing laboratory testing capability, by considering the factors that contribute to high–frequency dynamics of the wheel–track system. This part of the thesis first reviews the functionalities of the existing test techniques in the literature. Based on this survey, the category of the scaled wheel on the rail track ring is chosen. Afterwards, three potential alternatives are identified and an optimum mechanism is arrived at through finite element modelling and analysis of the structures. This leads to downscale test rig, consisting of multiple wheels running over a horizontal rail track ring. The new test rig is a unique experimental setup due to the inclusion of high–frequency dynamic vibrations in the wheel–track system and analogy of the incorporated elements and loading–response relation to those of the real–life system. This part of the thesis further presents the results of some experiments carried out using the newly–built setup to verify the ideas behind its development. One of the results is that several potential

corrugation wave patterns were observed on the railhead, which are considered to be induced by the impact due to the rail joints. These wave patterns are in good agreement with those of the real-life systems. Using transient finite element modelling, it is confirmed that the new test rig can reproduce the high-frequency dynamic characteristics of the wheel-track system when a typical w-shape squat is present on the railhead.

The third research presents the development of a computed tomographic (CT) scanning technique to reconstruct the 3D geometry of the RCF cracks in the railhead. Squat defects are associated with complex crack networks at the subsurface. Sample rails having squats of different severities are taken from the Dutch railway network. Four specimens of different sizes are prepared and investigated with the CT scanner. A detailed procedure of the CT experiment and post-processing is described. A sequence of high-quality X-ray images are collected during each scan. These 2D images are combined to construct the 3D visualization of the specimens. Various image processing tools are applied to extract and rebuild the internal crack geometries, thus allowing the crack networks to be differentiated from the bulk steel. For validation, the CT results are compared with metallographic observations of the rail surface for all the defects and with those of vertical sectioning. Discussions are made regarding the proper size of the rail samples in relation to severity of the squats. According to the results, CT allows for a 3D visualization of RCF defects, providing high-quality data on the geometry of the internal cracks. By choosing the appropriate settings and specimen size, CT can accurately reconstruct the squat cracks at different growth stages. This research shows the potential of the CT technique as an intermediate detection and characterization tool between the methods for characterizing macro cracks and those for characterizing micro/nano cracks. A practical specimen design and a detailed scanning procedure are proposed.

The proposed 3D visualization method, together with the necessary geometric definitions, is then used for enabling effective measurement and characterization of the squat cracks. It is used to determine the angles  $\theta_1$ ,  $\theta_2$ , and  $\theta_3$  that squat crack faces form with respect to three orthogonal planes: the rail top, the longitudinal-vertical cross-section and the lateral-vertical cross-section. It is found that the cracks can be characterized by four orientations T1 – T4. The variation ranges of the crack angles are determined for each orientation that fall in  $132^\circ \leq \theta_1 \leq 150^\circ$ ,  $6^\circ \leq \theta_2 \leq 36^\circ$  and  $67^\circ \leq \theta_3 \leq 81^\circ$ . By investigating the occurrence frequency of the orientations, it is found that T4 and T1 together form the primary V-shaped cracks of the squats, and T2 and T3 together form the secondary V-shaped cracks. The findings agree with previous field monitoring results that were reported in the literature. The angle types also appeared to be related to the loading conditions.

Based on this research, the main new insights into the formation of rail squats are as follows: i) the WEL formation via martensitic phase transformation turns out to be possible; this is confirmed through the thermomechanical wheel-rail contact modelling; ii) the impact-like loading conditions and high-frequency dynamic characteristics of the wheel-track system appear to be essential for the squat formation; this is confirmed through the vehicle-track testing using the new test rig; and iii) the occurrence of different crack orientations followed by the primary and secondary V-shaped cracks turns out to be important in the squat formation; this is confirmed through the CT scanning and metallographic observations.

## Samenvatting

Rollende contact moeheid (RCF) is een belangrijke vorm van schade aan de wielen en spoorstaven. Het veroorzaakt meestal oppervlaktescheuren en diepe scheuren. Squats zijn een van de belangrijkste RCF-defecten die zich in het loopvlak van de spoorstaven bevinden en kunnen hoge dynamische krachten en railbreuk veroorzaken als ze niet op tijd worden gedetecteerd en behandeld. In het kader van dit onderzoek zijn drie geavanceerde methoden ontwikkeld om een beter inzicht te krijgen in het vormingsmechanisme van RCF-defecten. Met name de squats in spoorstaven: 1) Een nieuwe thermomechanische berekeningsmethode voor het numeriek modelleren van het wiel-rail contact probleem, 2) Een nieuwe experimentele opstelling voor het testen van de wiel-rail interactie en 3) Een nieuwe computertomografie (CT) procedure voor het karakteriseren van de wiel-rail defecten.

Het eerste onderzoek presenteert een gecombineerde thermomechanische modellerings-procedure voor het wiel-rail contact probleem en berekent de flash (flits)-temperatuur en spanning-rek reacties van de materialen met het oog op thermische effecten. De contacttemperatuur en de thermische spanningen kunnen de oorzaak zijn van het ontstaan van de squats. Eén driedimensionaal (3D) elastoplastisch eindige-elementenmodel is gebouwd op basis van de interactie tussen het wiel en het spoor. Wanneer het wiel op het spoor loopt, wordt wrijvingsenergie gegenereerd in het contactvlak. Het model is in staat om deze energie om te zetten in warmte door middel van een gekoppelde thermomechanische benadering. Om de bijdrage van thermische effecten en plasticiteit te evalueren zijn er vijf verschillende materiaalmodellen opgebouwd, namelijk lineair elastisch (E), elastisch-plastic (EP), elastisch thermisch (ET), thermo-elasto-plastic (TEP) en thermo-elasto-plastic met thermische verzachting (TEPS). De numerieke modellen berekenen de flash-temperatuur en de thermomechanische spanningen in het wiel en de rail. Er is gediscussieerd over de effecten van diverse soorten oplossingen (uitsluitend mechanisch versus thermomechanische koppeling) en van de materiaalsoorten (elastisch versus niet-lineair, temperatuuronafhankelijkheid versus thermische zachtheid). De railtemperatuur wordt berekend voor een kritische situatie van ernstige wrijving en kruip coëfficiënt. De resultaten zijn gebruikt om het potentieel van de vorming van witte etslaag (WEL) via martensitische faseformatie te onderzoeken. De WEL-vorming wordt vaak in verband gebracht met de railsquats. De voor dit geval berekende temperatuur (756°C) was hoger dan de kritische temperatuur die nodig is om perliet naar austeniet (700°C) om te zetten.

Geconcludeerd kon worden dat het optreden van de martensitische faseformatie mogelijk veroorzaakt wordt door de hoge kruip omstandigheden en superkritische temperatuur in de spoorstaaf. Thermische effecten werden ook belangrijk bevonden in lagere kruipgevallen, waar de subkritische temperaturen (onder 700°C) voorkwamen. De resultaten wezen op een synchronisatie-effect, d.w.z. de lagere opbrengstlimieten en de hogere spanningen, die eerdere vermoeidheidsverschijnselen kunnen veroorzaken.

In het tweede deel van dit onderzoek is een nieuwe kleinschalige testopstelling ontworpen en gebouwd voor het onderzoeken van de interactie tussen wiel en rail, met name onder impact-achtige belasting condities, die vaak geassocieerd wordt met de railsquats. De testopstelling is bedoeld om het gebrek aan dynamische vergelijkbaarheid tussen het feitelijke systeem en de bestaande laboratoriumtestomgeving te corrigeren, door te kijken naar de factoren die aan de hoogfrequentiedynamica van het wiel-spoorbaansysteem bijdragen. In dit deel van het proefschrift is eerst een overzicht gegeven over de functionaliteiten van de bestaande testtechnieken uit de literatuur. Op basis van dit onderzoek is de categorie van het geschaalde wiel op een ringvormig spoor gekozen voor nader onderzoek. Vervolgens zijn drie mogelijke alternatieven geïdentificeerd en bestudeerd via de eindige elementen modellering en de analyse van de constructies. Dit heeft geleid tot een kleinschalige testopstelling, bestaande uit meerdere



wielen die over een horizontale spoorbaanring lopen. De nieuwe testopstelling is een unieke experimentele opstelling door de aanwezigheid van hoogfrequente dynamische trillingen in het railsysteem en door het kijken naar de analogie van de ingebouwde elementen en de belastingstoestanden met die van het reëel systeem. Verder zijn in dit deel van het proefschrift de resultaten van enkele experimenten die met de nieuw gebouwde opstelling zijn uitgevoerd gepresenteerd om de ideeën achter de ontwikkeling van RCF te verifiëren. Een van de resultaten was dat er verschillende potentiële golfslijtagepatronen op de spoorstaafoppervlakte zijn waargenomen, die als gevolg van de dynamische impact zijn verondersteld te worden geïnduceerd. Deze golfslijtagepatronen komen overeen met die van realiteit. Met behulp van de transiënte eindige elementen modellering is bevestigd dat de nieuwe testopstelling de hoogfrequente dynamische karakteristieken van het reëel systeem kan reproduceren o.a. wanneer er een typische w-vormig squat op de spoorstaafkop aanwezig is.

Het derde onderzoek presenteert de ontwikkeling van een computertomografische (CT) scantechniek die de 3D-geometrie van de RCF-scheuren in de spoorstaafkop kan reconstrueren. Squatdefecten worden vaak in verband gebracht met complexe scheurnetwerken op en onder de spoorstaafoppervlakte. Spoorstafmonsters met squats van verschillende defectgrootte categorieën zijn voor dit doel onttrokken van de Nederlandse spoorwegen. Vier monsters van verschillende defectgrootte zijn voorbereid en onderzocht met de CT-scanner. Een gedetailleerde procedure van het CT-experiment en de nabehandeling is beschreven. Tijdens elke scan is een reeks van hoogwaardige X-ray afbeeldingen verzameld. Deze 2D-beelden zijn gecombineerd om de 3D-visualisatie van het monster te reconstrueren. Verschillende beeld verwerkende methoden zijn toegepast om de interne scheurgeometrieën inzichtelijk tekrijgen en die opnieuw op te bouwen, waardoor scheurnetwerken van het bulkstaal worden gedifferentieerd. Voor de validatie zijn de CT-resultaten vergeleken met metallografische waarnemingen van het spooroppervlak en van verticale doorsnijdingen. Er zijn discussies over de juiste grootte van de railmonsters in relatie tot de ernst van de squats. Volgens de resultaten maakt de CT een 3D-visualisatie van de RCF-defecten mogelijk, waardoor hoogwaardige gegevens over de geometrie van de interne scheuren worden verkregen. Door de juiste instellingen en monstergrootte te kiezen, kan CT de squatscheuren in verschillende groeifasen nauwkeurig reconstrueren. Dit onderzoek toont het potentieel van de CT techniek aan als een intermediair detectie- en karakterisatiemiddel tussen de methoden voor het karakteriseren van macroscheuren en die van micro/nano scheuren. Een praktische monster opstelling en een gedetailleerde scanprocedure zijn aangedragen.

De voorgestelde 3D-visualisatiemethode, samen met de benodigde geometrische definities, zijn vervolgens gebruikt om een effectieve meting en karakterisering van de scheuren bij de railsquats mogelijk te maken. Dit is gebruikt om o.a. de hoeken  $\theta_1$ ,  $\theta_2$  en  $\theta_3$  die squatscheuren ten opzichte van de drie orthogonale vlakken vormen te bepalen: de bovenkant van de spoorstaaf, de langs-verticale doorsnede en de zijdelings-verticale doorsnede. De scheuren zijn in vier oriëntaties T1-T4 geclassificeerd. De variatiebereiken van de scheurhoeken zijn bepaald voor elke oriëntatie als volgt:  $132^\circ \leq \theta_1 \leq 150^\circ$ ,  $6^\circ \leq \theta_2 \leq 36^\circ$  en  $67^\circ \leq \theta_3 \leq 81^\circ$ . Door de verschijningsfrequentie van de oriëntaties te onderzoeken, is het vastgesteld dat T4 en T1 samen de primaire V-vormige scheuren van de squats vormen, en T2 en T3 samen de secundaire V-vormige scheuren. De bevindingen komen overeen met eerdere veldmonitoringresultaten die in de literatuur zijn vastgelegd. De hoek types/oriëntaties bleken ook verband te hebben met de belastingstoestanden.

Op basis van dit onderzoek zijn de belangrijkste nieuwe inzichten in de vorming van railsquats als volgt: i) de mogelijkheid bestaat dat WEL-vorming kan ontstaan door martensitische fasetransformatie. Dit is bevestigd door de thermomechanische wiel-rail contactmodellering; ii) de impact-achtige belastingstoestanden en hoogfrequente dynamische karakteristieken zijn van belang voor de totstandkoming van squats; dit is bevestigd met behulp van de nieuwe wiel-spoorbaan testopstelling; en iii) de aanwezigheid van verschillende scheur oriëntaties en vervolgens primaire en secundaire V-vormige scheuren zijn belangrijker voor de totstandkoming van squats; dit is bevestigd door de CT-scanning en metallografische onderzoeken.

## Chapter 1 Introduction

### 1.1 Rolling contact fatigue in wheels and rails

Railway wheels and rails are crucial parts of the train–track system and they contribute to the safe operation of railways. To meet the increasing demand on railways for higher speeds, train frequencies and loading bearing capacities, it is becoming more important to enhance the lifetime of wheel–rail materials. By improving the performance of wheel–rail materials against degradation, the maintenance and operational costs of the railways are reduced and failures and disturbances in the service are mitigated.

Rolling contact fatigue (RCF) is the major degradation mode of wheels and rails. RCF is a family of defects that occur in the surfaces and sub–surfaces of rolling elements under cyclic loading [1]. RCF is frequently observed in rolling bearings, gears, wheels and rails. For rails, this damage may appear in the surface as, e.g., head checks, spalling and squats or in the subsurface as, e.g., deep–seated shelling [1].

Figure 1.1 shows two examples of RCF defects in rails. Squats and head checks are the two main types of RCF [2]. Head checks are a sort of parallel surface cracks, occurring mostly in the gauge corner or gauge shoulder of the railhead. They are mostly seen in horizontal curves with radii of 500~3000m [2]. Squats, in contrast, are often found in tangent tracks or shallow curves, mostly in the form of isolated dark depressions in the railhead. They often have a two–lung shape footprint in the surface in their mature phase [3].

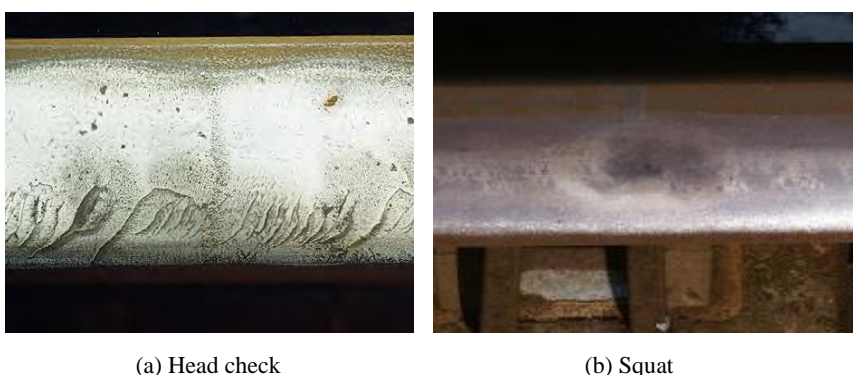


Figure 1.1. Some examples of RCF defects in rails; defect (a) is from [4] and (b) a defect in Steenwijk

The RCF problem in wheel–rail materials creates a lot of financial losses and safety issues. In general, rail defects cost around €2 billion per year around the world [5]. These costs are mainly related to the inspections, delays, remedial treatments, preventive measures, derailment and business losses.

Dutch railway is one of the most densely–used networks in Europe and its RCF–related costs are very significant. The annual costs for squat treatments were around 30 million euros

in the Netherlands, and even higher when also considering train operational costs (e.g. delays and disturbances) [6, 7]. The total treatment costs for head checks were in the order of 50 million euros per year [4].

To lower the maintenance and remedial costs associated with RCF defects, a fundamental understanding of their root causes is necessary. The initiation mechanism of rail head checks has been investigated in [2, 4, 8], where a number of preventive and remedial methods are proposed. This work [2] has proposed a systematic maintenance strategy, i.e. the combination of grinding, optimal rail profile design and suitable steel grades, that can significantly reduce the head check maintenance costs (renewals and rail replacements) [2].

In contrast to head checks, there has been less progress in understanding the initiation mechanism of rail squats. This formation process is a complex phenomenon, involving a wide range of problems, e.g. fatigue behaviour, vehicle–track dynamic interaction, impact, thermal issues and material phase transformation. Some investigations on the initiation and growth mechanism of squats have been reported in the literature. The causes of squats have been studied in [3, 9–11] using field observations, dynamic axle–box measurements and numerical predictions, where high–frequency wheel–rail interaction was identified to be a crucial factor. It is concluded in [9] that squat occurrence can be related to track short–wave irregularities such as indentations, weld and corrugations. Moreover, the growth of squats has been related to dynamic contact forces, vibration wave patterns and tangential forces [3, 10–11].

Statistics about the distribution of squats occurring in Australian railway tracks [12] has shown the frequent presence of a brittle white etching layer (WEL) on the rail surface. WEL is a martensitic hard layer on the rail surface that is often found to be related to squats. Delamination and fracture of white etching layer were thought to initiate squat cracks [13]. Squats were also observed near the white etching layer in [14]. More recently a brown etching layer was observed next to WEL, which might be related to squat initiation [15]. However, observations in [16] described some squats at a site in Australia, where no white etching layer was evident. It was concluded that such squats were initiated by the ratcheting phenomenon (cyclic plastic shear deformation of the surface layer).

The literature shows that squat formation has been a controversial subject within the field. This is even more disputable by looking at the thermal origin of squats. The martensitic structure of WEL indicates a possible thermal initiation process of squats. Thermal effects in the wheel–rail contact could considerably influence the damage mechanisms. Further research is therefore needed to understand the thermal effects on rail squats. Another problem is that the existing laboratory testing methodologies cannot reproduce the true states of contact stresses of the wheel–rail system so as to reveal the actual causality of squat defects under realistic loading conditions. Furthermore, the existing inspection and characterization techniques for non–destructive analysis of rail defects fail to detect small and shallow surface cracks associated with young squats.

Development of advanced methods for modelling, testing and characterization of squats will assist in determining the degradation causes, the formation mechanism and the growth process of such defects. The findings can be used to develop treatment strategies to avoid or delay them. The general aim of this doctoral thesis is to improve the durability of rail materials against squats by developing advanced methods required for uncovering the major causes behind their formation mechanism.

## 1.2 Problem statement

The formation mechanism of rail squats is still a complex and ambiguous phenomenon. A review of the existing literature shows a general lack of advanced methods and tools for

modelling, testing and characterization of these defects. Such demand is formulated in three major research topics as described in the following:

### *1.2.1 Thermomechanical modelling*

Thermomechanical behaviour of the wheel–rail contact originates from friction in the contact interface. Friction between wheels and rails is an important agent that provides adhesion and traction/braking possibilities for trains. On the other hand, part of the mechanical energy is dissipated by the frictional work when the train wheels run along the rail. Most of this frictional work is transformed into the frictional heat at the in–contact surfaces. The heating of wheel and rail materials can be a critical issue as it may lead to: 1) thermomechanical fatigue in wheels and rails and 2) microstructural transformations in steel materials. Temperature rise and thermal stresses due to frictional heat also have negative effects on the fatigue life of rail materials. Numerical simulations in [17] indicated that thermal loading has a significant influence on plastic strains and residual stresses at the rail surface, which can expedite the formation of RCF cracks. According to [18, 19], if thermal stresses in the sliding wheel–rail contact are superimposed on the mechanical contact stresses, the elastic and shakedown limits of the wheel and rail will be reduced, and yielding will begin at lower mechanical loads. These thermal stresses are generated in very thin surface layers of materials in contact where elevated temperature occurs [19].

Another potential problem is that the contact temperature might be so high that it causes thermally–induced phase transformation in wheel–rail steel. This phenomenon may contribute to explain the formation of squat defects. Indeed, the contact temperature and thermal stresses could be driving factors for squats initiation. To emphasize on the thermal origins of such defects, a different name “studs” has even been suggested [20].

The problem of squat formation due to thermal origins has received scant attention in the literature. Most of the modelling research in the past has focused on mechanical roots, while they have overlooked the thermal origination. Moreover, the literature has neglected the synergic way of investigating the problem by thermomechanical modelling, non–destructive characterization and experimental observations on the wheel–rail contact problem. To deal with the root causes of squat formation, a comprehensive research is needed to assess various aspects of the problem. This research examines whether the thermomechanical stress–strains and the accompanying temperature rise can cause/accelerate the formation of squats. There is a need for developing new modelling tools and experimental methods for this purpose. This dissertation focuses on the problem by the systematic use of numerical modelling and experimental developments.

### *1.2.2 Testing method*

A wide range of experimental techniques and test rigs were developed in the past for wheel–rail contact studies and RCF experiments. A brief review of various full–scale rigs is provided in [21] and similar reviews on scaled–test rigs can be found in [22, 23]. Such reviews comparatively evaluate the important aspects of the test rigs such as operational mechanisms, structures, dynamic characteristics, boundary conditions, kinetics, scaling strategies and loading mechanisms. Furthermore, critical reviews on the scale factors of the test rigs can be found in [24, 25]. A general survey on various test rigs is also reported in [26]; the main focus has been on different experimental methods for curve squeal noise problem, the introduced methods, however, can be applicable to other issues in relation to rolling contact problems.

In this thesis, it is demonstrated that the existing test setups cannot fulfil the requirements needed for testing the squats formation. A brand–new test rig developed in the present research aims to provide an innovative test facility, which enables the researchers to generate RCF of rails and wheels under scaled and controlled laboratory conditions.

With this rig we intend to provide the following four functional goals: 1) to examine the validity of the various hypotheses on damage occurrence; 2) to gain new insight into damage mechanisms from the extended viewpoint of mechanical loading and material properties at macro level and at the microstructure scale; 3) to test material performance for damage resistance and 4) to support the development of new materials and damage prediction models. The present study addresses how the new setup can fulfil the above-mentioned four functionality requirements.

### 1.2.3 Characterization technique

Non-destructive inspection tools have been used in the past for early detection and characterization of RCF defects. A comprehensive review of non-destructives methods for evaluating rail defects has been published in [27]. Traditionally, ultrasonic and eddy current detection systems are the most common inspection techniques used for non-destructive detection of rail defects. Both methods have been widely used to detect the presence of fatigue cracks or internal rail defects [5]. Despite the widespread application of ultrasonic and eddy current testing, these testing techniques have limitations in detecting rail defects, particularly at the early stage.

An alternative advanced damage reconstruction is three-dimensional (3D) EBSD [28], as well as SEM and TEM [29]. The disadvantages of SEM, TEM, and EBSD are their 1) destructiveness, 2) limited specimen dimensions, 3) tedious data collecting process, and 4) lack of information on the locations and orientations of the subsurface cracks to prepare the initial sample.

In this thesis, a computed tomographic (CT) scanning technique is developed to reconstruct the 3D geometry of the RCF cracks in the railhead. It can generate high-resolution images of the cracks at the macro, meso and micro scales for the studied squat defects. CT is shown to be able to bridge the gap between the methods for macro cracks and the methods for micro and nano cracks. When this gap is filled, one will be able to trace down the complete crack development process to allow for the study of the complete evolution process of the RCF cracks. When the complete crack geometry is reconstructed with a CT scan, a sample and cracks can be viewed and studied in any arbitrary 3D orientation, e.g., axial, transverse or normal directions. The crack dimensions and orientations can be measured accurately, including the sample geometry with internal fractures. With this information, a proper understanding of the initiation and growth mechanisms of such defects can be obtained.

## 1.3 Research questions

To understand the formation mechanism of rail squats, the following main question will be addressed in this dissertation:

*What are the root causes of the formation of rail squats?*

The following three research questions are addressed to approach the answer to the main question:

- 1) *What are the thermomechanical effects on the formation mechanism of rail squats?*
- 2) *How can a new testing setup contribute to simulate the realistic conditions of the wheel-rail system when squats occur?*
- 3) *How can we detect and characterize the squat defects using a none-destructive CT scanning technique to trace their origins?*

The first question focuses on advanced numerical modelling of the wheel-rail contact. Question 2 shows the necessity for a new experimental setup to study the wheel-rail contact

problem and especially squats. The last question concentrates on the development of a new non-destructive CT scanning procedure for the detection and characterization of squats especially at their early stage of development.

## 1.4 Research approach

Three main approaches are employed in this research to deal with the questions raised in the previous section. These approaches are the major contributions of this thesis:

### 1.4.1 *Thermomechanical modelling of the wheel–rail contact*

The first contribution is the development of a new numerical modelling tool. To understand the root causes of rail squats, a thermomechanical modelling tool is developed for a general wheel–rail contact problem. The friction and thermal behaviours of the wheel–rail system are considered in the analysis, as well as mechanical behaviours. To acquire an accurate estimation of the flash–temperature in the contact interface, the temperature–dependent elasto–plastic material properties and thermal softening are taken into account.

### 1.4.2 *A new test setup for testing the wheel–rail contact system*

The second contribution of this thesis is an experimental setup, developed for investigating the RCF problems. Generation of RCF defects in the laboratory environment is a reliable approach for uncovering their root causes. It can also assist to verify the modelling results and to discover the fundamental reasons for squats initiation.

The new downscale test rig, developed in this research, manifests the realistic contribution of impact loading conditions to the RCF phenomenon. This rig provides the possibility of generating RCF in rails and wheels under scaled and controlled laboratory conditions.

### 1.4.3 *A new technique for early detection of rail squats*

Besides the test rig, a CT scanning technique is developed in this research to characterise the shape, geometry and orientations of squat cracks in rails. A number of rail samples with squats, taken from the Dutch railway network, are studied. The CT scanning technique is used to construct 3D representation of the complex squat crack networks. The method is used to measure the angles of cracks that are associated with squats.

## 1.5 Dissertation outline

Figure 1.2 shows the general outline of this dissertation. The main body of the research is dedicated to the three advanced methods, i.e. modelling, testing and characterization.

Chapter 2 introduces the thermomechanical modelling of the general wheel–rail contact problem. A 3D elasto–plastic finite element (FE) model is developed in this chapter to study the thermomechanical effects on rail squats. The relations between thermomechanical loading and microstructural transformation in rail materials are also seen in this chapter.

The development process of a new testing facility for the RCF problem is presented in Chapter 3. The test rig is a downscale test setup for testing the wheel–track system. The chapter gives a brief overview of the relevant history of various testing strategies and reviews their functionalities. Based on this survey, an optimal operational mechanism for the new test rig is selected. The new test rig is finally built in the lab and is used for dynamic tests in this research. This chapter further presents the results of the preliminary tests carried out using the rig.

Chapter 4 is dedicated to the development of a new characterization tool for early rail squats. The technique is based on computed tomography. This technique can detect and measure the squat cracks in 3D in steels.

The CT scan technique is then used in Chapter 5 to characterise and measure the geometry and the angles of squat cracks in the railhead.

Chapter 6 summarizes the results of the previous chapters. This chapter draws the final conclusions and offers some recommendations for future works.

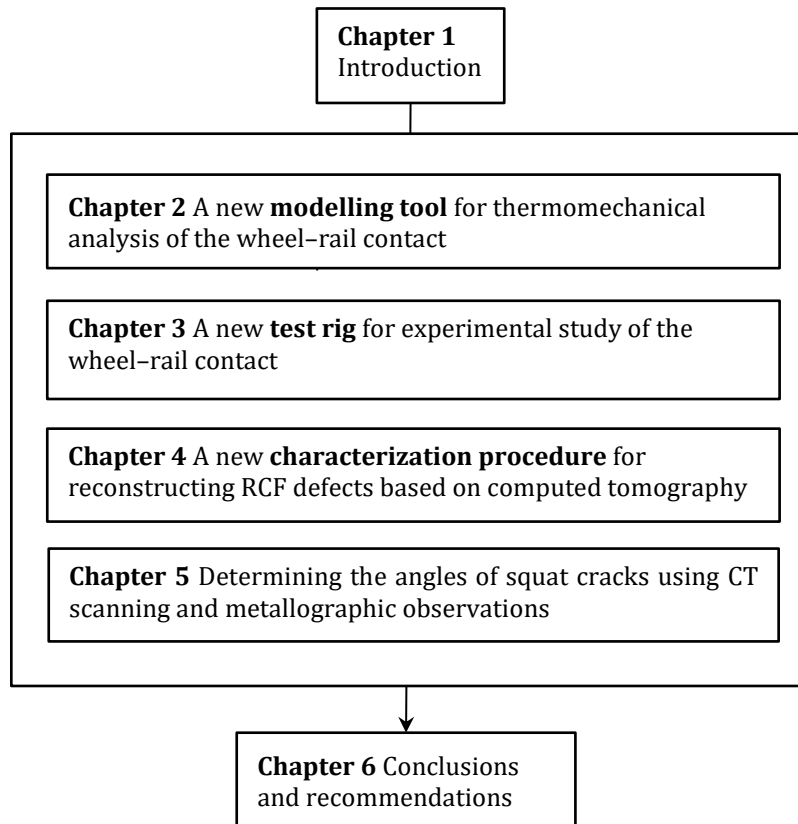


Figure 1.2. Graphical representation of the outline of this dissertation.

## 1.6 References

- [1] E. Magel, P. Sroba, K. Sawley & J. Kalousek, Control of rolling contact fatigue of rails, in: AREMA 2004 Annual Conference, Nashville, TN, USA, 2004.
- [2] A. Zoeteman, R. Dollevoet & Z. Li, Dutch research results on wheel/rail interface management: 2001–2013 and beyond. Proceedings of the Institution of Mechanical Engineers, Part F: Journal of Rail and Rapid Transit, 228–6 (2014) 642–651.
- [3] Z. Li, R. Dollevoet, M. Molodova & X. Zhao, Squat growth—Some observations and the validation of numerical predictions, *Wear*, 271 (2011) 148–157.
- [4] R.P.B.J. Dollevoet, Design of an Anti Head Check profile based on stress relief, PhD thesis, University of Twente, 2010.
- [5] D. Cannon, K.O. Edel, S. Grassie & K. Sawley, Rail defects: an overview, *Fatigue & Fracture of Engineering Materials & Structures*, 26 (2003) 865–886.
- [6] M. Molodova, Z. Li, A. Núñez & R. Dollevoet, Automatic detection of squats in railway infrastructure, *IEEE Transactions on Intelligent Transportation Systems* 15-5 (2014) 1980–1990.

- [7] X. Zhao, Dynamic wheel/rail rolling contact at singular defects with application to squats, PhD thesis, Delft University of Technology, 2012.
- [8] R. Dollevoet, Z. Li & O. Arias-Cuevas, A method for the prediction of head checking initiation location and orientation under operational loading conditions. Proceedings of the Institution of Mechanical Engineers, Part F: Journal of Rail and Rapid Transit, 224–5 (2010) 369–374.
- [9] Z. Li, X. Zhao, C. Esveld, R. Dollevoet & M. Molodova, An investigation into the causes of squats—correlation analysis and numerical modeling, *Wear*, 265 (2008) 1349–1355.
- [10] X. Deng, Z. Qian, Z. Li & R. Dollevoet, Investigation of the formation of corrugation–induced rail squats based on extensive field monitoring, *International Journal of Fatigue*, 112 (2018) 94–105.
- [11] X. Deng, Z. Li, Z. Qian, W. Zhai, Q. Xiao & R. Dollevoet, Pre–cracking development of weld–induced squats due to plastic deformation: five–year field monitoring and numerical analysis, *International Journal of Fatigue* 127 (2019) 431–444.
- [12] W.J. Daniel, S. Pal & M. Farjoo, Rail squats: progress in understanding the Australian experience, Proceedings of the Institution of Mechanical Engineers, Part F: Journal of Rail and Rapid Transit, 227 (2013) 481–492.
- [13] M. Steenbergen & R. Dollevoet, On the mechanism of squat formation on train rails–Part I: Origination, *International Journal of Fatigue*, 47 (2013) 361–372.
- [14] S. Pal, C. Valente, W. Daniel & M. Farjoo, Metallurgical and physical understanding of rail squat initiation and propagation, *Wear*, 284 (2012) 30–42.
- [15] S. Li, J. Wu, R. H. Petrov, Z. Li, R. Dollevoet & J. Sietsma. “Brown Etching Layer”: A possible new insight into the crack Initiation of rolling contact fatigue in rail steels? *Engineering Failure Analysis*, 66 (2016) 8–18.
- [16] S. Pal, W.J.T. Daniel & M. Farjoo, Early stages of rail squat formation and the role of a white etching layer, *International Journal of Fatigue*, 52 (2013) 144–156.
- [17] L. Wu, Z.F. Wen, W. Li & X.S. Jin, Thermo–elastic–plastic finite element analysis of wheel/rail sliding contact, *Wear*, 271 (2011) 437–443.
- [18] M. Ertz & K. Knothe, Thermal stresses and shakedown in wheel/rail contact, *Archive of Applied Mechanics*, 72 (2003) 715–729.
- [19] A. Böhmer, M. Ertz & K. Knothe, Shakedown limit of rail surfaces including material hardening and thermal stresses, *Fatigue & Fracture of Engineering Materials & Structures*, 26 (2003) 985–998.
- [20] S. Grassie, P. Nilsson, K. Bjurström, A. Frick & L.G. Hansson, Alleviation of rolling contact fatigue on Sweden’s heavy haul railway, *Wear*, 253 (2002) 42–53.
- [21] W. Zhang, H. Dai, Z. Shen & J. Zeng, Roller Rigs, in *Handbook of railway vehicle dynamics* (Chapter 14), in: S. Iwnicki (Ed.), CRC Press, Boca Raton FL (USA), 2006.
- [22] P. Allen, Scale Testing, in *Handbook of railway vehicle dynamics* (Chapter 15) in: S. Iwnicki (Ed.), CRC Press, Boca Raton FL (USA), 2006.
- [23] A. Jaschinski, H. Chollet, S. Iwnicki, A. Wickens & J. Würzen, The application of roller rigs to railway vehicle dynamics, *Vehicle System Dynamics*, 31 (1999) 345–392.
- [24] M. Gretschel & A. Jaschinski, Design of an active wheelset on a scaled roller rig, *Vehicle System Dynamics*, 41 (2004) 365–381.
- [25] A. Jaschinski, F. Grupp & H. Netter, Parameter identification and experimental investigations of unconventional railway wheelset designs on a scaled roller rig, *Vehicle System Dynamics*, 25 (1996) 293–316.
- [26] D.J. Thompson, A.D. Monk–Steel, C.J.C. Jones, P.D. Allen, S.S. Hsu & S.D. Iwnicki, Railway noise: curve squeal, roughness growth, friction and wear, *Real Research UK*, Report: RRUk A, 3 (2003).



- [27] M.P. Papaelias, C. Roberts & C. Davis, A review on non-destructive evaluation of rails: state-of-the-art and future development, *Proceedings of the Institution of Mechanical Engineers, Part F: Journal of Rail and rapid transit*, 222 (2008) 367–384.
- [28] H. Pirgazi, S. Ghodrat & L.A.I. Kestens, Three-dimensional EBSD characterization of thermo-mechanical fatigue crack morphology in compacted graphite iron, *Materials Characterization*, 90 (2014) 13–20.
- [29] T. Hashimoto, G.E. Thompson, X. Zhou & P.J. Withers, 3D imaging by serial block face scanning electron microscopy for materials science using ultramicrotomy, *Ultramicroscopy*, 163 (2016) 6–18.

# 2

## Chapter 2 A new modelling tool for thermomechanical analysis of the wheel–rail contact

*A considerable amount of literature has been published on wheel–rail contact mechanics. The process, through which thermal effects are created, however, is not fully understood yet. This is especially relevant for analysing rolling contact fatigue, in which, multiple sources of fatigue are potentially present, such as dynamic forces, plastic deformation, ratchetting and material phase transformation. This chapter introduces a new advanced numerical modelling tool that benefits from a coupled thermomechanical analysis for the wheel–rail contact problem.*

*In Section 2.2, a three–dimensional (3D) elasto–plastic finite element model is built, capable of predicting temperature rise and thermal stresses associated with the frictional rolling contact between the wheels and rails. Main points addressed are the use of nonlinear temperature–dependent material properties and thermomechanical coupling for calculating the amount of temperature rise, residual stresses and plastic strains. After introducing the modelling tool, the results are compared for different material models in Section 2.3.*

*Section 2.4 introduces some discussions on the formation process of rail squats using the numerical results, obtained in the former sections. The peak contact temperature and its alteration rates are used to examine the formation possibility of white etching layer using martensite transformation theory. The formation mechanism of squats is finally predicted by synthesising the temperature outputs and stress–strain responses.<sup>1</sup>*

---

<sup>1</sup> This chapter is based on the following publication:

M. Naeimi, S. Li, Z. Li, J. Wu, R.H. Petrov, J. Sietsma & R. Dollevoet, *Thermomechanical analysis of the wheel–rail contact using a coupled modelling procedure*, *Tribology International*, 117 (2018) 250–260.

## 2.1 Introduction

Friction between wheels and rails is an important agent that provides adhesion and traction/braking possibilities for trains. On the other hand, due to friction, part of the mechanical energy is dissipated by the frictional work when the train wheels run along the rail. Most of this frictional work is transformed into the frictional heat between the in-contact surfaces. Due to the small size of the contact patch, this frictional heat can significantly increase the temperature of the adjacent materials. The heating of wheel and rail materials can be a critical issue as it may lead to thermomechanical fatigue and/or microstructural transformations [1] e.g. generation of the brittle white etching layer (WEL).

The problem of thermal fatigue in wheels created by thermal loads has been investigated in a number of studies. According to [2, 3], the initiation and propagation of surface cracks in wheels are highly related to the presence of thermal loads. An overview of the rolling contact fatigue (RCF) phenomenon in wheels and rails, considering both mechanical and thermal loading by rolling contact, has been published in [4]. More recently, the fatigue behaviour of railway wheels under combined thermal and mechanical loadings has been studied [5], where thermal effects have created high stresses and decreased the fatigue life of wheel materials. Temperature rise and thermal stresses are also detrimental to the fatigue life of rails, considering the similar microstructure and loading conditions of the wheels and rails. Numerical simulations in [6] indicate that thermal loading has a significant influence on plastic strains and residual stresses at the rail surface, which can expedite the formation of RCF cracks.

A classical research about the RCF in the wheel–rail system [7] lists some controllable variables that can influence RCF: the contact forces, the size, geometry and location of the wheel–rail contact patch, the friction forces, lubrication, the residual, bending and thermal stresses and the material properties. In addition to these, the random character of the acting loads, contact geometries and fatigue strength of materials is considered in [4] as an important aspect in fatigue of railway components. Various models are also available for predicting the fatigue life in the wheel and rail materials, e.g. shear strains fatigue failure, multiaxial fatigue damage and energy–density based models [8].

Thermal effects in the wheel–rail contact can affect the magnitude and distribution of residual stress and strain components [9], altering the shakedown behaviour and fatigue life of materials. When the elastic limit of the material is exceeded, plastic deformations occur and after the load removal, residual stresses remain in materials [9]. Thermal stresses due to frictional heating can have additional contribution to the total stresses. According to [9, 10], if thermal stresses in the sliding wheel–rail contact are superimposed on the mechanical contact stresses, the elastic and shakedown limits of the wheel and rail will be reduced, and yielding will begin at lower mechanical loads. These thermal stresses are generated in a very thin surface layer of materials in contact where elevated temperature occurs [10].

Another potential problem is that the contact temperatures might be high enough to cause thermally–induced phase transformation in wheel–rail materials. According to a recent study [11], evidence of severe thermal loading and WEL formation is often associated with rail defects. This phenomenon might also explain the formation of some squat defects. Squats are one of the major RCF defects that occur mostly in the running band of rails and can create high dynamic forces. The contact temperature and thermal stresses could be driving factors for squats initiation. To distinguish thermal origins of such defects, a different name “studs” has even been suggested [12]. By investigating the rail microstructure [13], squats were found to be associated with WEL formation on the surface. When WEL is characterised as martensite microstructure, e.g. [14], it indicates a temperature rise up to the austenitizing temperature, e.g. 727°C for the binary Fe–0.76C steel. In such case, the austenite transforms

to martensite during the subsequent rapid cooling. It is also believed that such thermal transformation in rail materials can be linked to high thermal stresses, that may assist WEL formation or even produce it [15]. A recent study in this field [16] relates the formation of WEL to the temperature rise up to austenitization limit.

To deal with the thermal aspects of RCF in rails, a realistic estimate of the thermal stresses and contact temperature is required. A review of the literature shows a general lack of modelling tools for thermomechanical modelling of the wheel–rail contact; see the literature gap and the importance of coupled modelling in the next section. This research develops a coupled thermomechanical tool, capable of simultaneously calculating the flash temperature and stress–strain responses in the wheel–rail materials. It considers detailed material aspects, i.e. temperature–dependency, nonlinearity and thermal softening by importing the material parameters as a function of temperature in the numerical process. The outputs are used to evaluate the influence of thermal effects on stress–strain responses and to predict the potential of WEL formation in the rail.

## 2.2 Thermomechanical modelling of the wheel–rail contact

As mentioned above, friction creates heat at the contact interface due to the work done by moving wheels. Frictional behaviours have been studied in many wheel–rail contact models in the literature, dealing with microslip, tangential stresses and deformations. Microslip, which is the relative motion of contact particles, is the origin of many issues like fatigue and wear of wheels and rails. Tangential forces, produced by driving/braking wheels, can significantly change the contact stresses and fatigue behaviours. The numerical models of [17–19] have focused mainly on the tangential problem, surface shear stresses and microslip in the wheel–rail contact, whereas, they have not studied the frictional heat, temperature rise and accompanying thermal stresses.

A growing body of literature has recognised the importance of thermal effects in wheel–rail rolling contact. Some classical studies, e.g. [20, 21], used analytical methods to calculate the temperature rise during sliding contact situations. These studies had the following limitations: 1) They were developed based on the Hertz theory, which is only valid for the contact between elastic materials. Therefore, they cannot consider nonlinear material properties, which is more realistic in the case of wheel–rail contact. 2) They do not consider a wheel in the calculation; instead, they simplify the presence of the wheel with a moving load and heat over the rail surface. 3) They can only deal with the full–slip contact (when the wheel is in complete sliding). Hence, they cannot calculate the temperature rise and thermal stresses under partial–slip conditions. 4) They assume a rigid body creepage on the entire contact patch and they ignore the distribution of microslip at the contact patch, which is typical of railway operation. 5) The material properties and the coefficient of friction were considered independent of the temperature which is not the real case for wheel–rail materials. The mentioned limitations cause inaccuracies in calculating the temperature rise especially at higher temperatures ( $T > 300$  °C).

Some researchers calculated the thermal stresses associated with the temperature rise in frictional contact between wheels and rails; see e.g. [22, 23]. A two–dimensional finite element model of the rail has been constructed in [24], in order to calculate contact temperature, thermal stresses, plastic strains and wear rates of rails. Another 2D finite element model is used in [6] to investigate the thermal–elastic–plastic deformations and residual stresses during wheel sliding. A recent study [25] used a 3D finite element model for the rail to determine the temperature rise, residual stresses and plastic strains. Although this 3D model [25] is developed to estimate the temperature rise and thermal stresses, it does not still consider the transformation of the frictional energy at the contact patch into heat. Similar to

other studies, it has employed a moving heat source on the rail, by which, the thermal solution has been obtained uncoupled from the mechanical solution.

Looking at the literature, one can see a general lack of a finite element model that simulates the coupled thermomechanical behaviour of the wheel–rail system. By coupled modelling, we mean a model that simultaneously considers: 1) the frictional rolling contact of the wheel and the rail; 2) conversion of the frictional energy at the contact patch into heat; 3) distribution of the generated heat in the upper and lower bodies i.e. the wheel and rail; and 4) simultaneous thermal and mechanical analysis of the wheel–rail contact problem. This coupled behaviour is an important factor for the accurate estimation of the temperature and thermomechanical stresses. The reason is that in a coupled analysis the frictional energy (as a result of the load and microslip) is directly calculated and instantaneously converted into the heat. There is no need to define a simplified heat equation and to apply the thermal flux on a rail surface. The heat source in the coupled model is directly calculated by the product of tangential load and microslip in each element in the contact patch. It provides thus a more realistic condition than considering e.g. an elliptical or uniform heat flow on the surface which was suggested by [26].

The finite element model of this research simulates the frictional rolling contact process of the wheel over a length of the rail. It provides the following advantages in comparison with the available methods in the literature: 1) in addition to the normal contact problem, this model considers the creepage in the wheel–rail contact, as well as tractive forces, applied to the wheel; 2) the model can simulate both partial–slip and full–sliding contact conditions between the wheel and rail; 3) it considers elasto–plastic material properties with temperature dependency; and 4) by employing a coupled thermomechanical analysis, it directly converts the frictional energy into heat and computes the temperature and thermomechanical stresses. Figure 2.1 shows the finite element model of the wheel–track system developed in this research. The vehicle and the bogie are lumped into mass elements supported by a set of spring–damper elements serving as the primary suspension. The railway track includes the rail, sleepers and, fastening system and ballast. The fastening and the ballast are modelled with their respective parallel spring–damper elements. The spring–dampers between the rail and sleepers (fastening system) provide for the rail a vertical degree of freedom. The sleepers are allowed to move vertically on top of the ballast. The ballast consists of parallel springs and dampers that are at their upper ends connected to the sleepers and at lower ends to the fixed ground. The lateral movement of the wheel is constrained by applying symmetric boundary conditions on it.

This model benefits from a 3D mesh for the wheel, rail and sleepers using 8–node solid elements. To achieve high accuracy with efficient computing time, a non–uniform discretization strategy is used with the finest mesh in the contact region. The elements in the solution zone are refined down to 0.8 mm and the elements far from the solution zone are meshed at an element size up to 7.5 cm. The total number of elements in the model is 1,135,388 and the total number of nodes is 1,297,900. The wheel speed is 38.9 m/s corresponding to the typical Dutch passenger train speed of 140 km/h. The nominal radius of the wheel is 0.46 m and the model length is 20.54 m. At the beginning of simulations ( $x=0$ ,  $t=0$ ), stresses and strains are zero and materials are at atmospheric temperature. When the wheel runs over the rail, thermomechanical quantities in materials build up. The outputs of simulations are obtained when the wheel is located at  $x = 0.45$  m. The input parameters of the finite element model are given in the following sections.

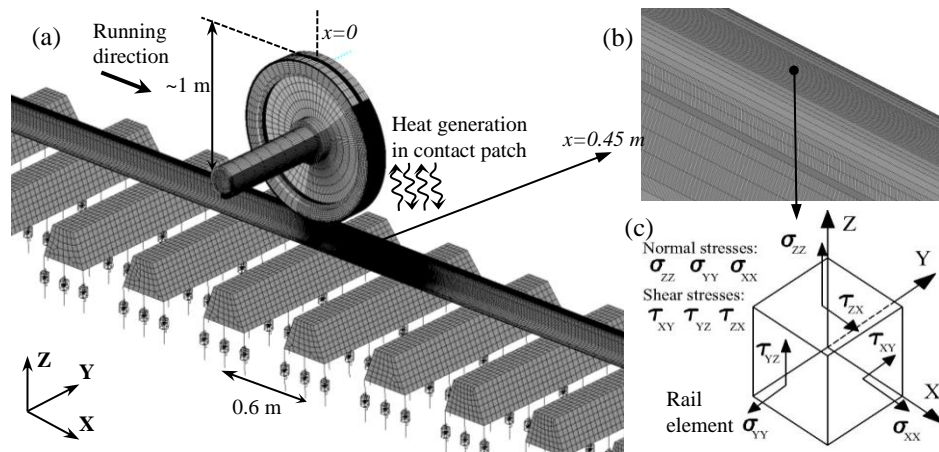


Figure 2.1. The finite element model of the wheel on the track system; (a) the finite element mesh; frictional heat is generated in the contact interface;  $x=0$  is the initial location of the wheel;  $x=0.45\text{ m}$  is the location, at which, the thermomechanical outputs are calculated; (b) magnification of the solution zone in the rail surface, (c) the stress components in one rail element located in the rail surface in the middle of the running band

### 2.2.1 Thermomechanical coupling

The mechanical contact between the wheel and rail is influenced by the heat production and therefore temperature gradients in materials. A suitable computational tool has to be able to consider the contact process as well as the heat conduction. For this kind of problems, thermomechanical coupling analysis can be used [27]. To perform a coupling analysis in this research, the finite element modelling consists of two transient problems; see Figure 2.2. The finite element model is developed with ANSYS/LS-DYNA, and the coupled thermomechanical problem is solved by LS-DYNA.

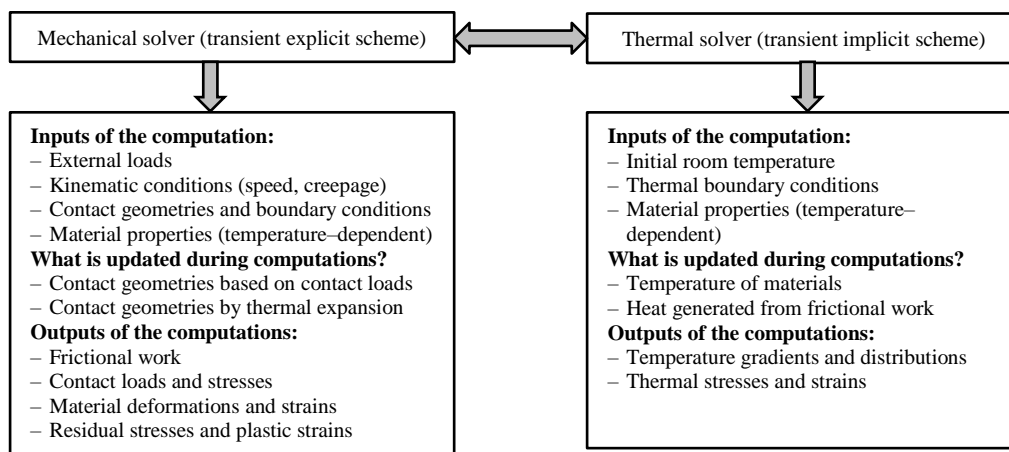


Figure 2.2. An overview of the coupled thermomechanical finite element analysis

### 2.2.2 Mechanical solver

The mechanical solver is based on Lagrangian formulation for the wheel–rail contact problem. In this solver, an explicit time integration scheme is used due to its stability in achieving accurate solutions with efficient computation [28]. The mechanical part of the analysis is governed by geometric, kinematic and loading parameters applied on the finite element mesh. When the wheel runs over the rail, a surface-to-surface contact scheme based on a master–slave algorithm [29] is used. This activates the underlying frictional algorithm and updates the interface forces and deformations during contact. When the slave node penetrates, an interface force is applied between the slave node and its contact point with the magnitude proportional to the extent of penetration.

According to Coulomb friction law, the limiting friction force between two contact bodies is  $f|F_n|$  in which,  $f$  is the frictional coefficient and  $F_n$  is the normal contact force. The initial frictional force in the numerical process is [30]:

$$F_f^* = F_f^t - E_f \Delta u_s \quad 2.1$$

where,  $E_f$  is the interfacial friction modulus,  $\Delta u_s$  is the incremental tangential displacement during a given time increment and  $F_f^t$  is the frictional force at time  $t$ . The frictional force increment during this time increment is  $\Delta F_f = F_f^* - F_f^t$ . The stick–slip condition is checked for calculating the evolution of the frictional force in the numerical process. If  $F_f^* - f|F_n| \leq 0$  is satisfied, the contact points are in stick and the frictional force at time  $t + \Delta t$  is calculated as

$$F_f^{t+\Delta t} = F_f^* \quad 2.2$$

otherwise ( $F_f^* - f|F_n| > 0$ ), the contact points are in slip and the frictional force at time  $t + \Delta t$  is:

$$F_f^{t+\Delta t} = f|F_n| \frac{F_f^*}{|F_f^*|} \quad 2.3$$

The motions of two deformable contact bodies  $b_1$  and  $b_2$  in the normal ( $n$ ) and tangential ( $s$ ) directions are considered. Let  $n_1$  and  $n_2$  be the unit normal vectors and  $s_1$  and  $s_2$  be the unit vectors tangent to the surface of these contact bodies. The impenetrability condition is applied to those portions of these bodies, which are already in contact. It can be written as [31]:

$$v_n^t = v_n^{b1} - v_n^{b2} = \dot{u}_1 \cdot n_1 + \dot{u}_2 \cdot n_2 \leq 0 \quad 2.4$$

where,  $u_1$  and  $u_2$  are the motion vectors,  $v_n^{b1}$  and  $v_n^{b2}$  are the velocity vectors and  $v_n^t$  is the relative normal velocity of the two contact bodies. The relative tangential velocity is calculated by:

$$v_s^t = \dot{u}_1 \cdot s_1 - \dot{u}_2 \cdot s_2 \quad 2.5$$

The numerical process uses  $F_f^t$  and  $v_s^t$  at each time step as the inputs for calculating the frictional energy  $\dot{Q}_f^t$  of the contact domain  $\Omega$  of the two bodies with  $\varepsilon$  as the heat–partitioning factor between these bodies:

$$\dot{Q}_f^t = \int_{\Omega} \varepsilon F_f^t v_s^t ds \quad 2.6$$

### 2.2.3 The thermal solver

The thermal solver in LS–DYNA employs an implicit scheme using a generalized trapezoidal time integration algorithm [32]. The implicit solver is a tailored solver for static and long duration problems. The implicit solver possesses a wider stability region than the explicit method [33], therefore, a larger thermal time step can be taken, which can enhance the calculation efficiency. The time step for the explicit mechanical solver in this research was  $4.67 \times 10^{-8}$  s, which is small enough to meet the Courant stability condition [34], i.e. to ensure that a sound wave may not cross the smallest element during one time step. The time step for the implicit thermal solver in this research was  $6 \times 10^{-5}$  s. This time step is small enough to capture the temperature gradient in the smallest element during the thermal solution as suggested by [35]. The computational cost of thermal problems (e.g. thermal convection) is far lower when the implicit solver is used. The thermal part of the analysis is controlled by thermal boundary conditions and parameters e.g. specific heat and conductivity. The general heat conduction equation for the given problem can be written by [36]:

$$\frac{\partial}{\partial x} \left( \lambda_x \frac{\partial T}{\partial x} \right) + \frac{\partial}{\partial y} \left( \lambda_y \frac{\partial T}{\partial y} \right) + \frac{\partial}{\partial z} \left( \lambda_z \frac{\partial T}{\partial z} \right) + I(x, y, z, t) = \rho c \frac{\partial T}{\partial t} \quad 2.7$$

where,  $T$  is the temperature,  $\rho$  is the density,  $c$  is the heat capacity,  $I(x, y, z, t)$  is the internal heat generation rate per unit volume and  $\lambda_x, \lambda_y, \lambda_z$  are the thermal conductivity in  $x$ ,  $y$  and  $z$  directions. It is a second–order partial differential equation involving rates of change with respect to the time and position. The material points in the contact patch are subjected to the frictional heat  $\dot{Q}_f$  during the wheel travel. Assuming  $T_0$  as the initial temperature, the initial condition will be  $T_{x,y,z}^{t=0} = T_0$  and the boundary condition at time  $t$  can be written as [37]:

$$\lambda_x \frac{\partial T}{\partial x} n_x + \lambda_y \frac{\partial T}{\partial y} n_y + \lambda_z \frac{\partial T}{\partial z} n_z = \dot{Q}_f \quad 2.8$$

where,  $\lambda_x, \lambda_y, \lambda_z$  are the thermal conductivity in  $x$ ,  $y$  and  $z$  directions and  $n_x, n_y, n_z$  are the normal vectors. There is no closed–form solution available for the aforementioned heat conduction problem. The numerical model of this research solves the aforementioned heat conduction problem by means of a trapezoidal time integration algorithm [32].

In the coupled analysis, the frictional energy in the contact interface ( $\dot{Q}_f$ , which is calculated by the mechanical solver) is first stored as the surface energy density in a temporary file. The numerical tool then considers the frictional energy as the heat source when doing a coupled thermomechanical simulation (Figure 2.2). This frictional heat is generated in the upper and lower contact surfaces, i.e., of the wheel and rail. It is immediately conducted in the adjacent wheel–rail materials, resulting in thermal stresses and temperature fields (calculated by the thermal solver).

#### 2.2.4 Thermomechanical parameters

Mechanical and thermal properties of steel materials are influenced by temperature variations. The thermomechanical model in this research uses the temperature–dependent mechanical and thermal parameters as the input. A bilinear elasto–plastic material model with kinematic hardening is used. Considering the Bauschinger effect, the total stress range in this material model is assumed twice of the initial yield stress [38]. The temperature–dependency of the mechanical parameters is shown in Table 2.1 and that of the thermal parameters in Table 2.2. These material parameters are given in [6, 39] for several temperature values in the range of 0–1200 °C. Thermal softening is defined by a reduction of the Young modulus ( $E$ ), yield strength ( $\sigma_y$ ) and hardening modulus ( $E_p$ ) at elevated temperatures. The rail material with the grade R260Mn has a typical initial yield stress between 452 and 636 MPa [40]. In order to consider the work hardening of the rail material, an enlarged value of yield stress  $\sigma_{yref} = 800$  MPa is used at the initial (room) temperature  $T_0$ . The same assumption was also recently made by [25, 28].

The yield point depends on the load level and the number of cycles. The assumption that the yield point increases from its initial value of 452~636 MPa to the assumed 800 MPa at 24 °C was based on the tensile strength of above 880 MPa for the pearlitic rail grade R260 [41].



Table 2.1. Temperature dependency of mechanical parameters used in the modelling [25, 39]

Temperature, $T$ (°C)	Young's modulus, $E$ (GPa)	Poisson's ratio, $\nu$	Yield strength, $\sigma_y$ (MPa)	Coefficient of thermal expansion, $\alpha$ ( $\times 10^{-6} \text{C}^{-1}$ )	Hardening modulus, $E_p$ (GPa)
24	213	0.295	800.0	9.89	22.7
230	201	0.307	802.1	10.82	26.9
358	193	0.314	735.8	11.15	21.3
452	172	0.32	649.4	11.27	15.6
567	102	0.326	468.1	11.31	6.2
704	50	0.334	362.0	11.28	1.0
900	43	0.345	330.4	11.25	0.1

Table 2.2. Temperature dependency of thermal parameters used in the modelling [39]

Temperature, $T$ (°C)	Specific heat capacity $c$ (J/kg°C)	Thermal conductivity $\lambda$ (W/m°C)
0	419.5	59.71
350	629.5	40.88
703	744.5	30.21
704	652.9	30.18
710	653.2	30
800	657.7	25
950	665.2	27.05
1200	677.3	30.46

In addition to the presented Thermo–elasto–plastic material, a simple elastic model and an elasto–plastic model (independent of temperature) were considered for the sake of comparison. These two material models are called the isothermal materials. For these materials, the properties at the initial temperature ( $T_0$ ) were used. Numerical simulations were carried out for them using the same finite element model, but with the thermal solver in the coupled analysis being switched off; so that only the mechanical solver was activated. In total, five material models were defined as listed in Table 2.3. The TEPS model was the most advanced model considered in this research. The type of numerical solver in each model is also given in Table 2.3. The mechanical contact solver is used for E and EP and the coupled thermomechanical for ET, TEP and TEPS.

Parameters of the vehicle–track system have significant influences on the numerical results. This research uses the parameters listed in Table 2.4. Three high creepage scenarios (10, 18 and 26%) were considered for the simulations to account for more critical conditions in terms of heat generation and temperature rise. For the same reason, a high vertical wheel load of 134 kN and a high friction coefficient of 0.6 were selected. The wheel moves with a constant velocity along the rail surface. It also rotates with a constant rotational velocity in order to create the required creepage given in the table.

Table 2.3. The numerical simulations considered in this research

Number	Type of material model	Model name (abbreviation)	Type of numerical solver	Model description	Type of stress–strain results
1	Elastic (isothermal)	E	Purely mechanical contact (no thermal solution)	It uses linear material properties at $T_0$ in Table 2.1. $E_P$ and $\sigma_y$ were disregarded.	Mechanical loading generates elastic stresses and strains.
2	Elastic–thermal (temperature independent)	ET	Coupled thermomechanical contact	It uses linear material properties at $T_0$ in Table 2.1. $E_P$ and $\sigma_y$ were disregarded. The material is temperature independent.	Mechanical loading generates elastic stresses and strains. Frictional heat generates thermal stresses and strains.
3	Elasto–plastic (isothermal)	EP	Purely mechanical contact (no thermal solution)	It uses bilinear material properties at $T_0$ including $E_P$ and $\sigma_y$ .	Mechanical loading generates elastic and residual stresses and strains.
4	Thermo–elasto–plastic (without thermal softening, temperature independent)	TEP	Coupled thermomechanical contact	It uses bilinear material properties at $T_0$ including $E_P$ and $\sigma_y$ . The material is temperature independent.	Mechanical loading generates elastic and residual stresses and strains. Frictional heat generates thermal stresses and strains.
5	Thermo–elasto–plastic with thermal softening (temperature dependent)	TEPS	Coupled thermomechanical contact	It uses bilinear material properties at $T_0$ including $E_P$ and $\sigma_y$ . Material is temperature–dependent (all parameters in Tables 2.1 and 2.2)	Mechanical loading generates elastic and residual stresses and strains. Frictional heat generates thermal stresses and strains.

Table 2.4. Parameters of the vehicle–track system used in the modelling

Symbol (units)	Description	Value
$F_N$ (kN)	Vertical load on the wheel	134
$V$ (km/h)	Wheel forward velocity	140
$s$ (%)	Longitudinal creepage	10, 18, 26
$V_R$ (km/h)	Wheel rotational velocity	154, 165, 176
$f$	Coefficient of friction	0.6
$\rho_s$ (kg/m <sup>3</sup> )	Density of wheel–rail material	7850
$T_0$ (°C)	Initial temperature	25
$M_w$ (kg)	Wheel weight	900
$M_s$ (kg)	Mass of concrete sleeper	280
$E_c$ (GP)	Young’s modulus of concrete	38.4
$\nu_c$	Poisson’s ratio concrete	0.2
$\rho_c$ (kg/m <sup>3</sup> )	Density of sleeper material	2520
$K_c$ (kN/m)	Stiffness of primary suspension	880
$C_c$ (N·s/m)	Damping of primary suspension	4000
$K_p$ (kN/m)	Stiffness of rail pad	1,300,000
$C_p$ (N·s/m)	Damping of rail pad	45,000
$K_b$ (kN/m)	Stiffness of ballast	45,000
$C_b$ (N·s/m)	Damping of ballast	32,000

## 2.3 Results of numerical simulations

Finite element simulations were carried out for the mentioned material models, i.e. E, EP, ET, TEP and TEPS given in Table 2.3. The results in this section are obtained for the medium creepage scenario ( $s = 18\%$ ). The following explanation is important for obtaining the results:

The track length, region of discretization with the finest mesh and the wheel travel time are restricted to achieve a reasonable simulation time. The wheel makes approximately a quarter of a full revolution during the simulation. Due to the absence of irregularity in the wheel-rail interface, the contact reaches, over such a short travelling distance, through dynamic relaxation [42], a steady state of the mechanical responses.

At the beginning of the simulation, the wheel and rail are at the room temperature; during rolling, the temperature increases at the contact interface (due to the frictional heat) as well as at the nearby elements (due to the heat conduction). At any time step, it is possible to record the temperature and the stress distributions in the elements. After a travelling distance of 0.45 m, we recorded the temperature and stress distributions in the contact patch and the region which is already travelled by the wheel. At this location, we have the finest mesh in the contact interface, which is an ideal place to record the results. Moreover, the peak stresses and temperature in the contact patch at this location have reached steady state condition, i.e., their values are relatively stable at each time step.

The peak temperature happens in the contact patch and the decay part of any temperature distribution shows the cooling process. The focus was on recording the peak temperature at and in the vicinity of the contact patch. Effects of cooling and retained heat of multiple wheel revolutions on the peak temperature are not considered.

### 2.3.1 Thermomechanical stresses

Figure 2.3 shows, for the different models, the time histories of stress components in a rail element in the surface (element number 827719). Such stresses were recorded for an element located at  $x = 0.45$  m (Figure 2.1) when the train wheel travels with the given speed along the rail. The abscissa shows the time passed from the moment that wheel has been at its initial location ( $x = 0.45$  m). Six stress components are shown, three of which are the orthogonal normal components i.e. the vertical, longitudinal and lateral components. The other three are the shear component in different planes; see the nominations in Figure 2.1(c).

As can be seen in Figure 2.3, the stresses were zero when there is no wheel around the rail element ( $t = 9.6$  ms). The stress components were gradually built up in the chosen element when the wheel gets close to this element (located at  $x=0.45$  m). The stresses reached their maximum when the wheel is nearly on top of this element ( $t = 10.1$  ms) and then decreased when the wheel moves away from this element. In the nonlinear models (EP, TEP, TEPS), residual stresses are seen on the right side of the graphs in Figure 2.3 ( $t = 10.6$  ms), even when the wheel has fully left the solution zone. Two of orthogonal normal stresses ( $\sigma_{zz}, \sigma_{yy}$ ) were negative (compressive) during the wheel passage, while  $\sigma_{xx}$  revealed a sign reversal because of the loading applied to generate the required creepage ( $s = 18\%$ ). This also caused significant shear stress in the vertical–longitudinal plane ( $\tau_{zx}$ ). The other shear components ( $\tau_{xy}, \tau_{yz}$ ) were negligible since no lateral load or creepage is considered.

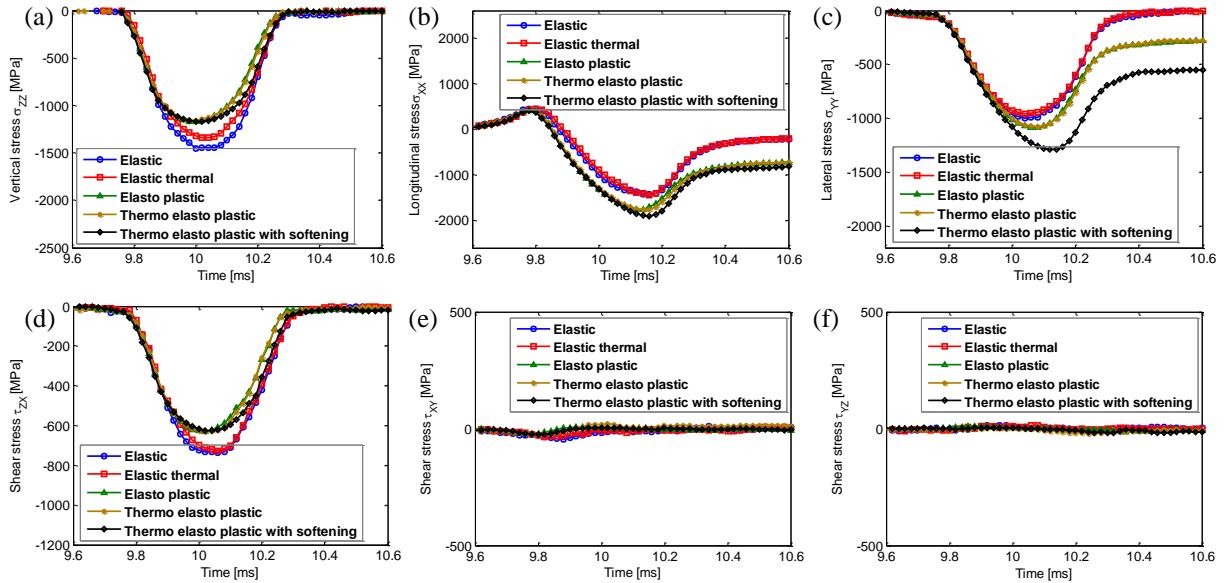


Figure 2.3. The stress histories in a rail element at  $x = 0.45$  m in the surface for 5 different material models, i.e. Elastic, Elastic thermal, Elasto–plastic, Thermo–elasto–plastic and Thermo–elasto–plastic with softening, (a)

$\sigma_{ZZ}$ ; (b)  $\sigma_{XX}$ ; (c)  $\sigma_{YY}$ ; (d)  $\tau_{ZX}$ ; (e)  $\tau_{XY}$ ; (f)  $\tau_{YZ}$

The stress histories of different material models significantly differ in shape and magnitude. To facilitate the comparison, the results of the equivalent von–Mises (V–M) stresses were calculated for the different material models; see Figure 2.4(a). The peak stresses, calculated for the different models, are given in Figure 2.4(b). The difference in stress between elastic and plastic models was significant. This is due to the effect of plasticity in materials, which increases the size of the contact patch and reduces the stresses; compare e.g. the  $\sigma_{VM}$  results of E with EP and ET with TEP in Figure 2.4. As can be seen in these figures, the peak stresses were higher in the elastic models than in the elasto–plastic models, irrespective of the thermal effects. Another observation is that, in the elastoplastic models, the location of the peak V–M stress shifts forward along the time axis. The abscissa (time) can be interpreted by the wheel location ( $x$ ) considering the relationship between the speed and time. When the peak V–M stress is shifted forward along the time axis it means that the peak stresses shift towards the trailing edge of the contact patch ( $x$ ). This is in contrast with the elastic models, in which, the peaks occur nearly in the middle of the contact patch. The reason for this observation is the work hardening and conformity increase between the contact bodies after plastic deformation, which causes the stresses to develop in the location where the maximum plastic deformation occurs [43]. Two of the stress components, i.e. the shear stress  $\tau_{ZX}$  and the normal stress  $\sigma_{YY}$  are higher at the trailing edge of the contact patch, which creates the same effect on the V–M stresses.

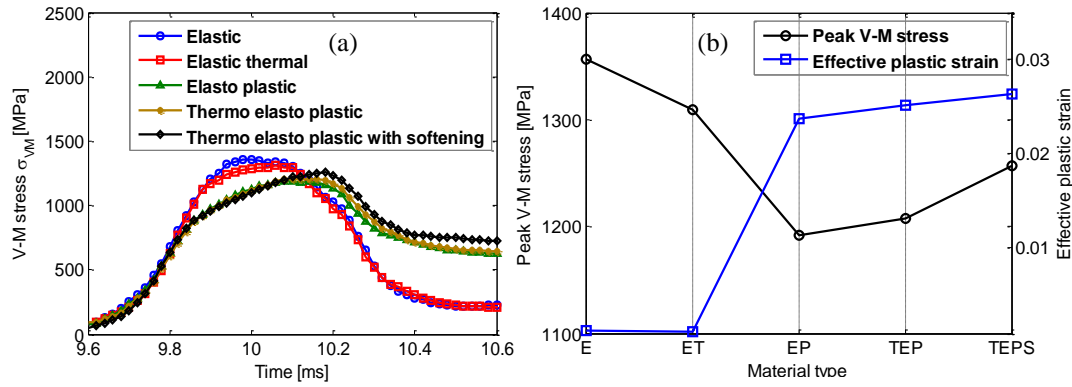


Figure 2.4. (a) The history of V–M stress in a rail surface element at  $x = 0.45$  m for different material models, i.e. Elastic, Elastic thermal, Elasto–plastic, Thermo–elasto–plastic and Thermo–elasto–plastic with softening; (b) the peak V–M stresses and effective plastic strain in different material models

Considering the elastic models (E and ET), it was seen that the thermal effects decrease the magnitude of  $\sigma_{VM}$ . The distribution of  $\sigma_{VM}$  differs more in the nonlinear models (EP, TEP, TEPS), which better indicates the contribution of thermal effects in the stresses. The observation was that the thermal models TEP and TEPS had higher stress peaks than the isothermal model EP. In fact, when thermal effects were introduced, the V–M stresses in the nonlinear models increased.

Figure 2.4(b) also provides the results of effective plastic strain left behind in the rail material when the wheel is far enough from the recording point. In the elastic models (E and ET), the strains returned nearly to zero when the wheel is far away and therefore no residual strains were seen. However, in the elasto–plastic models (EP, TEP and TEPS), there were plastic strains in the rail after the loading. According to Figure 2.4(b), TEPS produced the greatest plastic strain among different models. The TEPS model also produced the highest peak in  $\sigma_{VM}$  among different nonlinear models. As mentioned, TEPS is the most advanced material model, for which, thermomechanical coupling and the temperature–dependency of materials are considered. These results suggest that when thermal effects are introduced:

- Thermal coupling (the type of analysis) causes higher peak stresses and higher plastic deformations in materials (TEPS vs. EP).
- Thermal softening (the type of material) causes higher peak stresses and higher plastic deformations in materials (TEPS vs. TEP).

The stress distributions in the rail surface obtained for the elastic and elasto–plastic models are in good agreement with those of a former isothermal model in [43]. In both models (current research and the model of [43]), the peak V–M stress of the elastic solution is higher than that of the elasto–plastic solution. Further, in both models, the peak stress in the elastic solution is shifted towards the trailing edge of the contact patch. The stress results in this research, however, are not quantitatively identical with the results in [43] as the input parameters were different. The validity of the applied modelling procedure with ANSYS/LS–DYNA (mechanical wheel–rail contact) has been shown in a couple of former researches, e.g. [17] and [18] (discussing only in elasticity) and [43] (discussing in elasto–plasticity).

### 2.3.2 Temperature results

The flash–temperature during the wheel–rail contact is calculated for the thermal models (ET, TEP and TEPS); apparently, E and EP do not provide thermal outputs. Figure 2.5 shows the distribution of flash–temperature in the wheel tread and rail surface during the contact for the medium creepage scenario ( $s = 18\%$ ). The time step  $t = 11.52$  ms was selected to obtain the results; at this time step the wheel has already travelled 0.448 m in the longitudinal direction and the thermomechanical outputs are stable. The rolling direction of the wheel is shown with

V in the figure. The results for the different material models (ET, TEP and TEPS) are separately presented. The wheel tread temperature in these models is shown in Figures 2.5(a, b, c). Figures 2.5(d, e, f) show the corresponding rail surface temperature. A magnified view of each temperature distribution around the contact patch is shown in Figures 2.5(g, h, i).

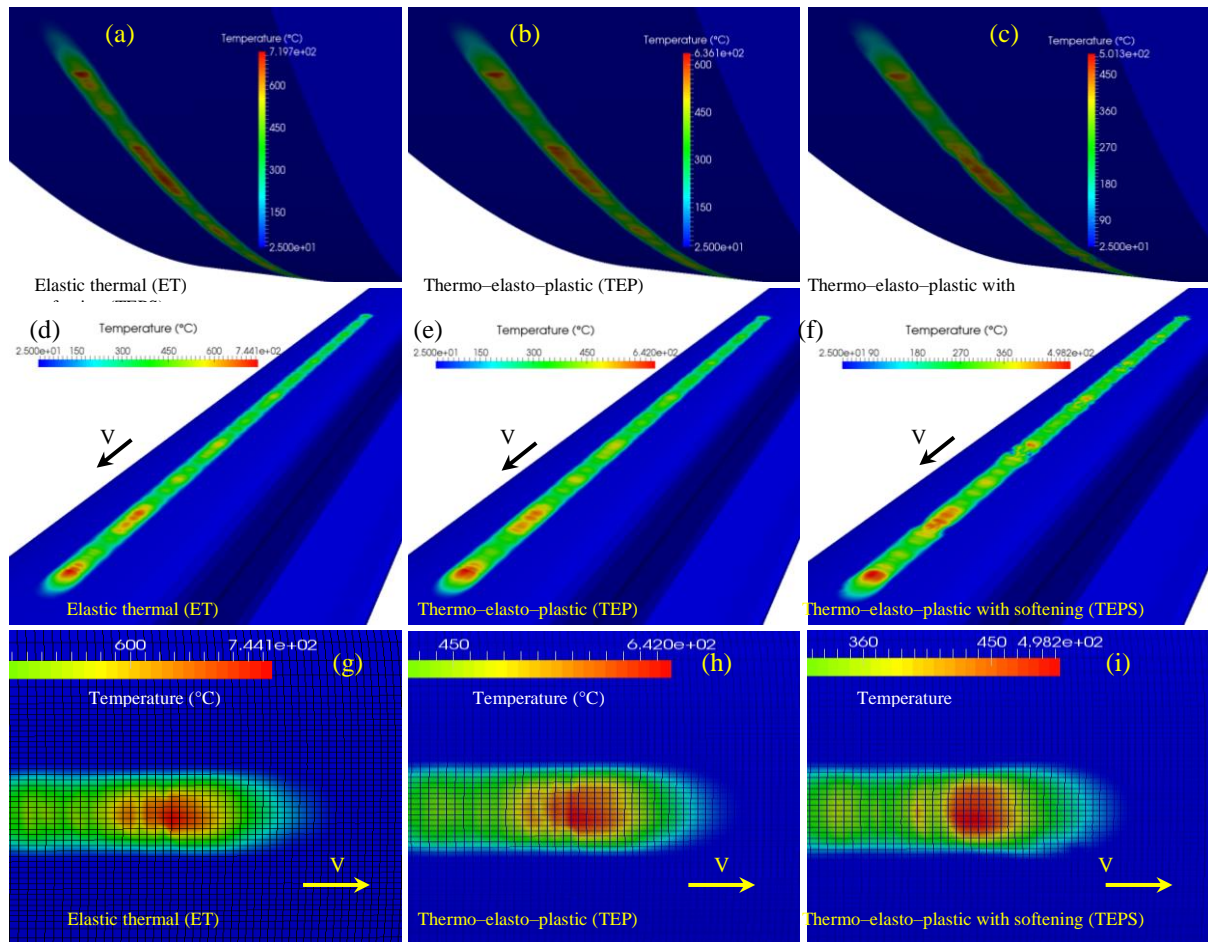


Figure 2.5: Temperature distributions in the wheel tread and rail surface under 18% creepage at  $t = 11.52$  ms; (a, b, c) wheel tread temperature in ET, TEP and TEPS; (d, e, f) corresponding rail surface temperature in ET, TEP and TEPS; (g, h, i) magnification of the rail surface temperature distribution around the contact patch in ET, TEP and TEPS

To facilitate the comparison, the temperature distributions are plotted along the rail longitudinal axis ( $x$ ) in Figure 2.6 and the peak temperature of the wheel tread and rail surface are listed in Table 2.5.

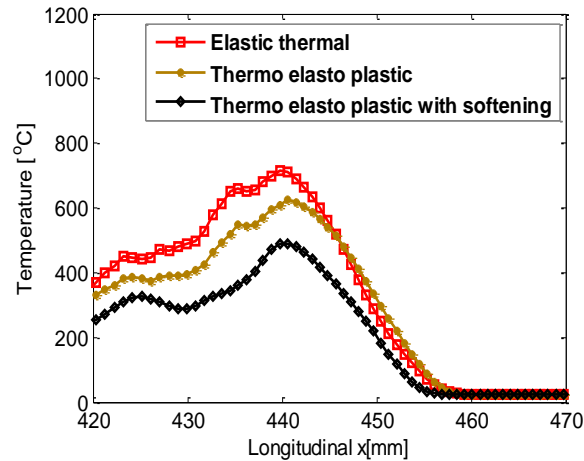


Figure 2.6. Temperature distributions in the rail surface along the  $x$  axis for different thermal models, i.e. Elastic thermal, Thermo–elasto–plastic and Thermo–elasto–plastic with softening, under 18% creepage

Table 2.5. Peak flash–temperature in the wheel and rail for different thermal models under 18% creepage

Material model	Maximum rail temperature (°C)	Maximum wheel temperature (°C)
ET (Elastic thermal)	744	720
TEP (Thermo–elasto–plastic)	642	636
TEPS (Thermo–elasto–plastic with softening)	498	501

According to Figures 2.5 and 2.6, the temperature in the wheel and rail is rapidly increased in the region where contact occurred (a longitudinal distance of around  $440 \text{ mm} < x < 455 \text{ mm}$ ). The peak occurred near the trailing edge of the contact patch (a longitudinal distance of around  $440 \text{ mm}$ ). This was followed by a fast decay in the opposite side of the running direction ( $x < 440 \text{ mm}$ ). There were some local peaks in the decay region because the contact force has fluctuations along the rail as a result of dynamic interaction between the wheel and track system.

According to Table 2.5, the wheel tread and rail surface had close temperature results since the heat (generated due to friction) is equally distributed between the wheel and rail ( $\varepsilon = 0.5$  in Eq. 2.6). In the TEPS model, a nearly equal temperature ( $\sim 500 \text{ °C}$ ) is obtained in the wheel tread and rail surface.

The peak rail temperature for the different material models was different. The maximum rail temperature occurred in the ET model ( $744 \text{ °C}$ ). The reason is that ET generates the greatest amount of surface shear stress and microslip. In the elastic model, higher mechanical energy is dissipated in the contact interface by the frictional work, which is proportional to the product of microslip and surface shear stress.

The temperatures in the nonlinear models TEP and TEPS were  $642 \text{ °C}$  and  $498 \text{ °C}$ , respectively, which were lower than the elastic model ET. This is because they create lower tangential contact stresses. The other reason is that in the nonlinear models, a fraction of the total energy contributes in forming plastic deformation. Hence, a lower temperature is obtained for TEPS and TEP with the minimum in TEPS ( $498 \text{ °C}$ ).

According to the results, among the different nonlinear models, TEPS produced the highest equivalent  $V$ – $M$  stress and the highest plastic deformation; and now among the different thermal models, TEPS produced the least flash–temperature.

The temperature distributions obtained in this research are in a reasonable agreement with another FE model in the literature [25]. The general trend, in which, the rail temperature increased in the contact patch with a peak occurring near the trailing edge of the contact patch was also seen in [25]. The peak temperatures in the current research, however, are not quantitatively identical with those of [25] due to the fact that the FE model in [25]: 1) includes

only the rail and does not simulate the wheel–rail contact problem; 2) is an uncoupled model, in which, the heat source is estimated using theoretical equations; and 3) considers different input parameters.

## 2.4 Discussion

### 2.4.1 Potential of martensitic transformation at supercritical temperatures

The formation of WEL by the martensitic transformation in rail steel was simulated in a recent study [44], using fast heating and quenching experiments and thermodynamic calculations. Microstructural characteristics of the simulated WEL in these experiments were found to be similar to those observed in the field rail specimens. The experimental results and thermodynamic calculations supported the hypothesis for WEL formation via martensitic transformation [44]. The proposed TEPS model is used to investigate the possibility of temperature rise up to the austenitizing limit. The values of parameters that are given in Tables 2.1 and 2.2 for the temperature–dependent elasto–plastic material were used for this purpose. To simulate a more critical situation in terms of frictional heating and its associated temperature rise, a high creepage of 26% was studied, in addition to 10 and 18% given in Table 2.4. Considering such parameters, the temperature distribution in the rail surface was calculated. Figure 2.7 shows the temperature distribution in the rail surface at  $t = 11.52$  ms. This result is obtained for the TEPS model under the 26% creepage. A magnified view of the rail temperature around the contact patch is shown in Figure 2.7(b). The maximum flash temperature, in this case, was 756 °C.

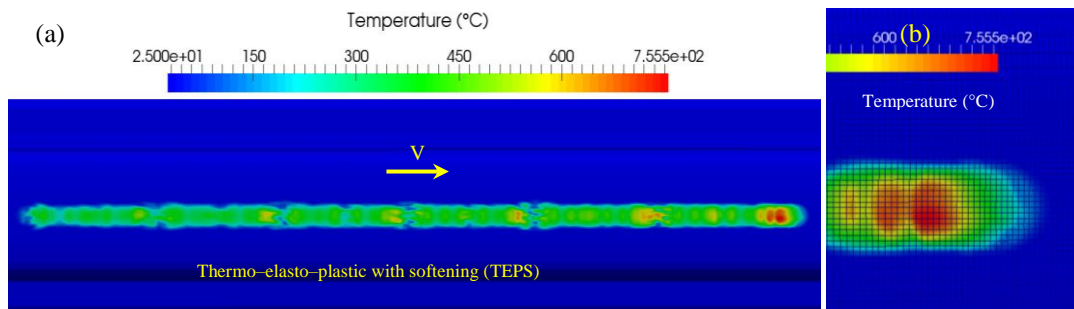


Figure 2.7. Distribution of the rail surface temperature at  $t = 11.52$  ms; the results are obtained for the TEPS model with 26% creepage; (a) full distribution in the rail top–view; (b) magnification around the contact patch

The results of the three creepage scenarios (10, 18 and 26%) were obtained to investigate the effect of creepage on the stress results and temperature. Figure 2.8(a) shows the temperature distributions along the rail under different creepage scenarios. All the results are obtained for TEPS. Figure 2.8(b) shows the history of V–M stress in a rail surface element at  $x = 0.45$  m. According to Figure 2.8(a), the rail temperature is significantly influenced by creepage; the peak temperatures were 284 °C 498 °C and 756 °C for the creepage of 10%, 18% and 26%, respectively. As can be seen in Figure 2.8(b), the residual V–M stresses in the rail material were also increased at higher creepages (the trend was less significant than that of temperature). In contrast, creepage had a negligible effect on the peak V–M stresses. These results suggest that a high creepage of 26% increases the flash–temperature (in a significant manner) and residual stresses (to the lower extent), while it has negligible influence on the peak stresses.



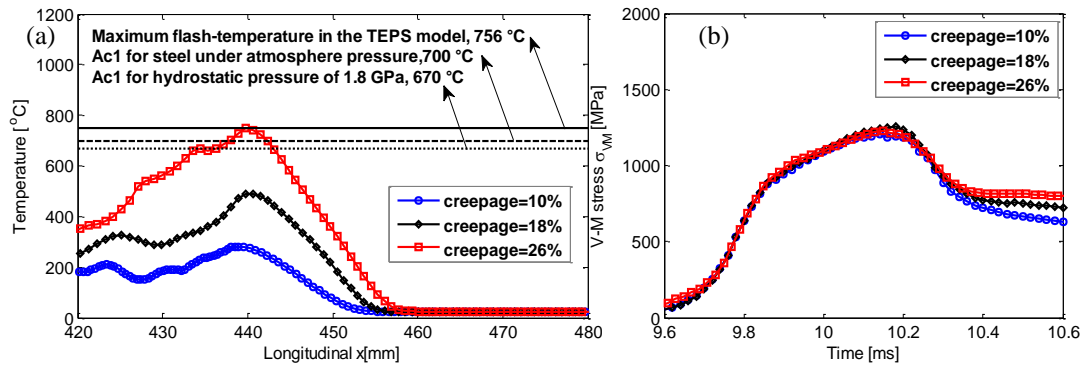


Figure 2.8. (a) Temperature distributions in the rail surface along the  $x$  axis for TEPS under three different creepage scenarios i.e. 10%, 18% and 26%; (b) history of V–M stress in a rail surface element at  $x = 0.45$  m,  $y = 0$  with different creepage scenarios

Thermodynamic calculations were performed in [44] to compute the critical phase transformation temperatures. The equilibrium quasi–binary iron–carbon phase diagrams were calculated at atmospheric pressure and at a hydrostatic pressure of 1.8 GPa. According to these calculations, the minimum temperature for austenite to form,  $A_{c1}$ , is 700 °C at atmospheric pressure. At the hydrostatic pressure of 1.8 GPa, the  $A_{c1}$  temperature shifts to 670 °C. These temperature boundaries are superimposed in Figure 2.8(a). As shown in this figure, the maximum flash temperature obtained for TEPS with 26% creepage (756 °C) was higher than both the  $A_{c1}$  estimated at atmosphere pressure (700 °C) and the one calculated at the hydrostatic pressure of 1.8 GPa (670 °C). This temperature calculation confirms the possibility of forming hard and brittle martensite on the rail surface due to frictional heat in the wheel–rail contact with a high creepage (26% for TEPS). This is also in good agreement with observations made in [44], where WEL formation by martensitic transformation is simulated in laboratory conditions.

Creepage as high as 26% has been measured in some passenger trains of the Dutch railway and high occurrence of squats have been reported in the railway tracks, for which, these passenger trains being in–service. This indicates that the chosen creepage of 26% and the resulting peak temperature of 756 °C can potentially happen in the Dutch railway.

The following explanation about the WEL formation is important. The formation of WEL by plastic deformation has also been reported in the literature. The research by [45] investigates the nature of different WELs induced either by thermal or by severe plastic deformation. The latter WEL contains nano-crystalline supersaturated Fe-C. The results in [44] shows a strong indication of WEL being formed by high temperature and not by severe plastic deformation. A recent study by [46] introduces electrical current leaking as an alternative formation mechanism for thermally induced WELs. According to this research, both electrical arcing induced WELs and the WELs induced by high slip comprise similar microstructures.

#### 2.4.2 Potential of fatigue at subcritical temperatures

Formation of WEL via martensitic phase transformation at supercritical temperatures (above 700 °C as shown in Figure 2.8) can reduce the rail lifetime. This is because WEL may promote the initiation of RCF cracks due to the brittle nature of martensite. The close relationship between WEL and RCF cracks has been reported in a number of studies e.g. [47]. Hence, elevated temperature and formation of WEL can be a possible explanation for RCF initiation.

A creepage as high as 26% is not the typical of railway operation, though it might locally happen in the wheel–rail contact when the trains accelerate or decelerate. Temperature rise and thermal effects can also be important at subcritical temperatures (below 700 °C). Let us

consider a more general case of the temperature rise calculated with  $s = 18\%$ . The rail temperature, in this case, was obtained up to  $498\text{ }^\circ\text{C}$ , see Figure 2.6 and Table 2.5 (for TEPS which is the most advanced material model). This temperature is lower than the critical phase transformation temperature.

The evolution of the V–M stresses and strains in the rail during an entire contact cycle is shown in Figure 2.9. The results were obtained for all the material models i.e. E, ET, EP, TEP and TEPS. For clarity, the results of thermal and isothermal models are shown separately.

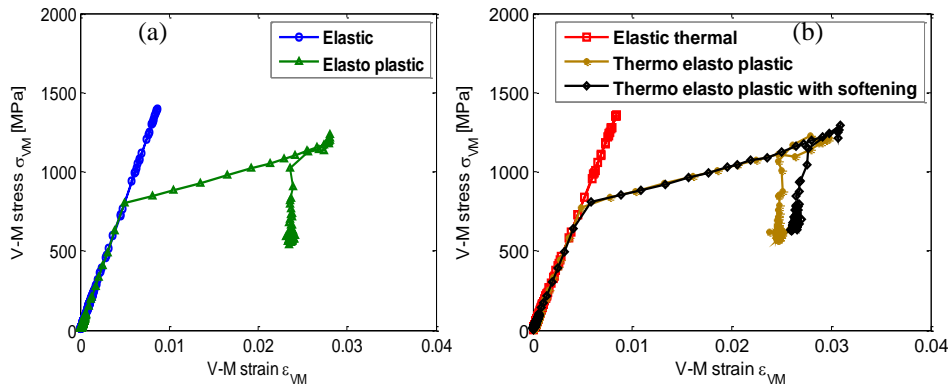


Figure 2.9. Evolution of the V–M stresses and strains in a rail element on the surface (number 827719) for the (a) isothermal material models (Elastic and Elasto–plastic); (b) thermal material models (Elastic thermal, Thermo–elasto–plastic and Thermo–elasto–plastic with softening) during the entire contact cycle with  $s = 18\%$ .

As can be seen in Figure 2.9, the magnitudes of effective residual stress and plastic strain in the TEPS model are the greatest among the different models. This is due to the significant thermal effects i.e. the inclusion of thermomechanical coupling and thermal softening (temperature dependency) in the TEPS model.

Without thermal effects (the case of EP), the rail material showed lower plastic strain than the thermal cases, though, the material still had high plastic deformation due to the severe loading considered in this research. When thermal coupling and thermal softening are both involved (the case of TEPS), materials appeared to be less resistant to RCF. Thermal effects, on the one hand, cause a reduction in the elastic and shakedown limits due to thermal softening; see the temperature dependency of  $\sigma_y$  in Table 2.1. Therefore, yielding begins at lower stress levels. On the other hand, when thermal stresses are superimposed on the mechanical contact stresses, higher peak and residual stresses and strains were expected. This synchronization effect i.e. the lower yielding limits and higher stresses can lead to earlier RCF damage.

The influence of yield strength of rail steel on the outcome can be explained by the mentioned mechanism. A higher yield strength will increase the peak temperature of the wheel tread and rail surface at high creepage conditions; see e.g. Figure 2.6, in which, the maximum rail temperature occurs in the elastic case and the minimum in TEPS. This means that under the high slip (creepage) loading conditions, the higher yield strength is less desirable because it can increase the chance of martensitic transformation at supercritical temperatures.

At subcritical temperatures, however, the higher yield strength is more desirable with regard to the rail shakedown behaviour. When the applied stresses are lower than the yield strength of the rail steel, no plastic strain will occur in the material. Plastic flow and strain-hardening will start in materials when stress exceeds the yield strength. The higher yield strength (normally the case for the higher steel grades) causes a lower plastic strain; under this situation, materials appeared to be more resistant to the RCF initiation. This indicates that, when there is a low risk of high temperature (around  $700\text{ }^\circ\text{C}$ ), a higher steel grade (with

higher yield strength) is more RCF resistant. The work hardening effect is similar to the mentioned effect for the yield strength. A higher work hardening is, thus, more desirable considering the rail shakedown behaviour.

## 2.5 Conclusions

To quantify the temperature rise and thermomechanical stresses in the wheel–rail contact problem, a coupled thermomechanical modelling procedure was developed. Different material models with various thermal and mechanical properties were examined. TEPS was the most advanced material model, for which, thermomechanical coupling and temperature–dependency of materials were considered. The numerical model was able to calculate the stresses, deformations and temperatures under various creepage scenarios. Based on the results, the following conclusions are drawn:

- 1) The comparison between the purely mechanical and the coupled thermomechanical solver revealed that the coupling solver produces higher peak stresses and higher plastic deformations in the rail material. (TEPS vs. EP).
- 2) The comparison between the temperature–independent and the thermal–softened material revealed that thermal softening causes higher von–Mises stresses and higher plastic deformations in materials (TEPS vs. TEP).
- 3) Among the different nonlinear material models, TEPS produced the highest equivalent von–Mises stress and the highest plastic deformation. It happened due to the combined effects of thermal softening and thermal coupling, which caused higher thermal stresses. These stresses were superimposed on the mechanical contact stresses and amplified the total stresses.
- 4) Among the different thermal models, TEPS produced the least flash–temperature (498 °C) in the rail surface. This happened because, in this model, a higher fraction of the total energy contributed to form the high plastic deformation.
- 5) A nearly equal temperature rise was seen in the contact patch of the wheel and rail since the heat (generated due to friction) was equally distributed between the wheel and rail during the thermomechanical coupling.
- 6) The temperature distribution in the wheel and rail surface consisted of two regions i.e. a rapid increase in the contact patch and a fast decay in the opposite side of the running direction. The peak occurred near the trailing edge of the contact patch. Some local peaks occurred in the decay region due to contact force fluctuations, caused by dynamic interaction between the wheel and track system.
- 7) The temperature in the wheel–rail contact was significantly influenced by creepage; for the creepage of 10%, 18% and 26%, the peak temperatures were 284 °C 498 °C and 756 °C, respectively. The higher creepage increased the flash–temperature (in a significant manner) and residual stresses (to the lower extent), while it had negligible influence on the peak von–Mises stresses.
- 8) The peak temperature in the rail surface calculated for the 26% creepage (756 °C) was sufficient to transform pearlite to austenite. According to equilibrium quasi–binary iron–carbon phase diagrams, the temperature above 700 °C was considered as the supercritical temperature, at which, the potential of WEL formation via martensitic phase transformation was confirmed. Creepage as high as 26% has been measured in some passenger trains of the Dutch railway and high occurrence of squats have been reported in the rails, on which, these passenger trains being in–service.
- 9) Thermal effects were also important at subcritical temperatures (below 700 °C). Thermal effects, on the one hand, caused a reduction in the elastic and shakedown limits, due to thermal softening. On the other hand, when thermal stresses were

superimposed on the mechanical contact stresses, higher stresses and deformations were expected. The results indicated a synchronization effect i.e. the lower yielding limits and higher stresses, which will cause earlier RCF damage.

The high temperature and the mentioned synchronization effect might explain the formation of squat defects. To verify this, further research using thermomechanical modelling and microstructural observations of the defected rails will be needed in future.

## 2.6 References

- [1] J. Ahlström & B. Karlsson, Modelling of heat conduction and phase transformations during sliding of railway wheels, *Wear*, 253 (2002) 291–300.
- [2] M. Fec & D. Utrata, Elevated temperature fatigue behavior of class B, C and U wheel steels, in: *Proceedings of the ASME Rail Transportation Spring Conference*, 1985, 33–39.
- [3] G. Bartley, A practical view of wheel tread shelling, in: *Proceedings of the Ninth International Wheelset Congress*, Montreal, Canada, 1988, 5.1.1–5.1.4.
- [4] A. Ekberg & E. Kabo, Fatigue of railway wheels and rails under rolling contact and thermal loading—an overview, *Wear*, 258 (2005) 1288–1300.
- [5] A. Haidari & P. Hosseini–Tehrani, Fatigue Analysis of Railway Wheels Under Combined Thermal and Mechanical Loads, *Journal of Thermal Stresses*, 37 (2014) 34–50.
- [6] L. Wu, Z.F. Wen, W. Li & X.S. Jin, Thermo–elastic–plastic finite element analysis of wheel/rail sliding contact, *Wear*, 271 (2011) 437–443.
- [7] D.F. Cannon & H. Pradier, Rail rolling contact fatigue – Research by the European Rail Research Institute, *Wear*, 191 (1996) 1–13.
- [8] J.W. Ringsberg, Life prediction of rolling contact fatigue crack initiation, *International Journal of fatigue*, 23 (2001) 575–586.
- [9] M. Ertz & K. Knothe, Thermal stresses and shakedown in wheel/rail contact, *Archive of Applied Mechanics*, 72 (2003) 715–729.
- [10] A. Böhmer, M. Ertz & K. Knothe, Shakedown limit of rail surfaces including material hardening and thermal stresses, *Fatigue & Fracture of Engineering Materials & Structures*, 26 (2003) 985–998.
- [11] D.I. Fletcher & S.H. Sanusi, The potential for suppressing rail defect growth through tailoring rail thermomechanical properties, *Wear*, 366–367 (2016) 401–406.
- [12] S.L. Grassie, D.I. Fletcher, E.A. Gallardo Hernandez & P. Summers, Studs: a squat–type defect in rails, *Proceedings of the Institution of Mechanical Engineers, Part F: Journal of Rail and Rapid Transit*, 226 (2012) 243–256.
- [13] S. Pal, C. Valente, W. Daniel & M. Farjoo, Metallurgical and physical understanding of rail squat initiation and propagation, *Wear*, 284 (2012) 30–42.
- [14] H. Zhang, S. Ohsaki, S. Mitao, M. Ohnuma & K. Hono, Microstructural investigation of white etching layer on pearlite steel rail, *Materials Science and Engineering: A*, 421 (2006) 191–199.
- [15] G. Baumann, H. Fecht & S. Liebelt, Formation of white–etching layers on rail treads, *Wear*, 191 (1996) 133–140.
- [16] C. Bernsteiner, G. Müller, A. Meierhofer, K. Six, D. Künstner & P. Dietmaier, Development of white etching layers on rails: simulations and experiments, *Wear*, 366–367 (2016) 116–122.
- [17] X. Zhao & Z. Li, The solution of frictional wheel–rail rolling contact with a 3D transient finite element model: Validation and error analysis, *Wear*, 271 (2011) 444–452.
- [18] Z. Wei, Z. Li, Z. Qian, R. Chen & R. Dollevoet, 3D FE modelling and validation of frictional contact with partial slip in compression–shift–rolling evolution, *International Journal of Rail Transportation*, 4 (2016) 20–36.

- [19] Z. Yang, Z. Li & R. Dollevoet, Modelling of non-steady-state transition from single-point to two-point rolling contact, *Tribology International*, 101 (2016) 152–163.
- [20] M.A. Tanvir, Temperature Rise Due to Slip between Wheel and Rail – an Analytical Solution for Hertzian Contact, *Wear*, 61 (1980) 295–308.
- [21] K. Knothe & S. Liebelt, Determination of temperatures for sliding contact with applications for wheel rail systems, *Wear*, 189 (1995) 91–99.
- [22] F.D. Fischer, E. Werner & W.Y. Yan, Thermal stresses for frictional contact in wheel-rail systems, *Wear*, 211 (1997) 156–163.
- [23] W.W. Chen & Q.J. Wang, Thermomechanical Analysis of Elastoplastic Bodies in a Sliding Spherical Contact and the Effects of Sliding Speed, Heat Partition, and Thermal Softening, *Journal of Tribology*, 130 (2008) 041402.
- [24] A.M.S. Asih, K. Ding & A. Kapoor, Modelling the Effect of Steady State Wheel Temperature on Rail Wear, *Tribol Lett*, 49 (2013) 239–249.
- [25] K.D. Vo, A.K. Tieu, H.T. Zhu & P.B. Kosasih, The influence of high temperature due to high adhesion condition on rail damage, *Wear*, 330–331 (2015) 571–580.
- [26] M. Ertz & K. Knothe, A comparison of analytical and numerical methods for the calculation of temperatures in wheel/rail contact, *Wear*, 253 (2002) 498–508.
- [27] I. Çaldichoury, F. Del Pin, P. L'Eplattenier, D. Lorenz & N. Karajan, Coupling possibilities in LS-DYNA: Development status and sample applications, in: *NAFEMS Eroupean Conference: Multiphysics Simulation*, Frankfurt, Germany, 2012, 1–44.
- [28] X. Deng, Z. Qian & R. Dollevoet, Lagrangian Explicit Finite Element Modeling for Spin-Rolling Contact, *Journal of Tribology*, 137 (2015) 041401.
- [29] J. Hallquist, G. Goudreau & D. Benson, Sliding interfaces with contact-impact in large-scale Lagrangian computations, *Computer methods in applied mechanics and engineering*, 51 (1985) 107–137.
- [30] Z. H. Zhong, *Finite element procedures for contact-impact problems*, Oxford University Press, Oxford, New York, 1993.
- [31] T. Belytschko, W.K. Liu & B. Moran, *Nonlinear finite elements for continua and structures*, Wiley, Chichester, New York, 2000.
- [32] *LS-DYNA Thermal analysis user guide*, Livermore Software Technology Corporation (LSTC Inc.), Livermore, USA, 1999.
- [33] M. Furuichi & D.A. May, Implicit solution of the material transport in Stokes flow simulation: Toward thermal convection simulation surrounded by free surface, *Computer Physics Communications*, 192 (2015) 1–11.
- [34] R. Courant, K. Friedrichs & H. Lewy, On the partial difference equations of mathematical physics, *Mathematische Annalen*, 11 (1928) 215–234.
- [35] R. Stout, P.D. Billings & P. Semiconductor, Accuracy and time resolution in thermal transient finite element analysis, in: *ANSYS™ Users Conference*, 2002.
- [36] M.N. Özışık, *Heat conduction*, John Wiley & Sons, 1993.
- [37] J.O. Hallquist, *LS-DYNA theory manual*, Livermore software technology corporation, 3 (2006) 25–31.
- [38] A. Bower & K. Johnson, The influence of strain hardening on cumulative plastic deformation in rolling and sliding line contact, *Journal of the Mechanics and Physics of Solids*, 37 (1989) 471–493.
- [39] B. Talamini, J. Gordon & A.B. Perlman, Investigation of the effects of sliding on wheel tread damage, in: *ASME 2005 International Mechanical Engineering Congress and Exposition*, American Society of Mechanical Engineers, 2005, 119–125.
- [40] C. Esveld, *Modern railway track*, Second ed., MTR-Productions, Zaltbommel, The Netherlands 2001.

- [41] K. Mädler, A. Zoll, R. Heyder & M. Brehmer, Rail Materials -Alternatives and Limits. 8th World Congress on Railway Research, 2008 (WCRR2008), Seoul, Korea. 132.
- [42] Z. Yang, X. Deng & Z. Li, Numerical modeling of dynamic frictional rolling contact with an explicit finite element method, *Tribology International* 129 (2019) 214-231.
- by electrical leakage between wheel and rail, *Tribology International* 140 (2019) 105875.
- [43] X. Zhao & Z. Li, A three–dimensional finite element solution of frictional wheel–rail rolling contact in elasto–plasticity, *Proceedings of the Institution of Mechanical Engineers, Part J: Journal of Engineering Tribology*, 229 (2014) 86–100.
- [44] J. Wu, R.H. Petrov, M. Naeimi, Z. Li, R. Dollevoet & J. Sietsma, Laboratory simulation of martensite formation of white etching layer in rail steel, *International Journal of Fatigue*, 91 (2016) 11–20.
- [45] A. Al-Juboori, D. Wexler, H. Li, H. Zhu, C. Lu, A. Mccusker, J. Mcleod, S. Pannila & Z. Wang, Squat formation and the occurrence of two distinct classes of white etching layer on the surface of rail steel, *International Journal of Fatigue*, 104 (2017) 52-60.
- [46] A. Al-Juboori, H. Zhu, D. Wexler, H. Li, C. Lu, A. A. Gazder, J. Mcleod, S. Pannila & J. Barnes, Microstructural changes on railway track surfaces caused by electrical leakage between wheel and rail, *Tribology International* 140 (2019) 105875.
- [47] P. Clayton & M. Allery, Metallurgical aspects of surface damage problems in rails, *Can Metall Quart*, 21 (1982) 31–46.



# 3

## Chapter 3 A new test rig for experimental study of the wheel–rail contact

*In the previous chapter, the basic principles of the thermomechanical wheel–rail contact were outlined, along with synthesising possible hypothesises for squat formation. As the existing testing facilities fail to deal with squats, this chapter introduces a brand–new testing setup, needed to investigate the RCF problem in wheel–rail materials.*

*In Section 3.2, the existing experimental setups and testing strategies for wheel–rail contact studies are overviewed. Based on this survey, an optimal operational mechanism for the new test rig is selected. Section 3.3 addresses the development process of the test rig based on the undertaken literature review. Section 3.4 summarizes the results and provides the readers with the final choice for the test rig. Afterwards, detailed specifications and design configurations of the setup are determined using scaling laws and similarity analysis. In Section 3.5, the results of some real experiments carried out using the newly–built setup are presented.<sup>1</sup>*

---

<sup>1</sup> This chapter is based on the following publication:

*M. Naeimi, Z. Li, R.H. Petrov, J. Sietsma & R. Dollevoet, Development of a new downscale setup for wheel–rail contact experiments under impact loading conditions, Experimental Techniques, 42 (2017) 1–17.*



### 3.1 Introduction

Railways and especially high-speed trains are popular transportation modes due to being sustainable, economical and environmentally friendly. Rolling contact fatigue (RCF) is an important degradation source of the wheel and rail materials in the railway industry. In the past few decades, researchers have attempted to identify the physical mechanisms involved in RCF of rails and wheels and proposed diverse models to predict their fatigue life; see e.g. [1–3]. Such studies and many other examples have substantially contributed to the prediction of the lifetime of rails and wheels and to optimization of maintenance strategies by avoiding or delaying RCF.

Although detailed models of the wheel–rail contact and damages, as well as vehicle–track interaction have been developed, further field characterization and experimental verifications are needed to better understand the root causes of the RCF. These include the development of repeatable testing methodologies that can manifest the true states of contact stresses of the wheel–rail system and reveal the actual causality of microstructure changes under realistic loading conditions. To such end, a new test rig is developed in the current research. The aim is to provide a brand–new test facility, which enables the researchers to generate RCF of rails and wheels under scaled and controlled laboratory conditions. With this rig we intend to provide the following four functional goals: 1) to examine the validity of the various hypotheses on damage occurrence; 2) to gain new insight into damage mechanisms from the extended viewpoint of mechanical loading and material properties at macro level and at the microstructure scale; 3) to test material performance for damage resistance and 4) to support the development of new materials and damage prediction models. The present study addresses how the new setup can fulfil the above–mentioned four functionality requirements. The damages include plastic deformation, wear and RCF. In particular, the focus of the new test rig will be on impact–induced RCF defects such as squats, as they involve all these damages [4]. The test rig can also be applied to other similar defects (in terms of their dynamic loading) like poor insulation joints, wheel flats and wheel burns, poor welds and corrugation [4, 5]. It is expected that tests for other types of RCF, e.g. head–checking, can also be conducted, if the loading is reduced to a (quasi–) static state.

High–frequency dynamics of wheel–rail and train–track interaction is not yet well understood. It mostly has to do with wheel–rail dynamic contact and is very much determined by the track flexibility and nonlinearities, effects of which are mostly not yet well established. One specific example is corrugation, which not only causes acoustic noises, but RCF (squats) and damages fastening. This might lead to chain effects as many fastenings might break one after another in a short time between inspection intervals and thus might cause a catastrophic derailment, as well as fast degradation of ballast/slab and other components. The new test setup can test almost any type of track structures e.g. ballast track, slab track, embedded track with including their real material nonlinearities.

This chapter first briefly reviews the existing rigs that can be used for general wheel–rail contact studies. The chapter further assesses the suitability of the existing experimental setups for research on impact–induced RCF defects. This evaluation leads to three preferred experimental techniques, which are then further assessed in more detail. Consequently, an optimum mechanism is achieved through technical evaluations and synthesis of the structures, characteristics and performance. Afterwards, specifications of the new test setup are described and some results of dynamic measurements are presented. Experimental observations in the test setup are finally compared with those of the real–life railway to reveal dynamic similarities and to see the potentials for screening RCF in the new rig.

### 3.2 Review of the existing test rigs for wheel–rail contact studies

Various experimental techniques were proposed in the literature for wheel–rail contact studies. The testing procedures for fatigue testing of metals are fairly established in terms of methodologies, instruments and the applications. Some experimental methods were introduced for RCF experiments in bearing steels. A collection of methodologies devoted substantially to rolling bearings were presented in [6]. In contrast to rolling bearings, the experimental methods for assessing RCF in wheel–rail materials, involved much uncertainty about the functionality of different techniques and their effectiveness. Table 3.1 summarises a list of various test rigs for wheel–rail contact investigations either within full–scale or reduced–scale configurations in the literature. The scale parameter in this table indicates the overall scale of the wheel (its diameter) relative to the standard railway wheel.

Table 3.1. A list of available test rigs for wheel–rail contact studies

No.	Name of the testing setup	Scale	Owner	Location
1	Vehicle/Bogie Roller Rig [7]	1:1	Deutsche Bahn AG (DB AG)	Munich–Freimann, Germany
2	Full–scale Roller Rig [8]	1:1	Southwest Jiaotong University (SWJTU)	Chengdu, China
3	DTR Dynamic Train Bogie Test Rig [9]	1:1	Danobat Group, Railway Unit	Elgoibar, Spain
4	Full–scale Roller Stand [10]	1:1	National Traffic Safety & Envir. Lab. (NTSEL)	Tokyo, Japan
5	Wheel–Rail Test Rig [11]	1:1	University of Sheffield (formerly RSSB)	Sheffield, UK
6	Full–scale Rail Wheel Test Rig [12]	1:1	Voestalpine Schienen (VAS)	Leoben, Austria
7	Wheelset Roller Rig [13]	1:1	Deutsche Bahn AG (DB AG)	Munich, Germany
8	Wheel Test Rig [7]	1:1	Fraunhofer Institut Betriebsfestigkeit (FIB)	Darmstadt, Germany
9	BU300 Roller Rig [14, 15]	1:1	Lucchini C.R.S	Lovere, Italy
10	Naples Vehicle Roller Rig [16]	1:1	Ansaldo Transport Research Centre	Naples, Italy
11	Osmannoro Full–scale Roller Rig [17]	1:1	Osmannoro Research Centre	Florence, Italy
12	Reduced–scale Rolling Rig [18, 19]	1:3	TNO–TPD	Delft, Netherlands
13	Wheel/Rail Tribological Rolling Rig [20]	1:4	Southwest Jiaotong University	Chengdu, China
14	UNSW Wheel–Rail Rolling Rig [7]	1:5	University of New South Wales	Sydney, Australia
15	Scale Roller Rig [21]	1:5	University of Huddersfield (formerly MMU)	Huddersfield, UK
16	Twin–Disk Rig [22]	1:3	University of Huddersfield (formerly MMU)	Huddersfield, UK
17	Two–Disc Test Rig [23]	~1:5	University of Queensland	Sydney, Australia
18	Scaled–Bogie Test Bench [24]	1:5	Université Catholique de Louvain	Louvain, Belgium
19	SUROS Twin–Disk Test Machine [25]	~1:20	Sheffield University Rolling Sliding	Sheffield, UK
20	ISVR Wheel–Rail Test Rig [26, 27]	1:5	Institute of Sound & Vibration Research	Southampton, UK
21	BCRRE Spinning Rail Test Rig [28]	~1:7	University of Birmingham	Birmingham, UK
22	INRETS Bogie Test Rig [29, 30]	1:4	French Transport Research Institute (INRETS)	Grenoble, France
23	Scaled Wheelset Roller Stand [31]	1:5	National Traffic Safety & Environ. Lab. (NTSEL)	Tokyo, Japan
24	Oerlikon Test Machine [32]	~1:10	Delft University of Technology	Delft, Netherlands
25	Scaled wheel on rail track–wheel Test Rig [33]	1:3	Cranfield University	Cranfield, UK
26	Twin–Disc Rolling–Sliding Machine [34]	~1:2	Railway Technical Research Institute	Tokyo, Japan
27	Twin–Disc Machine [35]	1:2– 1:4	East Japan Railway Company (JR East)	Saitama, Japan
28	Scaled Roller Test Rig [36]	1:5	MDM Lab	Pistoia, Italy
29	Scaled Bogie on Rollers [37]	~1:5	Delft University of Technology	Delft, Netherlands

Looking at the scale parameter in Table 3.1, the existing test rigs can be classified into two main categories: Full-scale and reduced-scale. General classification of the existing test rigs is shown in Figure 3.1. According to this figure, six general categories are defined: 1) Full-size vehicle/ bogie, 2) Full-size wheel-on-roller, 3) Full-size wheel-on-straight, 4) Twin-discs, 5) Scaled wheel on rail track ring and 6) Scaled wheel on the straight track.

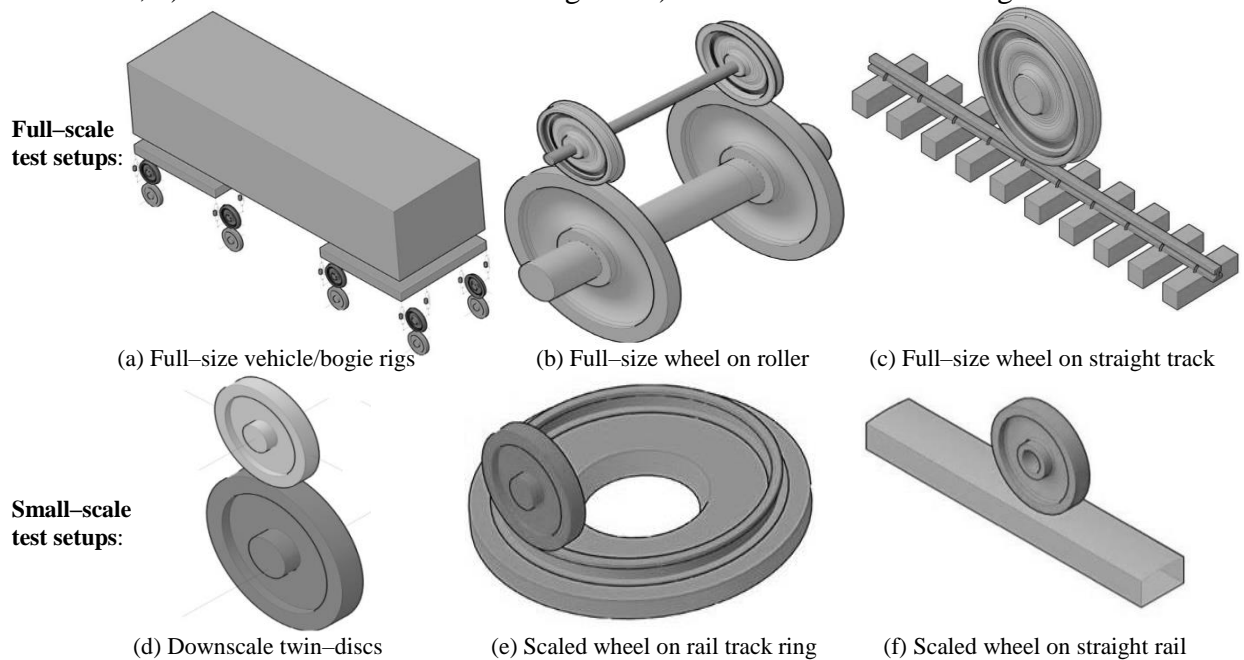


Figure 3.1. Classification of possible test rig mechanisms for wheel-rail contact studies

A comparative evaluation is carried out in the following, to select an optimum category for the new test rig in this research. Although any of these six categories is able to simulate some aspects of the rolling contact problem, some specific demands are defined for the new test rig to evaluate the six categories. Compliance of the above-mentioned categories is evaluated toward these criteria.

### 3.2.1 High-frequency vibrations

It has commonly been agreed by [38–42] that the primary suspension of a railway vehicle plays a more significant role in the wheel-rail interaction problem than the secondary suspension. Hence, the secondary suspension of the vehicle can be handled with less detail in order to develop a new rig for the wheel-rail contact problem. This simplification is acceptable because the vibration of the sprung mass has a negligible effect on dynamic properties of the wheel-rail contact problem. This is because the wavelength of vibrations of the sprung mass, in the order of meters, is much longer than the size of contact patch between the wheel and rail [42, 43]. This means that for the purpose of high-frequency dynamic investigation in the wheel-rail contact, it is not essential to include the vehicle or bogies with their complex configurations into the testing procedure. Thus, the mass of the vehicle system can be lumped above the wheel component, where it is supported by a group of springs and dampers of the vehicle's primary suspension; see Figure 3.2. In order to manifest high-frequency dynamics in the test rig, it is of major importance to include the required flexibilities and nonlinearities in the wheel-rail dynamic contact problem. This can be achieved by using identical material properties for the wheel-track system. The majority of the existing test rigs are used to study the wear in wheel-rail materials or to examine the head-checks which happen due to quasi-static loading [44]. Although the new test rig is

developed to study all the major types of RCF defects, the main focus is on squats, which are associated with high–frequency dynamics in the wheel–track system.

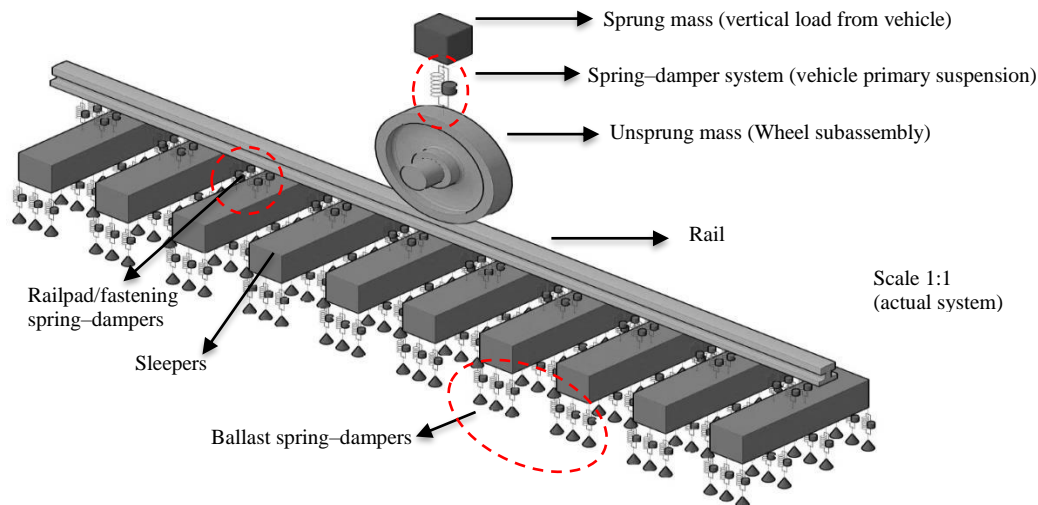


Figure 3.2. Dynamic model of the vehicle–track system with simplification in vehicle structure and with detailed modelling of the track to manifest high–frequency vibrations in the test environment

### 3.2.2 Details down to track components

In a typical ballasted railway track, the support system is composed of fastenings, sleepers and ballast layer. Field observations have shown that the wheel–rail dynamic forces can be directly transferred from the contact interface to the track components and exacerbate the deterioration rate of the track components [45, 46]. Conversely, the presence of defects and imperfections in track components can also contribute to high–frequency vibrations of the wheel–track system [43, 47]. The results of vehicle–track dynamic simulations in [48] show that the presence of singular rail surface defects (squat for instance) can significantly increase high–frequency dynamic forces between the wheel and rail. Furthermore, the stiffness and damping properties of rail fasteners, and in particular the railpads, have been shown to play an important role in dynamic behaviours of the railway system, especially in the high–frequency range [49]. Some surveys such as [50, 51] have examined the relationship between the track geometry and the formation of RCF defects, where track maintenance was also found to be related to RCF initiation. Such studies indicate the importance of incorporating the major track components to deal with impact–loading conditions. The term “impact” is used here to characterise the short period and highly dynamic wheel–rail contact at irregularities in the wheel/rail surface such as indentation, squats, rail joint, wheel flat or other defects. Such term has also been used for the same purpose by other researchers; see e.g. [39, 46]. It is possible to create all of these (irregularities, joints, track defects, etc.) in the wheel–track components of the new test rig. This enables us to study the wheel–track system similar to the real life.

### 3.2.3 Scaling concept

From a general standpoint, reduced–scale testing generally costs less and is more convenient to conduct than the full–scale testing. Furthermore, for the present research, monitoring and controlling the effective factors on the RCF problem necessitate a large number of tests to be carried out. In a reduced–scale setup, of course, it would be easier and less costly to implement a wider range of tests. On the other hand, a full–scale test rig may incorporate the whole body of the railway vehicle (Figure 3.2), which is more realistic from the vehicle

dynamics point of view. The major concern about the scaled test rigs is the uncertainty about the equivalency of the system when the scaling is applied. For this reason, researchers often argued the similarity issues of the scaled test rigs. Various similarity strategies of the scaled test rigs were discussed in [30, 52], indicating their benefits and limitations. Another example of the similarity analysis on the parameters of a wheel–track test rig is provided in [53]. A more recent study [54], reports the application of similarity law for a small–scale derailment simulator. By using a suitable scaling strategy, it is plausible to derive the parameters of the new test rig equivalent to the real–life system.

#### 3.2.4 *The ring track mechanism*

A fundamental limitation of the test rigs with straight track mechanisms (Figure 3.1(c, f)) is the low rolling speed of the wheel. This is because the wheel cannot continuously run over the rail and thus it has to move back and forth in a cyclic manner to simulate the repeated contact. With such a mechanism, a realistic simulation of the vehicle–track system will be difficult to achieve. It also causes un–realistic transient non–steady state, making required test conditions disturbed or needing a long time to achieve. Furthermore, it is more demanding on the loading and running mechanism. Hence, to provide repeated contact condition with an acceptable range of speed and realistic transient state of the system under unidirectional rolling, it is almost unavoidable to use a rail with a circular shape, either with disc or ring. This is the main reason why many of the existing rigs simulate track with the disc, roller or ring.

Continuous rolling contact can also be achieved by the simple twin–disc strategy, where the rail–disc and wheel–disc drive with opposite angular velocities against each other; see Fig 3.1(d). However, the behaviour of the rail track is neglected in such a mechanism as the track is excluded. Lack of similarity in dynamic characteristics of the vehicle–track system and its flexibility features are the major limitations of the twin–disc categories. Therefore, the rail disc mechanism cannot fulfil the requirements needed for RCF tests in the current research. By employing a bent track structure (ring track), it is possible to provide the test rig with a continuous rolling contact, while the important dynamic analogies are maintained.

By evaluating the mentioned six categories toward the prescribed requirements, one category provides more advantages for developing a new rig for the wheel–rail contact studies. This category is the scaled wheel on a scaled rail track ring (Figure 3.1(e)). The main advantages are: 1) It uses a reduced–scale strategy to benefit from the reduced–scale experiments i.e. convenience, cost effectiveness, operational safety, flexibility etc.; 2) The level of simplification on the vehicle is up to primary suspensions, which is adequate for the purpose of the wheel–rail contact research; 3) All components of the track system are incorporated, contributing to the dynamic properties of the wheel–rail contact problem; 4) A continuous rolling contact can be simulated due to the ring–shaped application. Table 3.2 summarizes the beneficial assets that can be achieved with the selected category. The table also gives some design features that need to be considered to fulfil the prescribed requirements.

Table 3.2. Benefits for the selected category (the scaled wheel on the rail track ring)

Benefits of the selected category	Features to be seen in the design process of the new rig
- Vibration equivalency	- Parameters of the new test rig (dimensions, speed, loads, stiffness, damping, etc.) need to be properly designed to reach vibration equivalency between the tests and the real system.
- Acceptable level of simplification in the vehicle	- Outputs of the tests (deformations, forces, accelerations, frequencies, wavelength, stress/strain responses etc.) should be comparable with respect to the real system.
- Consideration of the track components	- The ring–shaped rail track needs to be properly designed, ensuring that residual stresses will not affect the testing.
- Downscale mechanism	
- Effective for RCF tests	
- Continuous rolling contact	
- Acceptable operational speed	

### 3.3 Development of the new rig under the selected category

Based on the above discussion, the qualified category is a downscale wheel–track mechanism consisting of equivalent components of an actual railway system. The vehicle primary suspension and the track components need to be incorporated, (Figure 3.2) to simulate analogical behaviours of the vehicle–track system. In the following, further assessment is undertaken on the selected category. The stable positioning of the wheel–track system in the selected category can be provided through different mechanisms. Three alternatives within this category are defined as shown in Figure 3.3. The track structure in all the alternatives consists of rail, fastenings, sleepers and ballast. The track assembly is stationary in all the three alternatives, while the wheel assembly rolls over the rail.

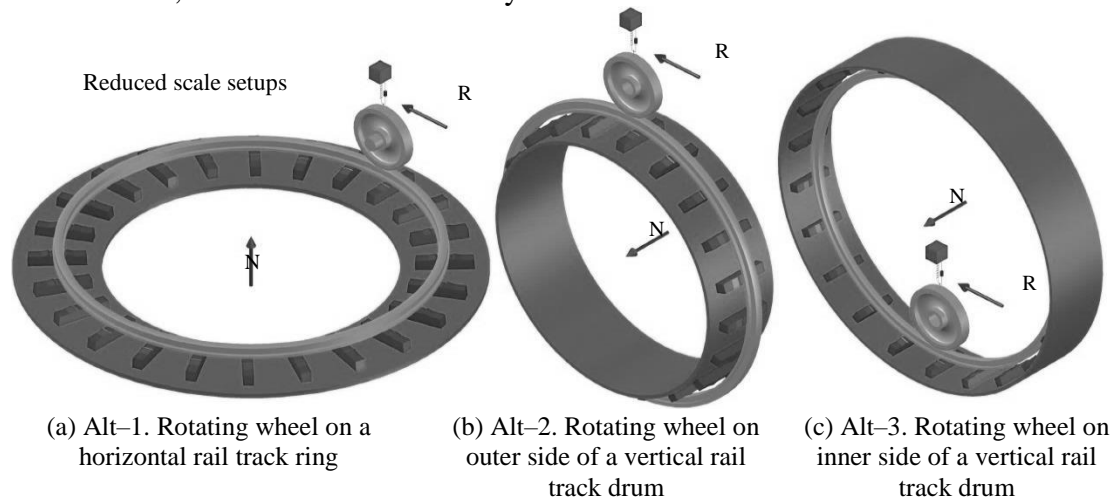


Figure 3.3. Schematic view of the three plausible alternatives within the qualified category; RD = rolling direction, NT = normal track vector

In the following sections, these three alternatives are comparatively assessed from the structural and mechanical viewpoints to determine the most suitable one. The Finite element method (FEM) is employed to assess the alternatives under the rolling contact condition.

#### 3.3.1 Scalability in the new test rig

Scalability is a fundamental subject when dealing with downscale test setups. The scale factor defines the dimensions and it affects the parameters of the components in the test setup. The choice of material properties is also an important factor in the scaling problem. The starting point for the scalability in this research is to keep similarity of the wheel–track system to the real–life one. To achieve this, a linear geometric scaling, i.e. applying a particular scale factor on all dimensions is used, whereas the material properties are kept the same. References [29, 30, 53–56] are some examples of studies on scaling strategies in railway–related test setups. The scaling rules in these works were based on reducing all geometrical dimensions by a scale factor  $N$ , whereas the scales on other parameters were calculated by relationships between different variables.

As described in [30], a scaling strategy needs to be selected based on the type of analysis work to be carried out on the rig. Some scaling strategies were classified and comparatively evaluated in [30]. These strategies were useful approaches for the studies on dynamics and stability of railway vehicle/ bogie. The wheel–track system in this research is going to be extensively used for contact mechanics studies. The contact problem involves high–frequency dynamics of the wheel–rail interaction and nonlinearities in materials. The scaling strategy of the current research is shown in Table 3.3, by addressing the required scale factors on different variables.

Table 3.3. Scaling strategy of the new test rig, scale factor on different variables

Variable/ parameter	Variable notation	Units	Scale factor notation	Scale factor
Length	$L$	$m$	$\phi_L$	$N$
Cross section	$A$	$m^2$	$\phi_A$	$N^2$
Volume	$V$	$m^3$	$\phi_{Vol}$	$N^3$
Inertia	$I$	$m^4$	$\phi_I$	$N^4$
Density	$\rho$	$kg/m^3$	$\phi_\rho$	$1$
Mass	$M$	$kg$	$\phi_M$	$N^3$
Young's modulus	$E$	$N/m^2$	$\phi_E$	$1$
Poisson's ratio	$\nu$	<i>None</i>	$\phi_\nu$	$1$
Force	$F$	$N$	$\phi_F$	$N^2$
Creep/tangent force	$T$	$N$	$\phi_T$	$N^2$
Stress	$\sigma$	$N/m^2$	$\phi_\sigma$	$1$
Strain	$\varepsilon$	<i>None</i>	$\phi_\varepsilon$	$1$
Stiffness	$K$	$N/m$	$\phi_K$	$N$
Damping	$C$	$N.s/m$	$\phi_C$	$N^2$
Frequency	$f$	$Hz$	$\phi_f$	$1/N$
Time	$t$	$s$	$\phi_t$	$N$
Velocity	$v$	$m/s$	$\phi_v$	$1$
Acceleration	$a$	$m/s^2$	$\phi_a$	$1/N$
Friction coefficient	$\mu$	<i>None</i>	$\phi_\mu$	$1$

The value  $N$  in Table 3.3 stands for the overall scale of the test rig, while different scale factors on each parameter are shown with  $\phi$  factors. Considering  $\phi_L = N$  on spatial dimensions, the other scale factors are obtained for the other parameters in Table 3.3, e.g. for acceleration  $\phi_a = \phi_L / \phi_t^2 = 1/N$ . The scale factor on time can be interpreted by the scaled duration of the experiment needed for running on a configuration with the scaled dimensions. It can also be interpreted by the increased number of contact cycles (by a factor of  $N$ ) that a downscale wheel can create when running on the track. A similar time scaling is also used by the INRETS test rig in the literature [30].

The chosen strategy provides the following advantages: 1) the scale factor on any parameter is obtained by keeping the quantities of material specification (e.g. density  $\rho$ , Young's modulus  $E$  and Poisson's ratio  $\nu$ ) unchanged. It is important that the nature of fatigue and fracture in the test rig components (more importantly in wheels and rails) be the same as the real life system. This can be achieved when material properties are the same as reality. 2) This scaling strategy keeps the stress and strain in materials the same as reality. This is again important due to the tendency for having the same fatigue and fracture mechanisms in the wheel-track system. 3) The chosen scaling strategy does not consider any scale factor on the friction and traction coefficients. Thus, the tribological behaviours of the wheel-rail system are kept similar to reality. This is of significant importance as some RCF defects (e.g. wheel flat) occur due to tractive/braking efforts. The scaling strategy of this research has also been successfully experimented in [29, 53].

In order to simulate and design the test rig in this research the scale factor of 1:5 was tentatively selected for the three alternatives. The dimensions of the wheel and rail were determined, by scaling the actual geometries (wheel profile S1002 and rail profile UIC54E1) down to the scale of five. The material parameters for the modelling purpose are listed in Table 3.4. The diameter of the rail ring in all the three alternatives was tentatively set to 4 m. It is noteworthy that the proposed parameters and geometries are the nominal data obtained based on the scaling law. These parameters are used for the comparing the alternatives and for the concept design. It should be noted that these quantities need to be practically refined in the engineering design process for the ease and feasibility of manufacturing.

Table 3.4. Values of parameters used for wheel–rail materials in numerical simulations

Parameter	Value in actual railway	Scale factor	Design values in the test rig
Young's modulus of material, $E$	210 GP	1	210 GP
Poisson's ratio of material, $\nu$	0.3	1	0.3
Density of material, $\rho$	7800 kg/m <sup>3</sup>	1	7800 kg/m <sup>3</sup>
Lumped sprung mass, $M_c$	13.4 t	$N^2=25$	536 kg
Wheel diameter, $\phi$	920 mm	$N=5$	184 mm
Wheel mass, $M_w$	900 kg	$N^3=125$	7.2 kg
Friction coefficient, $\mu$	0.5	1	0.5
Stiffness of primary suspension, $K$	1150 kN/m	$N=5$	230 kN/m
Damping of primary suspension, $C$	2500 N s/m	$N^2=25$	100 N s/m
Rail vertical moment of inertia, $I_{xx}$	2337900 mm <sup>4</sup>	$N^4=625$	37406 mm <sup>4</sup>
Rail bottom section modulus, $S_{bot}$	311181 mm <sup>3</sup>	$N^3=125$	2489 mm <sup>3</sup>
Rail top section modulus, $S_{top}$	278753 mm <sup>3</sup>	$N^3=125$	2230 mm <sup>3</sup>
Rail lateral moment of inertia, $I_{yy}$	4192000 mm <sup>4</sup>	$N^4=625$	6707 mm <sup>4</sup>

### 3.3.2 Numerical modelling of the wheel–rail contact in the new test rig

The wheel–rail contact problem in the test rig can be simulated using finite element (FE) modelling. The FE models of the three alternatives (test rig models) and the reference case (the actual wheel–rail system) are shown in Figure 3.4. The contact occurs in the lateral centre of the railhead against the wheel tread. The sprung mass, which together with the unsprung mass (the wheel) forms the wheel load, was lumped and supported by a group of springs and dampers of the primary suspension. The loading condition was considered identical for the three alternatives (536 kg sprung mass applied on the wheels). The contact surfaces of both the wheel and the rail were smooth.

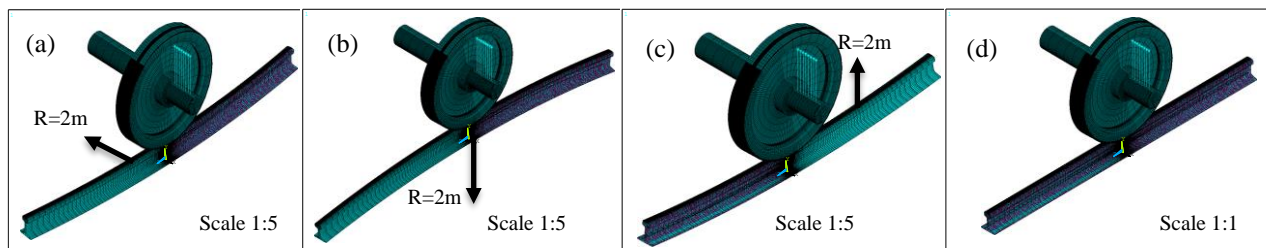


Figure 3.4. 3D FE models of the wheel–rail contact in different alternatives, (a) Alt–1, (b) Alt–2, (c) Alt–3 and the actual railway as the reference case (d); arrows with  $R=2m$  show directions of the rail curvature in different cases

Table 3.5. Results of normal contact problem by FE simulation for different alternatives

Parameters/Alternatives	Unit	Alt–1	Alt–2	Alt–3	Actual condition
Wheel radius	$R1(mm)$	92	92	92	460
	$R2(mm)$	$\infty$	$\infty$	$\infty$	$\infty$
Rail radius (ring/head)	$R1(mm)$	$\infty$	–2000	2000	$\infty$
	$R2(mm)$	70	70	70	300
Vertical Load	$N$	5360	5360	5360	134000
Semi–radius in FEM	$a(mm)$	1.3	1.29	1.31	6.03
	$b(mm)$	1.54	1.58	1.51	8
Contact area	$mm^2$	6.26	6.38	6.19	151.55
Max. pressure FEM	$MPa$	1284.4	1261.5	1300.1	1344
Max. pressure Hertz	$MPa$	1299.5	1278.3	1319.1	1364.7
Difference FEM/Hertz theory	%	1.18	1.33	1.46	1.54

As mentioned before, having stresses and strains close to the real system is one of the major requirements on the new test rig, so as to reproduce RCF of the same nature as in the



actual system. In order to estimate the level of contact stresses and strains, the solutions of the wheel–rail rolling contact problem were determined for the three alternatives. The modelling procedure with FEM and its validation against Hertz and Kalker solutions were previously reported in [42]. The results of FE simulations in this research are summarized in Table 3.5. The outputs of the simulations for the actual wheel–rail model (Figure 3.4(d)) were consistent with those of [42]. Furthermore, the maximum pressures of the wheel–rail contact problem were calculated using the Hertz theory for comparison. These results are given in Table 3.5 together with the differences between FEM and Hertz theory in each case. The last column of the table presents the results of the actual wheel–rail components as a reference.

As shown in table 3.5, the size of the contact patch was very much reduced by a factor of  $N^2$  ( $= 5^2$ ). The precise ratios of the contact area relative to the actual case were respectively 24.2, 23.8 and 24.5 for the given alternatives. The contact pressures were close to the actual case; the differences in the three alternatives were respectively 4.4%, 6.1% and 3.3% compared to the actual case. The differences in the contact area and stress are negligible. These are caused by the mesh discretization in the model and by the curvature of the rail ring in the vertical or lateral direction, depending on the alternatives. In summary, all three alternatives offered closely comparable results and no significant distinction can be made in this respect.

### 3.3.3 Numerical modelling of the rail bending in the new test rig

The downscale rail profile needs to be bent to create the curvature required for the various alternatives. This can be achieved by driving the rail through a suitable configuration of three steel rollers known as the roller–bending method [56, 57]. Residual stresses may arise during this process. The residual stresses were estimated by simulating the bending process with FEM. The FE models corresponding to the three alternatives are shown in Figure 3.5(a, b, c). The FE models provided in this section are static simulations to calculate the stresses that can be generated during the roller–bending process. The results of the equivalent von–Mises stress due to bending are presented in Figure 3.5(d, e, f). These stresses were generated during the rail bending to 4 m diameter.

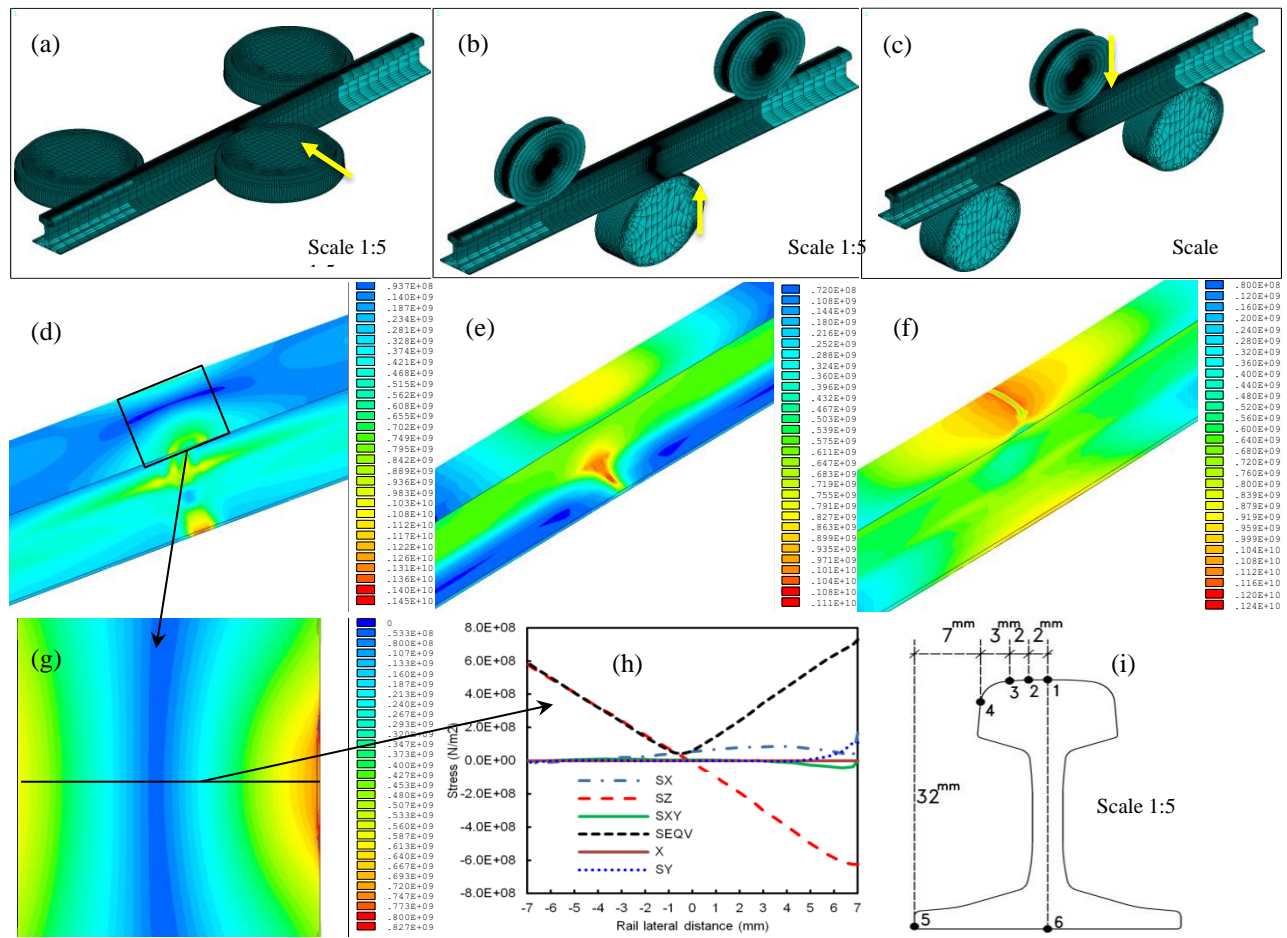


Figure 3.5. 3D FE models of the rail bending process for the three alternatives, (a) Alt-1; (b) Alt-2; (c) Alt-3; arrows show the directions of movement in rollers; (d, e, f) Von-Mises stress contour plots generated during the bending process in different FE models; (g) closer view of the rail surface stress in Alt-1; (h) variation of the stress components in the 2D lateral view; (i) 6 elements are selected in the rail cross section for reporting the stresses

The residual stresses will remain in the rail because the rail is permanently deformed with the prescribed curvatures. Since the rails are intended for RCF experiments, residual stresses can have an unwanted influence on the test results. It is desirable to have low residual stress in the railhead and particularly in the running band. To examine this in the different alternatives, the stresses were determined for the most critical or characteristic locations at six elements. Four elements were chosen in the railhead (see 1 to 4 in Figure 3.5(i)) and two extra elements in the middle and the edge of the railfoot (5, 6 in Figure 3.5(i)). A summary of the maximum von-Mises stresses at these elements is reported in Table 3.6 for all the three alternatives. Looking at Von-Mises stresses in Table 3.6, a significant difference is seen between the modelled alternatives. As can be seen there, significantly high stresses occurred in Alt-2 and 3 in the rail surface (elements 1–3). The peak stresses were seen in the middle of running band (element 1) for both alternatives. In contrary, Alt-1 had the least stress magnitude in this element (153 MPa), which is lower than the yield stress of a typical rail material. According to the results in elements 1–3, Alt-1 introduced the least stresses in the running band. The greatest stress for Alt-1 was seen at the edge of rail foot. This is of less importance as the focus in the test rig is to study the wheel–rail contact interface where RCF occurs. Nevertheless, adequate care is taken in the design process to ensure that the fatigue at the edge of the rail foot will not affect the testing. The numerical modelling of the rail bending process suggests an encouraging advantage for Alt-1, in which the railhead and especially the running band are less subjected to residual stresses. The numerical model of

this section does not consider the time-dependent stress relaxation in materials when the rail is released from the roller-bending machine. It assumes that the obtained residual stresses will remain in the rail; because the rail is permanently deformed. This is indeed a conservative assumption since in reality part of these stresses will be relieved by time.

Table 3.6. Summary of the maximum V–M stresses for the three alternatives (all stresses in MPa)

Element location	1	2	3	4	5	6
Alt–1, Figure 3.5(a)	153	242	354	965	1449	118
Alt–2, Figure 3.5(b)	823	817	796	589	508	1115
Alt–3, Figure 3.5(c)	1241	1169	1085	764	938	914

### 3.4 Summary of the comparisons and final choice for the test rig

So far, a numerical approach was used to evaluate the mechanical performance of the different alternatives. In addition to these factors, the alternatives can be further evaluated based on several qualitative criteria. An overview of these aspects is summarized here.

#### 3.4.1 Rail track stability

The importance of incorporating a track system with its detailed components into the test rig was shown before. A conventional railway track is composed of discrete components with no adhesion force between them, particularly with and between the ballast gravels which cannot sustain tensile stresses. A horizontal track system (Alt–1 of Figure 3.3) is thus more stable than Alt–2 and 3 as the ballasted railway track with its typical form will be preloaded by the gravity loads from the vehicle. This can provide the test rig with higher stabilities, more durable geometrical conditions, a higher level of safety and closer similarity to the actual railway track.

#### 3.4.2 Analogy of loading conditions to the actual railway

For the scaled alternatives, the wheel needs to be preloaded on the rail to achieve the required normal load. In most test rigs with the configuration of Alt–2 or Alt–3, the wheel remains static under the applied load and the rail (or the track) rotates under it. Such loading mechanism and that of the real life are somewhat unequal, particularly in connection with the vibrations that are generated in the vehicle and track subsystems. Such loading mechanism can be suitable for quasi-static analysis of the wheel–rail contact problem, while the loading mechanism of Alt–1 better represents the dynamic nature of the system. Another operational mechanism for Alt–2, 3 is the case where the wheel rotates around the vertical track drum. In this case, the direction of the normal load constantly changes during the wheel rolling in Alt–2, 3. Hence, the control of the wheel preload in Alt–2, 3 is apparently more complicated. Furthermore, the wheel–rail contact pressure in Alt–2 and 3 changes when the wheel is running. In contrary, when the wheels continuously roll over rails in an actual railway (also the case of Alt–1), a constant normal force is present between the wheel and rail, if the dynamics of the wheel–track system is ignored. For Alt–1, that utilizes a horizontal track bed, the normal load is applied only in a single direction (the gravity direction) and this direction remains constant during the operation.

A similar discussion applies to the longitudinal loading (traction/braking efforts). Taking all these factors into account, important operational benefits can be seen for Alt–1.

### 3.4.3 Final choice for the test rig

In view of the above discussion, the first alternative (a rotating wheel on a horizontal track bed) offers more benefits and shows a better potential performance than the other two. A summary of its advantages is listed in Table 3.7. Based on this evaluation, the operational mechanism of the first alternative is chosen for the new test rig.

Table 3.7. Summary of comparison of the three alternatives

Criteria	Comparison of the three alternatives
Contact stresses and contact patch size	A slight difference was observed. No strong prioritisation can be proposed.
Residual stress levels in the railhead	A clear distinction was found. Alt-1 offers a substantial benefit of significantly lower residual stresses in the railhead and the running band due to rail bending.
Rail track stability, analogy in loading conditions	Alt-1 offers significant advantages in rail track stability and analogy of loading conditions to the actual system owing to its horizontal track bed configuration.

According to the chosen mechanism, detailed numerical modelling and mechanical calculations were carried out to finalise the structural design of the new setup. The test rig has been engineered with an overall scale of 1:5 (basic scale), providing the flexibility of having smaller or bigger wheel–track elements. The CAD view of the setup after the engineering work is shown in Figure 3.6, with the nomination of the major components underneath the figure. It is capable of testing materials of rails and wheels under loading conditions equivalent to the actual operations. As can be seen in Figure 3.6, the rig is a rotating frame structure with four wheels running on a fixed rail track bed, capable of simulating continuous wheel–rail contact.

The setup is constructed through a rigorous engineering design and manufacturing process, involving the professional expertise of various fields in mechanics, mechatronics, electronics, control, safety, etc. Analogical components of the wheel–track system are made and assembled, maintaining dynamic behaviours of the tests with similarity to real vehicle–track systems including the scalability analysis described in this chapter. Figure 3.7 shows the newly–built setup, established on a firm fundament in the laboratory. The track bed in Figure 3.7 consists of a scaled rail connected to the wooden sleepers using elastic fasteners. The ballast in the current configuration is replaced by rubber materials with the required damping/stiffness properties. It can also be made of crushed stone as enough space is provided by the track container to hold the ballast and allow for tamping. The wooden sleepers can also be replaced by concrete sleepers depends on the test goals. The rail is supported by the sleepers in lateral, longitudinal and vertical directions. The sleepers can be constrained in any combinations of the three directions by connecting them to the track container with the desired stiffness and damping.

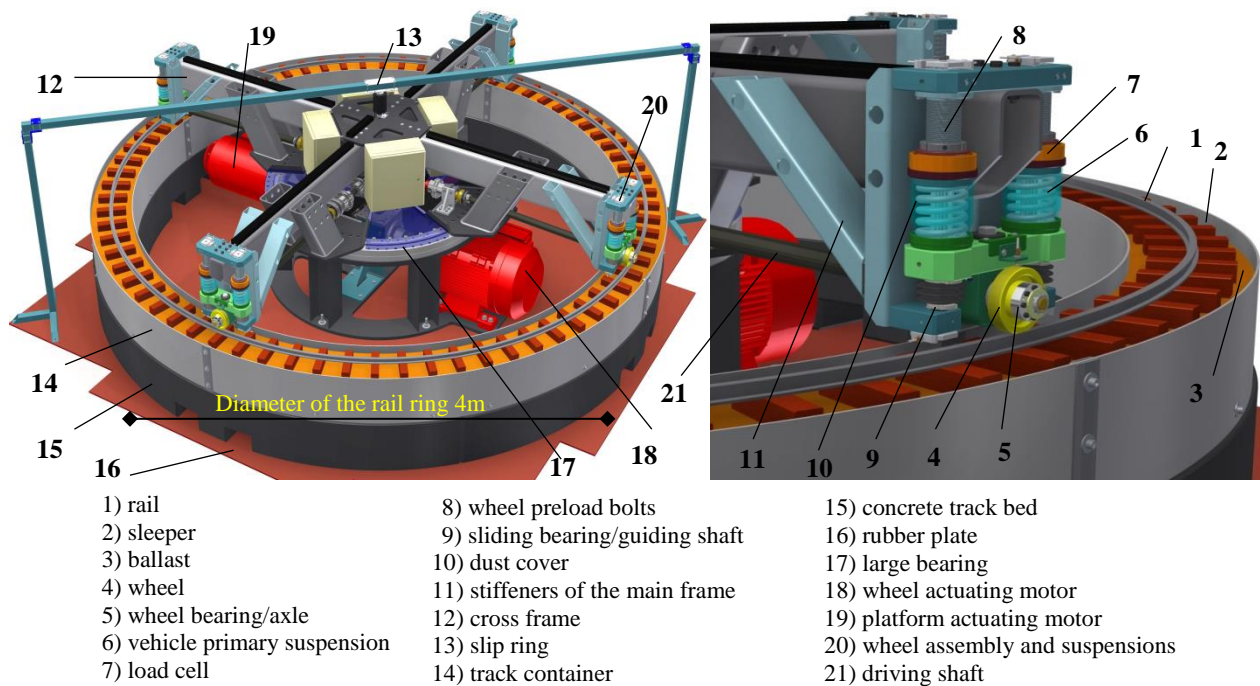


Figure 3.6. The CAD view of the final test rig after detailed engineering design

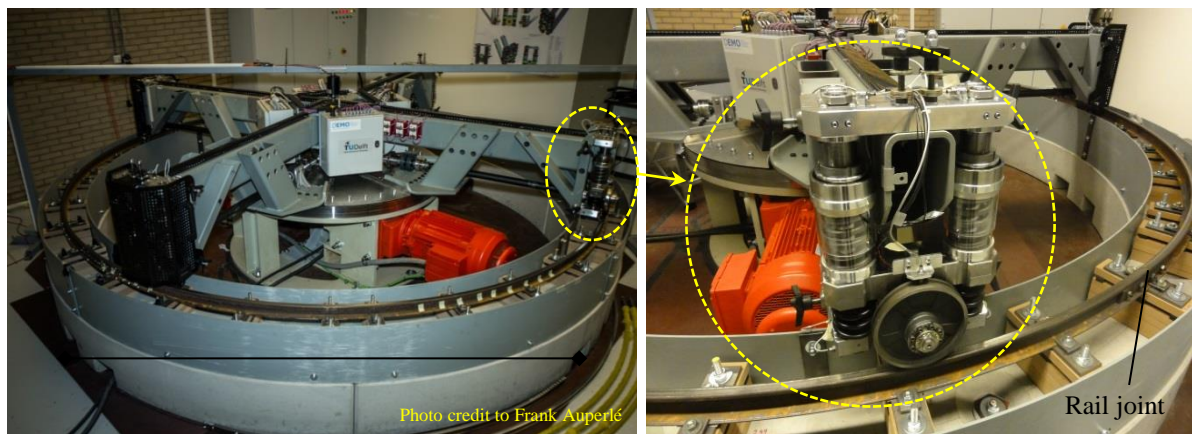


Figure 3.7. The newly-built test rig for the wheel-rail contact studies; each of the four wheel-assemblies can be activated or dismantled from the frame

Having a curved track in the setup is the most important dissimilarity factor between the setup and the real life. However as stated in Section 3.2.4, this is the most effective way that provides a continuous long-term rolling contact between the wheel and rail. Due to the same reason, the majority of the existing test rigs in the literature have used the curved track principle. In order to minimize the effect of having a curved track in the test configuration the following treatments can be provided in the setup:

- For testing squats (involving the vertical high-frequency vibrations) the wheels do not necessarily have the flange and the contact occurs in the middle of the railhead. Therefore, gauge corner contact will be avoided. Any effects of the curved setup on the similarity with the straight track will be studied, identified and removed for any specific tests. Numerical analysis and physical testing can be used for this purpose; possible approaches are briefly demonstrated in the following. For testing head-checks, flanged or conical wheels can be used, where gauge corner contact can occur.

- By offsetting the centre of the rail ring, the position of the running band of the wheels will vary with the offset along the ring. Further the setup benefits from four multiple wheels with adjustable positioning on the rail surface. The four wheels can create different running bands on the railhead, which can prevent the contact to happen only in a certain band.
- To avoid conformal contact, the wheels will be re-profiled or changed after certain contact cycles if they are highly worn.
- The rail circle diameter has been selected relatively large (4m) to have sufficiently low residual stresses during the rail bending.

From the engineering point of view, a diameter larger than 4m was not feasible because the moving subsystem (wheels, driving shafts, frames and all their attached components) will exert extremely high electro–mechanical demands on safety and on the strength of some components. The following explanation about the curved track mechanism is important from the loading prospective:

In the new test rig, the wheels are constrained in the lateral directions by connecting them rigidly to the frame structure with constant angle of attack. Using such a mechanism, the dynamic behaviour of the wheels in the longitudinal-vertical direction is comparable with the real system, while providing controlled lateral loading.

By setting the angle of attack at different (fixed) values, different lateral contact force can be produced. Loading due to spin by kinetic yawing is not possible; this can be compensated by defining the geometrical spin via, e.g., profiles of constant wheel conicity or via scaled real-life profiles of wheel and rail. With this configuration, a realistic wheel-rail contact loading i.e. the vertical force and tangential forces by longitudinal, lateral and spin creepages, can be generated for situations in straight and curved tracks. Such a controlled and repeatable lateral contact force, as well as the controlled and repeatable vertical and longitudinal contact forces, are the advantage of controlled laboratory tests.

The following explanation about the repeatability of the test outputs is important:

All the 4 wheels are controlled centrally by the two motors and they have the same radius. Thus, nominally, all the wheels have the same slip. On the other hand, the “track” can vary along the ring in terms of geometry, materials, construction, stiffness and damping, making variations in contact forces, slip, wear, deformation and RCF possible. This situation is comparable with the real systems. The tests performed, so far, have shown that the measurements of the contact forces that vary along the ring are repeatable. These make it possible to perform simultaneous tests of different loading, geometry, construction and materials under controlled and repeatable conditions.

#### 3.4.4 Description of the new test rig

As can be seen in Figures 3.6 and 3.7, the four wheel assemblies are mounted on a stiff frame (the platform). This platform is fixed to the inner ring of a large bearing (17 in Figure 3.6) and drives by the platform motor (19 in Figure 3.6). The outer ring of this bearing is fixed using a frame to the ground. The wheels are driven by the wheel motor (18 in Figure 3.6). This motor is coupled with two gearboxes that transfer and divide the power to the wheels.

The combination of these two motors (18 and 19) generates traction or braking forces at the wheel rail contact and maintains the required speed. The power from the wheel motor is transferred with a gearbox from rotation around the horizontal axis to a rotation around the vertical axis. With a second gearbox, the rotation around the vertical axis is transferred with a factor of 1/4 to the rotation around the horizontal axis on each wheel shaft. The power from the platform motor is used to drive an internal gear that is mounted on the large bearing. When the wheel motor is driving, one can use platform motor to let the wheels slip relative to the rail. When the platform motor is driving, one can use the wheel motor for braking the

wheels. With such mechanism, the driving and braking possibilities can be provided for the wheels under the desired creepage with the traction coefficient variable between 0 and 0.45.

The wheels are mounted on the rail using the spring–damper assemblies (20) with adjustable loading mechanism equivalent to the primary suspension of a train. The vertical static preload on the wheels is adjusted by preloading the two springs (6) between the wheel axle (5) and the cross–frame above it (12). The wheels can be cylindrical or conical depending on the test requirements. The wheel angle of attack is adjustable between  $-2^\circ$  and  $+2^\circ$ .

Depending on the scope of each testing scenario, one would be able to study various degradation topics: 1) about the rail e.g. wear, squat, head–check, weld effect, joint effect; 2) about the wheel e.g. wheel flat, unrounded wheel; and 3) about the other track components, e.g. loose or damaged fasteners, worn railpads, unsupported sleepers, polluted ballast etc.

### 3.5 FE modelling and experiments using the newly–built test rig

This section presents some results on estimating and measuring the high–frequency vibrations in the newly–built test rig. For this purpose, some output of FE modelling and real measurements with the newly–built setup is provided. A transient–finite element model of the wheel–track contact was built according to the geometry and loading conditions of the 1:5–scaled setup; see Figure 3.8 (a). The FE calculations provided in this section are dynamic simulations to compare the numerical results with the experimental results; in these FE models, a wheel component runs with the given speed over the track. The material specifications and loading parameters were assumed according to Table 3.4. As given in Table 3.5, the contact stresses and the patch size are only slightly different for the curved rail. Hence, a straight rail track is modelled. The parameters of the sleepers, fastenings and ballast in the FE model were calculated by the scaling factors in Table 3.3. For the purpose of comparison, a finite element model of the actual wheel–track system (full–scale) was also built; see Figure 3.8 (b).

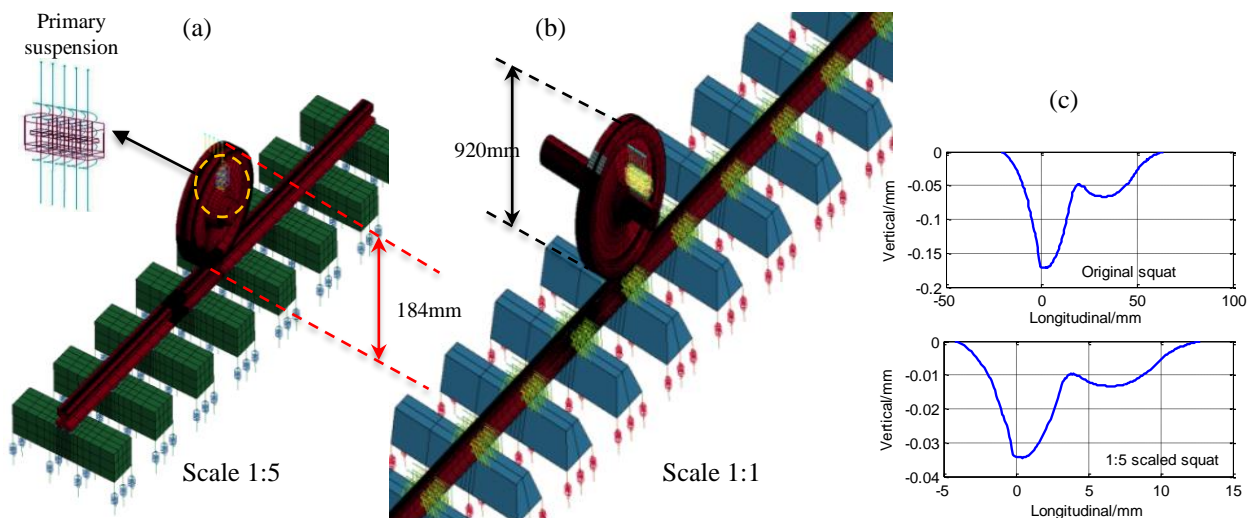


Figure 3.8. (a) A FE model of the 1:5–scaled test rig to study its dynamic behaviours; (b) the FE model of the actual wheel–track system, the wheel diameters (184 and 920 mm) are shown as per indication of the scale; (c) the geometry of an original real–life squat and its equivalent defect with the scale of 1:5

#### 3.5.1 FE modelling with squat defect

A typical squat with W–shape profile [58] was applied on the rail surface of the full–size model. Applying the linear scale factor of 1:5 on the defect geometry, an equivalent defect

was applied on the 1:5–scaled model. Figure 3.8 (c) shows the longitudinal–vertical profiles of the original and the scaled squats.

Considering these defects, dynamic simulations were carried out for the 1:1 and 1:5 models. The time history of the wheel–rail contact forces for the smooth rails and for the rails with the prescribed squats are shown in Figure 3.9. The abscissas in these figures are normalized relative to the maximum simulation times in each model to obtain comparable data. The vertical axes show the dynamic load ratios relative to the corresponding static values (dynamic amplification factors).

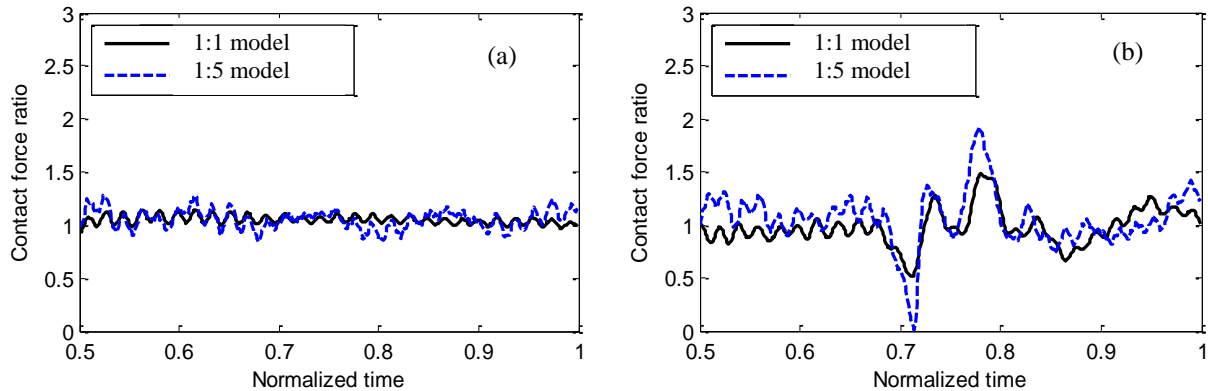


Figure 3.9. The normalized wheel–rail contact forces in the FE models with (a) smooth rail; (b) squat defect

As can be seen in Figure 3.9, the dynamic amplification factors under the presence of squats were increased in both the full–scale and scaled models. This means that the dynamic behaviour of the wheel–track system due to the impact loading condition, caused by squats, were properly reproduced in both models.

### 3.5.2 FE modelling and experiments of the rail joint

To study the dynamic behaviour of the scaled test rig in the presence of the impact–induced RCF, a typical insulated rail joint in the Dutch railway system was considered. A similar rail joint (with the scaled size) was constructed in the newly–built test rig; Figure 3.7 (b). To compare the dynamic behaviour of the rig with the actual system, trial tests were performed with the running speed of 20 km/h, wheel diameter of 200 mm, the standard rail profile of S7 and the static load of 1.3 kN on the wheel. The wheel–track components were made for the preliminary tests and were not precisely according to the required scale factors. The components in such a preliminary wheel–track setup were downsized with various scales between 1:3 and 1:5 relative to the real system.

Using a transient finite element approach [42], the rolling contact process of the wheel over the rail is simulated for the two cases, i.e. the actual railway and the downscale test rig, shown in Figure 3.8 (a, b). To consider the effect of rail joint, a 10 mm rail gap was considered in the finite element model of the full–scale rail, similarly, a 2 mm rail gap in the test rig rail.

The time histories of the wheel–rail contact force are given in Figure 3.10, for the smooth rail and for the rail with the joint. For the sake of comparison, the abscissas in these figures were normalized relative to the whole duration of the simulation or the measurement. The vertical axes show the dynamic load ratios relative to the corresponding static loads. The contact force between the wheel and rail are measured using a real–time data acquisition system in the test rig.



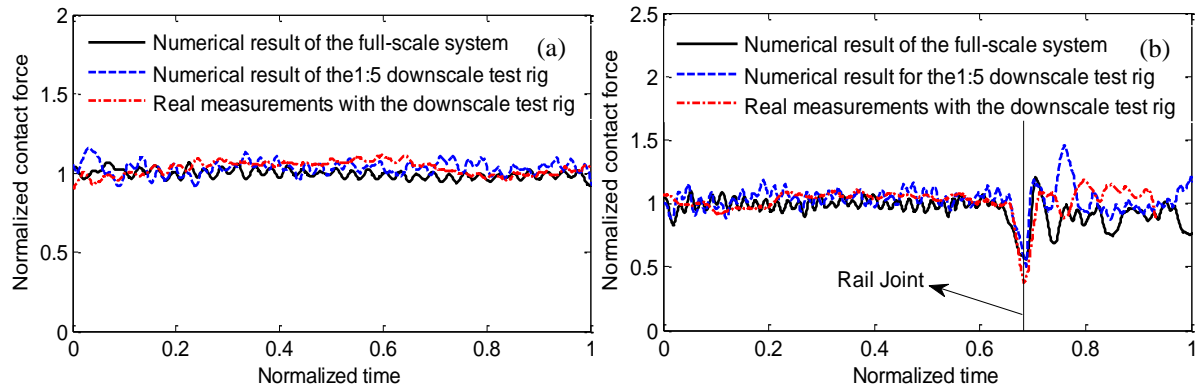


Figure 3.10. The normalized contact forces, (a) smooth rail; (b) with rail joint; comparison between the test rig model (scale 1:5) and real measurements in the test rig with preliminary wheel–track components of various scales between 1:3 and 1:5

It can be seen from Figure 3.10 that the contact force obtained from the modelling is in good agreement with the measured forces in the test rig with or without the presence of the rail joint. The frequency content of the normal contact force is calculated using Fast Fourier transformation (FFT); see Figure 3.11. The major high–frequency content is around 1.1 kHz, which agrees with the high–frequency range obtained for the real track [59], where measurements of similar cases were presented. These findings confirm that the setup is able to represent high–frequency dynamic characteristics of the wheel–rail contact similar to the actual system.

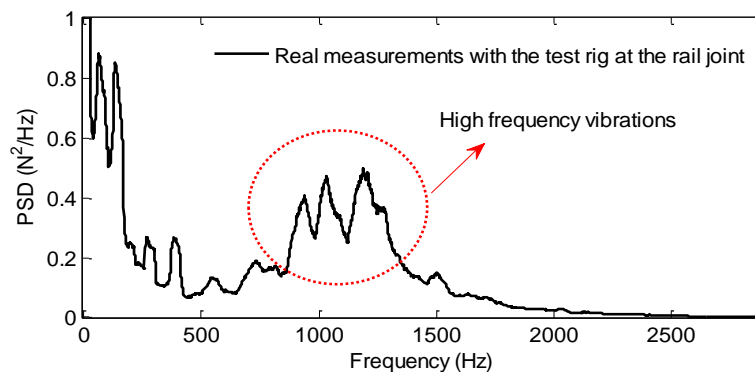


Figure 3.11. The frequency content of the contact force measured in the test rig with rail joint

In order to further evaluate the dynamic performance of the test rig, the setup has been under operation using the trial wheel–rail pairs (wheel diameter 200 mm and the standard rail profile S7). The speed varied between 0 and 40 km/h and the static preload on the four wheels was around 1.3 kN. The running bands on the rail and wheels were frequently inspected during the test intervals. After around 41300 revolutions (in total 165200 wheel–rail contact cycles, as four wheels were activated) some changes were observed on the rail surface. A potential rail corrugation, shown in Figure 3.12 (b), started to develop after the rail joint. Figure 3.12 (a) shows an example of corrugation wave pattern that occurred close to a real joint in a straight track in the Dutch railway network. Looking at the wave pattern of the potential corrugation in Figure 3.12 (b) and its proximity to the rail joint, the similarity with the real–life corrugation (Figure 3.12 (a)) is remarkable. Such a wave pattern was only seen after the rail joint, hence it can be hypothesised that it is generated due to the dynamic impact induced by the rail joint; see the impact in Figure 3.10(b). RCF defects can be the consequence of corrugations due to the high loads occurred at corrugation [60]. RCF can also be a cause of corrugation as it was suggested by [61, 62]. The damage mechanism for many RCF and corrugation defects is the high–frequency vibration of the wheel–track system,

which can be studied using the new test rig. These observations further confirm that the new test rig is able to generate the impact–induced defects in rails, as it was predicted in the design process.

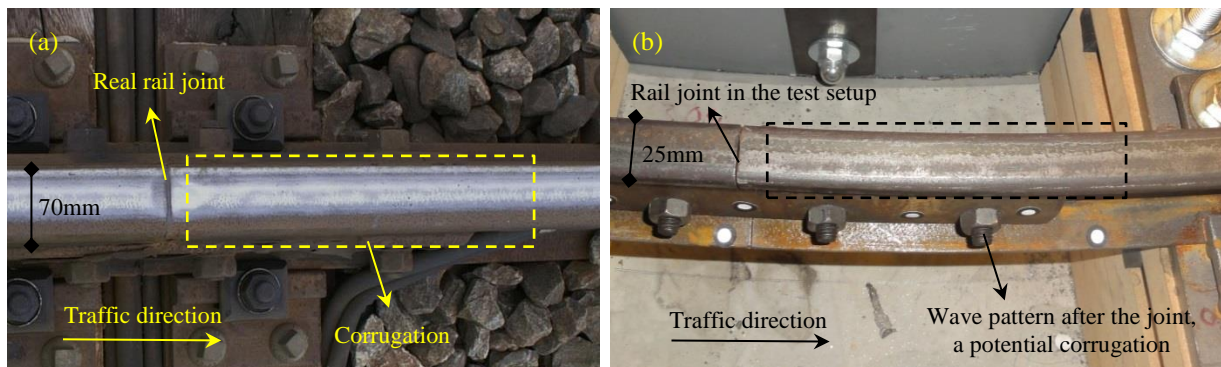


Figure 3.12. (a) An actual corrugation after the rail joint in the Dutch railway network; (b) a potential corrugation after the rail joint in the new test rig with preliminary wheel–track components of various scales between 1:3 and 1:5

It is essential to also look at the magnitude of potential defects with respect to the microstructure level. In [63], it is shown that typical microstructures of the real-life defects have a dimension of about 20  $\mu\text{m}$  or less. The semi-axes of the contact area in the test rig are 1.3 – 1.5 mm (Table 3.5). Thus, the real-life microstructures are much smaller than the test rig contact area. The expectation is thus that the test rig should be able to generate RCF defects of microstructures comparable to those of real-life RCF.

### 3.5.3 Scalability of track dynamic characteristics by impact measurements

In order to investigate the scaling effect on the dynamic behaviour of the track system, a prototype ballasted railway track is built in the lab with the scale of 1:5 (Figure 3.13). The components of the scaled track system were designed and made with the specifications given in Table 3.8. Dynamic hammer test measurements were carried out on the scaled test track. Dynamic excitations were generated using a 160 gr instrumented impact hammer. The hammer hits the rail surface at different locations relative to the sleepers, i.e. on top of the sleepers (on support) and at the middle spans; see Figure 3.13(b). Two accelerometers were mounted on the railhead (one on support and another one on the midspan) to record the dynamic responses in the track induced by the impact hammer.

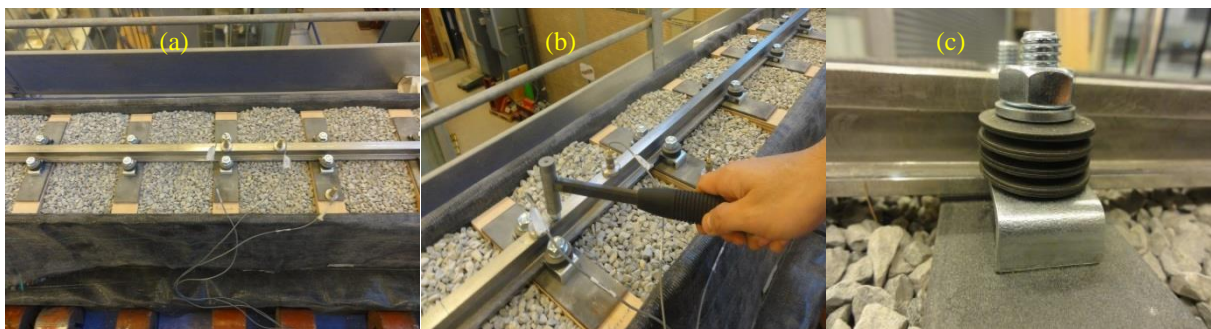


Figure 3.13. (a) A 1:5 downscale ballasted railways track; (b) hitting the rail surface using an instrumented impact hammer; (c) magnified view of the designed fastening system for fixing the rail on sleepers

Table 3.8. Specifications of the track components used in the 1:5 downscale ballasted railways track

Track component	Specifications
Rail	<ul style="list-style-type: none"> <li>- A 1:5 scaled profile based on the standard UIC54E1 profile</li> <li>- Height 30mm, railhead depth 8mm, railhead top curve radius 60mm, railhead width 18mm, railfoot width 28mm</li> <li>- Weight: 2.95 kg/m</li> <li>- Cross section: 378 mm<sup>2</sup></li> <li>- Moment of inertia <math>I_{xx}</math>: 3970 mm<sup>4</sup></li> <li>- Bending stiffness: 8337 Nm<sup>2</sup></li> </ul>
Sleepers	<ul style="list-style-type: none"> <li>- A 1:5 scaled profile based on the standard B93.1 sleeper</li> <li>- Material: a mix of wood and steel with the scaled weight</li> <li>- Dimensions: length 250mm, width 50mm and height 40mm</li> <li>- Sleeper weight: 1250gr</li> <li>- Sleeper spacing: 120mm (centre to centre)</li> </ul>
Fastening system	<ul style="list-style-type: none"> <li>- Materials: combination of steel bolts, spring washers, clips, bolts and washers</li> <li>- Weight of the fasteners per sleeper <math>\approx</math> 250gr</li> <li>- Spring washers: 6 per bolt in series</li> </ul>
Railpads	<ul style="list-style-type: none"> <li>- Materials: Natural rubber</li> <li>- Size: length 50mm, width 28–30mm and height 1–3mm; (height is adjusted to reach the required stiffness)</li> <li>- Stiffness of rail pad <math>\approx</math> 50 kN/m</li> <li>- Damping of rail pad <math>\approx</math> 2 kN.s/m</li> </ul>
Ballast	<ul style="list-style-type: none"> <li>- Materials: granite stone gravels</li> <li>- Density of the compacted ballast <math>\approx</math> 1551 kg/m<sup>3</sup></li> <li>- Size of gravels: ranging from 4mm to 21mm</li> <li>- Stiffness of ballast <math>\approx</math> 10 kN/m</li> <li>- Damping of ballast <math>\approx</math> 1 kN.s/m</li> </ul>

Hammer test measurements were carried out with hitting the railhead vertically at locations above the sleepers and at midspans. The track accelerance (acceleration for a unit force) is calculated during the impact excitations. The acceleration responses are measured at supports and at the midspans. The results of frequency response functions (FRFs) are shown in Figure 3.14. This figure shows the characteristic frequencies of the track system under the mentioned impact loading. According to this figure, the pinned–pinned resonance frequency of the rail is around 4720 Hz, which is marked using a thick vertical dash line. This frequency corresponds to the location where a local peak is found at mid–span FRF and a sharp dip is seen on FRF above the sleeper. This pin–pin frequency is approximately five times of the corresponding pin–pin frequency of the full–scale track reported in [64]. Due to the use of a scale factor of 5, the track characteristic frequencies were approximately five times of those of the full–scale system; see the scale factor of the frequency parameter in Table 3.3. These results are in good agreement with results from another 1:5 scaled test track in [27] and further confirm the scalability potential of the developed downscale system with respect to dynamic characteristics.

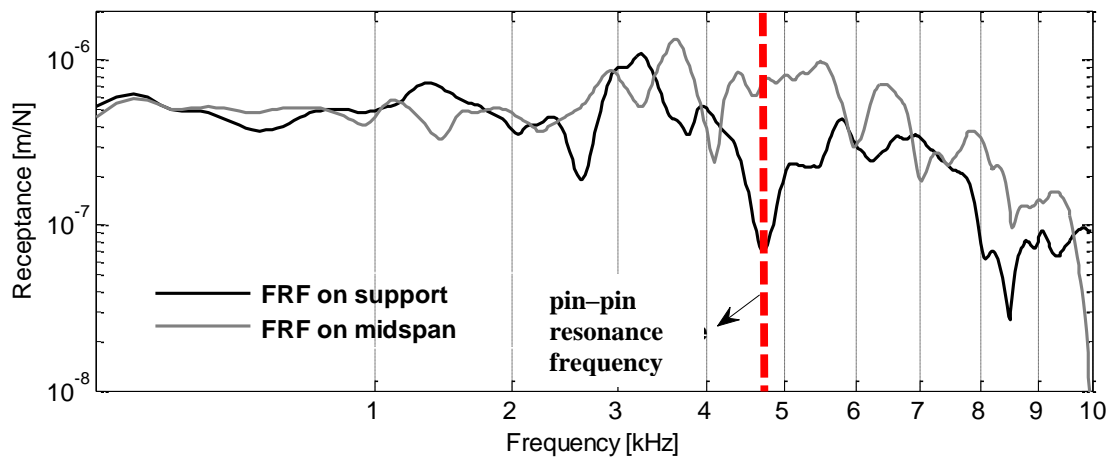


Figure 3.14. Results of impact hammer measurements in the 1:5 downscale ballasted railways track

### 3.6 Conclusions

A wide range of available test setups for wheel–rail contact experiments was classified and comparatively reviewed. Six categories were distinguished and their functionalities synthesised: 1) Full–size vehicle/ bogie, 2) Full–size wheel–on–roller, 3) Full–size wheel–on–straight, 4) Twin–discs, 5) Scaled wheel on rail track ring and 6) Scaled wheel on the straight track. The fifth category could better mimic the high–frequency dynamic behaviours of the system. Three conceptual alternatives were further analysed: Alt. 1) The wheel on a horizontal ring–track, Alt. 2) The wheel rolling on the outer side of a vertical track drum and Alt. 3) Rotating wheel on the inner side of a vertical track drum. According to the results, the following conclusions are drawn:

- 1- The rail curvature ( $R=2\text{m}$ ) in the different alternatives had negligible influence on the contact stresses and contact patch size.
- 2- Numerical simulations confirmed that Alt–1 in which the rail profile is bent about its vertical axis has significantly lower residual stresses (due to rail bending) in the running band of the railhead.
- 3- Alt–1 also offered significant advantages with respect to the rail track stability and analogy of loading conditions to the actual system.
- 4- Using transient finite element modelling, it was confirmed that the new test rig is capable of reproducing high–frequency dynamic characteristics of the wheel–track system when a typical w–shape squat is present on the railhead.
- 5- Dynamic effects induced by the presence of a rail joint were properly reflected in both the full–scale system and the downscale test rig. This was confirmed by transient finite element modelling and by real measurements using the newly built setup.
- 6- After about 41300 preliminary test revolutions in the new test rig, some potential corrugation wave patterns were observed on the railhead, which considered to be generated by the impact due to the rail joint. The wave pattern of this was in good agreement with those of the real–life systems.
- 7- The scalability of dynamic characteristics of the system is confirmed by performing impact hammer test measurement on a prototype ballasted railway track with the scale of 1:5.

The new setup is, in fact, a rotating frame structure containing four wheels, running on a fixed ring–track bed, capable of simulating the continuous wheel–rail rolling interaction. It is designed and manufactured with the overall scale of 1:5 (basic scale), providing the flexibility of having smaller or bigger wheel–track elements. It is built through a rigorous engineering design and manufacturing process. This test rig will provide a worthy means for deeper

insights into track degradation mechanisms and performance of rail and wheel materials under the impact loading comparable to real-life railway operation.

### 3.7 References

- [1] A. Ekberg, H. Bjarnehed & R. Lundb an, A fatigue life model for general rolling contact with application to wheel/rail damage, *Fatigue & fracture of engineering materials & structures*, 18 (1995) 1189–1199.
- [2] P. Clayton, D.N. Hill, Rolling contact fatigue of a rail steel, *Wear*, 117 (1987) 319–334.
- [3] S. Grassie & J. Kalousek, Rolling contact fatigue of rails: characteristics, causes and treatments, in: *Proceedings of 6th International Heavy Haul Conference*, The International Heavy Haul Association, Cape Town, South Africa, 1997, 381–404.
- [4] Z. Li, R. Dollevoet, M. Molodova & X. Zhao, Squat growth—Some observations and the validation of numerical predictions, *Wear*, 271 (2011) 148–157.
- [5] F. Franklin, G.–J. Weeda, A. Kapoor & E. Hiensch, Rolling contact fatigue and wear behaviour of the infrastar two–material rail, *Wear*, 258 (2005) 1048–1054.
- [6] ASTM–STP771, Rolling contact fatigue testing of bearing steels, in, *American Society for Testing and Materials*, 1982.
- [7] D.J. Thompson, A.D. Monk–Steel, C.J.C. Jones, P.D. Allen, S.S. Hsu & S.D. Iwnicki, Railway noise: curve squeal, roughness growth, friction and wear, *Real Research UK*, Report: RRUk A, 3 (2003).
- [8] S. Ma, W. Zhang, G. Chen & J. Zeng, Full Scale roller rig simulation for railway vehicles, *Vehicle System Dynamics*, 23 (1994) 346–357.
- [9] X. Alzaga, Manufacturing development, automatic machining and verification of railway running gears, in: *Second European Forum on Railway Running Gears*, Madrid– Spain, 2014.
- [10] A. Matsumoto, Y. Sato, H. Ohno, M. Tomeoka, K. Matsumoto, J. Kurihara, T. Ogino, M. Tanimoto, Y. Kishimoto & Y. Sato, A new measuring method of wheel–rail contact forces and related considerations, *Wear*, 265 (2008) 1518–1525.
- [11] M.C. Burstow, Rolling contact fatigue laboratory testing, File reference LD44089, Report number AEATR–ES–2004–907, Issue1, in, *RSSB (Rail Safety & Standards Board)*, 2006.
- [12] R. Stock & R. Pippan, RCF and wear in theory and practice–The influence of rail grade on wear and RCF, *Wear*, 271 (2011) 125–133.
- [13] Deutsche–Bahn–AG & Welte Druck GmbH, The Roller Rig, Munich–Freimann, Central Division for Research and Testing Research and Test Centre, Germany (1994).
- [14] S. Bruni, F. Cheli & F. Resta, A model of an actively controlled roller rig for tests on full–size railway wheelsets, *Proceedings of the Institution of Mechanical Engineers, Part F: Journal of Rail and Rapid Transit*, 215 (2001) 277–288.
- [15] K. Knani, S. Bruni, S. Cervello & G. Ferrarotti, Development of an integrated design methodology for a new generation of high performance rail wheelset, in: *World Congress of Railway Research WCRR*.
- [16] W. Zhang, H. Dai, Z. Shen & J. Zeng, Chapter 14, Roller Rigs, in *Handbook of railway vehicle dynamics*, in: S. Iwnicki (Ed.), CRC Press, Boca Raton FL (USA), 2006.
- [17] B. Allotta, R. Conti, E. Meli, L. Pugi & A. Ridolfi, Development of a HIL railway roller rig model for the traction and braking testing activities under degraded adhesion conditions, *International Journal of Non–Linear Mechanics*, 57 (2013) 50–64.
- [18] A.D. Monk–Steel, D.J. Thompson, F.G. de Beer & M.H.A. Janssens, An investigation into the influence of longitudinal creepage on railway squeal noise due to lateral creepage, *J Sound Vib*, 293 (2006) 766–776.

- [19] F. De Beer, M. Janssens & P. Kooijman, Squeal noise of rail–bound vehicles influenced by lateral contact position, *J Sound Vib*, 267 (2003) 497–507.
- [20] Q. Liu, B. Zhang & Z. Zhou, An experimental study of rail corrugation, *Wear*, 255 (2003) 1121–1126.
- [21] P. Allen & S.D. Iwnicki, The critical speed of a railway vehicle on a roller rig, *Proceedings of the Institution of Mechanical Engineers, Part F: Journal of Rail and Rapid Transit*, 215 (2001) 55–64.
- [22] S.S. Hsu, Z. Huang, S.D. Iwnicki, D.J. Thompson, C.J. Jones, G. Xie & P. Allen, Experimental and theoretical investigation of railway wheel squeal, *Proceedings of the Institution of Mechanical Engineers, Part F: Journal of Rail and Rapid Transit*, 221 (2007) 59–73.
- [23] T. Vuong, P. Meehan, D. Eadie, K. Oldknow, D. Elvidge, P. Bellette & W. Daniel, Investigation of a transitional wear model for wear and wear–type rail corrugation prediction, *Wear*, 271 (2011) 287–298.
- [24] N. Docquier & P. Fisette, A scaled–bogie test bench to understand and demystify wheel/rail contact dynamics, in: *Multibody Dynamics 2011–ECCOMAS Thematic Conference*, 2011.
- [25] D. Fletcher & J. Beynon, Development of a machine for closely controlled rolling contact fatigue and wear testing, *Journal of testing and evaluation*, 28 (2000) 267–275.
- [26] T.D. Armstrong, Measurements and predictions of wheel–rail vibration using a 1/5th scale rig, in: *University of Southampton*, 2004.
- [27] J. Zhu, D. Thompson & C. Jones, On the effect of unsupported sleepers on the dynamic behaviour of a railway track, *Vehicle System Dynamics*, 49 (2011) 1389–1408.
- [28] M.P. Papaelias, C. Roberts, C. Davis, M. Lugg & M. Smith, Detection and quantification of rail contact fatigue cracks in rails using ACFM technology, *Insight–Non–Destructive Testing and Condition Monitoring*, 50 (2008) 364–368.
- [29] C. Heliot, Small–scale test method for railway dynamics, *Vehicle System Dynamics*, 15 (1986) 197–207.
- [30] P. Allen, Chapter 15, Scale Testing, in *Handbook of railway vehicle dynamics* in: S. Iwnicki (Ed.), CRC Press, Boca Raton FL (USA), 2006.
- [31] A. Matsumoto, Y. Sato, H. Ono, Y. Wang, M. Yamamoto, M. Tanimoto & Y. Oka, Creep force characteristics between rail and wheel on scaled model, *Wear*, 253 (2002) 199–203.
- [32] A. Savkoor & G. van der Schoor, Slip–time history influences on the interaction between friction and wear in contaminated rolling contacts of wheel–rail systems, *Wear*, 162 (1993) 980–984.
- [33] K. Bruzelius & D. Mba, An initial investigation on the potential applicability of Acoustic Emission to rail track fault detection, *NDT & E International*, 37 (2004) 507–516.
- [34] Y. Jin, M. Ishida & A. Namura, Experimental simulation and prediction of wear of wheel flange and rail gauge corner, *Wear*, 271 (2011) 259–267.
- [35] M. Takikawa & Y. Iriya, Laboratory simulations with twin–disc machine on head check, *Wear*, 265 (2008) 1300–1308.
- [36] B. Allotta, L. Pugi, M. Malvezzi, F. Bartolini & F. Cangioli, A scaled roller test rig for high–speed vehicles, *Vehicle system dynamics*, 48 (2010) 3–18.
- [37] A. de Pater & Y. Gu–Ang, The Geometrical Contact between a Pair of Rollers and a Wheelset in a Railway Vehicle Roller Rig, in: *Dynamical Problems of Rigid–Elastic Systems and Structures*, Springer, 1991, 179–189.
- [38] P.T. Torstensson, J.C.O. Nielsen & L. Baeza, Dynamic train–track interaction at high vehicle speeds—Modelling of wheelset dynamics and wheel rotation, *J Sound Vib*, 330 (2011) 5309–5321.

- [39] J.C.O. Nielsen, High-frequency vertical wheel-rail contact forces—Validation of a prediction model by field testing, *Wear*, 265 (2008) 1465–1471.
- [40] S. Grassie, R. Gregory, D. Harrison & K. Johnson, The dynamic response of railway track to high frequency vertical excitation, *Journal of Mechanical Engineering Science*, 24 (1982) 77–90.
- [41] N. Chaar & M. Berg, Simulation of vehicle-track interaction with flexible wheelsets, moving track models and field tests, *Vehicle System Dynamics*, 44 (2006) 921–931.
- [42] X. Zhao & Z. Li, The solution of frictional wheel-rail rolling contact with a 3D transient finite element model: Validation and error analysis, *Wear*, 271 (2011) 444–452.
- [43] X. Zhao, Z. Li & J. Liu, Wheel-rail impact and the dynamic forces at discrete supports of rails in the presence of singular rail surface defects, *Proceedings of the Institution of Mechanical Engineers, Part F: Journal of Rail and Rapid Transit*, 226 (2012) 124–139.
- [44] R.P.B.J. Dollevoet, Design of an Anti Head Check profile based on stress relief, in, University of Twente, 2010.
- [45] H. Jenkins, J. Stephenson, G. Clayton, G. Morland & D. Lyon, The effect of track and vehicle parameters on wheel/rail vertical dynamic forces, *Railway Engineering Journal*, 3 (1974).
- [46] K. Knothe & S. Grassie, Modelling of railway track and vehicle/track interaction at high frequencies, *Vehicle system dynamics*, 22 (1993) 209–262.
- [47] X. Zhao, Z.L. Li & R. Dollevoet, The vertical and the longitudinal dynamic responses of the vehicle-track system to squat-type short wavelength irregularity, *Vehicle System Dynamics*, 51 (2013) 1918–1937.
- [48] X. Zhao, Z. Li & R. Dollevoet, Influence of the fastening modeling on the vehicle-track interaction at singular rail surface defects, *J Comput Nonlin Dyn*, (2014).
- [49] D.J. Thompson & J.W. Verheij, The dynamic behaviour of rail fasteners at high frequencies, *Appl Acoust*, 52 (1997) 1–17.
- [50] M. Burstow, Improving track geometry alignment to reduce rolling contact fatigue (RCF), in: *Proceedings of 9th World Congress on Railway Research (WCRR-2011)*, Lille-France, 2011, 22–26.
- [51] E. Hiensch, J. Horst, P. Wiersma, B.F. van der Linden, B. Lapidair & R. Dollevoet, Relationship between Track Geometry Disturbances and the Development of Rolling Contact Fatigue Damage, in: *Proc. 7th World Congress on Railway Research (WCRR 2006)*, Montreal, Canada, 2006.
- [52] A. Jaschinski, H. Chollet, S. Iwnicki, A. Wickens & J. Würzen, The application of roller rigs to railway vehicle dynamics, *Vehicle System Dynamics*, 31 (1999) 345–392.
- [53] T. Armstrong & D. Thompson, Use of a reduced scale model for the study of wheel/rail interaction, *Proceedings of the Institution of Mechanical Engineers, Part F: Journal of Rail and Rapid Transit*, 220 (2006) 235–246.
- [54] B.G. Eom, B.B. Kang & H.S. Lee, Design of small-scaled derailment simulator for investigating bogie dynamics, *International Journal of Railway*, 4 (2011) 50–55.
- [55] J. Koch, N. Vincent, H. Chollet & O. Chiello, Curve squeal of urban rolling stock—Part 2: Parametric study on a 1/4 scale test rig, *J Sound Vib*, 293 (2006) 701–709.
- [56] R.C. Spoorenberg, H.H. Snijder & J.C.D. Hoenderkamp, Finite element simulations of residual stresses in roller bent wide flange sections, *Journal of Constructional Steel Research*, 67 (2011) 39–50.
- [57] A.H. Gandhi & H.K. Raval, Analytical and empirical modeling of top roller position for three-roller cylindrical bending of plates and its experimental verification, *Journal of Materials Processing Technology*, 197 (2008) 268–278.
- [58] Z. Li, X. Zhao, C. Esveld, R. Dollevoet & M. Molodova, An investigation into the causes of squats—correlation analysis and numerical modeling, *Wear*, 265 (2008) 1349–1355.

- [59] M. Oregui, S. Li, A. Núñez, Z. Li, R. Carroll & R. Dollevoet, Monitoring bolt tightness of rail joints using axle box acceleration measurements, *Structural Control and Health Monitoring*, (2016).
- [60] S.L. Grassie, Rail corrugation: Characteristics, causes, and treatments, *Proceedings of the Institution of Mechanical Engineers, Part F: Journal of Rail and Rapid Transit*, 223 (2009) 581–596.
- [61] S. Grassie & J. Kalousek, Rail corrugation: characteristics, causes and treatments, *Proceedings of the Institution of Mechanical Engineers, Part F: Journal of Rail and Rapid Transit*, 207 (1993) 57–68.
- [62] E. Magel, P. Sroba, K. Sawley & J. Kalousek, Control of rolling contact fatigue of rails, in: *AREMA 2004 Annual Conference*, Nashville, TN , USA, 2004.
- [63] J. Wu, R.H. Petrov, M. Naeimi, Z. Li, R. Dollevoet & J. Sietsma, Laboratory simulation of martensite formation of white etching layer in rail steel, *International Journal of Fatigue*, 91 (2016) 11–20.
- [64] M. Oregui Echeverria–Berreyarza, Vertical railway track dynamics: from measurements to numerical modelling, PhD thesis, TU Delft, Delft University of Technology, 2015.





# 4

## Chapter 4 A new characterization procedure for reconstructing RCF defects based on computed tomography

*In the previous chapter, a new test rig was developed to characterise the nature of squat defects by cyclic testing. This chapter describes the development of an advanced detection and characterization tool based on computed tomography (CT) for studding squat cracks. This technique is used as a non-destructive approach to examine young squats.*

*Section 4.1 presents an overview of the existing detection techniques for detecting rail defects. Section 4.2 addresses the details of the rail samples taken from the Dutch railway network for CT observations. The settings of the CT scanner are described in Section 4.3. The detailed procedures of the CT experiment and post-processing work are described in Section 4.4. The CT results are compared with metallographic observations in Section 4.5. Discussions are made in Section 4.6 regarding the sizing effect and the accuracy of CT measurements.<sup>1</sup>*

---

<sup>1</sup> This chapter is based on the following publication:

*M. Naeimi, Z. Li, Z. Qian, Y. Zhou, J. Wu, R.H. Petrov, J. Sietsma & R. Dollevoet, Reconstruction of the rolling contact fatigue cracks in rails using X-ray computed tomography, NDT & E International, 92 (2017) 199–212.*

## 4.1 Introduction

Rolling contact fatigue (RCF) is an important form of damage in wheels and rails that is typically associated with surface and subsurface cracks. RCF cracks often develop with complex patterns in subsurface materials and can potentially cause broken wheels or rails. To study the nature of RCF defects and their behaviours, it is of great value to characterize the crack geometries, networks and patterns. This characterization will become more interesting if it can provide proper understanding of various types of RCF defects, such as head checks and squat defects. Squats in Europe are currently the dominant form of rail RCF that incurs the most maintenance costs and imposes the most threat to operational safety.

The detection, characterization and monitoring of RCF cracks in rails have been important topics in the literature. Serial cutting (or multi-sectioning) can help reconstruct the geometry of subsurface cracks. This method involves the following steps: (i) specimen sectioning and subsequent recording with optical microscopy in sequential slices; in this stage, indentations with known dimensions, i.e., known hardness, are marked as a depth reference; and (ii) alignment of 2D cracks in separate sections and rebuilding a three-dimensional volume with available software packages. For example, this method has been applied to RCF cracks in [1] to build up the 3D data on crack shapes and characteristics. However, this method has the following limitations: 1) It is significantly destructive without the possibility of retrieving the original sample. 2) Metallographic examination of rail samples is time-consuming and laborious. 3) Furthermore, parallel slices can be made along only one single axis, typically normal to the primary crack alignments. 4) The number of possible cross-sections is limited, which causes data loss on the fracture. The word ‘fracture’ is used interchangeably with ‘crack’ in this research, as it is often used by computed tomography (CT) experts. 5) The thickness of the cutting blades causes loss of material, which leads to discontinuity in crack patterns.

### 4.1.1 Computed tomography vs. ultrasonic and eddy current measurement

Due to the above-mentioned limitations of serial cutting, the non-destructive inspection tools are more promising for the early detection and characterization of RCF defects. These tools have been widely used for quality control in many industrial fields, e.g., during the manufacturing process of rails or for the damage inspection of rails in service. A comprehensive review of non-destructive systems for evaluating rail defects was published in [2]. Traditionally, ultrasonic and eddy current testing are the most common inspection techniques for the non-destructive detection of rail defects. Both methods have been widely used to detect the presence of fatigue cracks or internal rail defects [3].

Despite the widespread application of ultrasonic and eddy current testing, these testing techniques have limitations in detecting rail defects, particularly at the early stage. Shadowing effects and the shielding of overlapped cracks in ultrasonic examination hinder the detection of shallow head checks and squat cracks [3]. Ultrasonic inspection has difficulty with detecting cracks with a depth of less than 4 mm by rough estimation. Eddy current can detect small, shallow surface cracks. However, overestimation of small cracks and inaccuracies in crack sizes have been limitations that threaten the reliability of eddy current measurements [4,5]. The typical crack depth that can be detected by eddy current is 0.3–5 mm. Furthermore, when there is group of cracks in a defect cluster, shallower cracks may mask deeper defects. Therefore, the defect depth might be underestimated [6].

The detection of small, shallow cracks near the surface is important because RCF cracks are typically small and shall when first forming. It is also essential to determine the geometry of cracks at different life stages to understand the initiation and development process of RCF defects. The above-mentioned techniques provide some insight into the presence of RCF

cracks despite their aforementioned limitations. However, detailed information on the geometries of the RCF cracks cannot be obtained. The crack pattern on the surface can be characterized by microscopic observations or even by the naked eye, depending on the scales. However, shallow subsurface cracks are difficult to evaluate, as available non-destructive methods fail to access their 3D geometries.

CT is a potentially more powerful non-destructive technique for characterizing internal fractures than ultrasonic and eddy current methods. Using X-ray images taken from different angles, the CT technique can reproduce the cracks in three dimensions while avoiding the inaccuracies in the detection of shallow cracks and shielding of overlapped cracks. In this research, we use the CT technique to measure and reconstruct the RCF crack network in steel. The CT scan settings, measurement process and subsequent data post-processing are discussed in detail. Cross-sectional (tomographic) images are collected from the CT scans for each reconstruction. These X-ray images are processed and compiled to form the 3D volumetric data, including internal fractures, with the available commercial software. Various image processing tools are then used to detect surface and subsurface cracks in the bulk steel. Finally, the 3D geometry of the internal crack networks is reconstructed. In this chapter, four rail specimens with different RCF severities were examined to show the potential of the CT technique for detecting and reproducing RCF cracks. Metallographic experiments were conducted to validate the reconstructions.

#### 4.1.2 CT vs. SEM, TEM and EBSD

Figure 4.1 shows the crack development and potential methods to detect and characterize the cracks with the categorized dimensions. As shown in this figure, it is challenging, if not impossible, for the non-destructive method to detect and reconstruct RCF cracks at the meso and micro scales. An alternative advanced automatic damage reconstruction is 3D EBSD [7], which can also be performed by SEM and TEM [8]. The disadvantages of SEM, TEM, and EBSD are their 1) destructiveness, 2) limited specimen dimensions, 3) tedious data collecting process, and 4) lack of information on the locations and orientations of the subsurface cracks to prepare the initial sample.

In this research, we could generate high-resolution images of the cracks at the macro, meso and micro scales. Although all the studied RCF defects were visible at the macro scale, the detectability of the X-ray images was adequate to detect crack tips and branches up to the micro level. Thus, CT is shown to be able to bridge the gap between the methods for macro cracks and the methods for micro and nano cracks, as shown in Figure 4.1. When this gap is filled, one will be able to trace down the complete crack development process to allow for the study of the complete evolution process of the RCF cracks. When the complete crack geometry is reconstructed with a CT scan, a sample and cracks can be viewed and studied in any arbitrary 3D orientation, e.g., axial, transverse or normal planes. The crack dimensions and orientations can be measured accurately in a virtual workspace, which includes the sample geometry with internal fractures. With this information, a proper understanding of the initiation and growth mechanism of such defects can be obtained. When the locations and orientations of the RCF cracks are known using the CT scan, small samples can be prepared to encompass the internal crack network. Such samples can be further analysed using advanced crystallographic characterization techniques, such as EBSD, SEM or TEM.

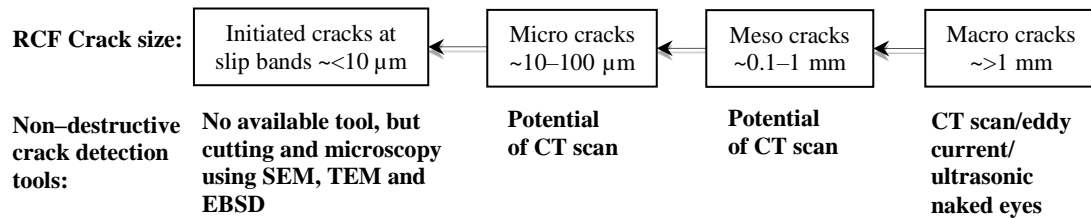


Figure 4.1. RCF crack development: sizes of the cracks on the different scales and the appropriate non-destructive detection tests

#### 4.1.3 Relevant history of CT technology

In addition to medical applications, CT is used in other fields, such as non-destructive material testing and archaeological studies [9]. Industrial CT generates a 3D representation of the objects and internal structures. CT has occasionally been used to inspect internal damage in materials; see, e.g., the applications to aluminium alloys [10], polymer composites [11], soil aggregates [12,13] and concrete [14,15]. CT has also been used to detect RCF cracks in high-strength steel with artificial defects [16,17]. Some fundamental works on the CT technology and its applications can be found in [18–20].

Nicholson et al. [21] used X-ray tomography to determine the size and morphology of the RCF cracks in cylindrical samples machined from a rail. RCF cracks at different levels, a light and a moderate one, were reconstructed, and their shapes and sizes were measured. Another research, devoted specifically to the RCF of rail materials [22], proposed different methods to describe the squat crack networks geometrically. The methods were a mixture of destructive and non-destructive, i.e., X-ray radiography, metallography, X-ray tomography, and topography. A recent study [23] introduced the application of X-ray CT to head checks. They collected 3D information on several head checks and quantified the geometry of the internal cracks.

The studies [21–23] were pioneering in introducing the capability of X-ray radiography to railway applications. However, there is still a lack of research on: 1) the application of a CT scan to squats of different severities to track the geometry of squats at different growth stages; 2) designing CT specimens with squats considering the sizing effect and sample orientation; 3) describing the CT scanning procedure, CT settings and associated post-processing work; and 4) validating the CT measurements with metallographic observations. Considering this knowledge gap, this chapter presents the results of CT measurements on RCF defects of different severities and discusses the CT scan process, apparatus settings, required sample dimensions, post-processing methods, verifications and limitations of the technique. Furthermore, this chapter provides an experiment-based design for future CT experiments.

## 4.2 Sample preparation

Rail samples with defects of different severities were prepared to develop the CT process. We chose rail pieces with squat damage because there has been less understanding of the initiation mechanism and geometry of squat cracks among the various types of RCF defects. Squats have a complex crack network in the rail surface and at the subsurface. Hence, characterization of squat cracks is of particular interest for this research.

The samples were taken from a straight track between Meppel and Leeuwarden in the Dutch railway network, as shown in Figure 4.2. The rail is of the UIC 54 standard of grade R260 Mn. The rail was manufactured in 1989 and was loaded with an annual traffic of approximately 3.65 million gross tons [24]. Numerous squats were found at different places; some are marked with arrows in Figure 4.2.

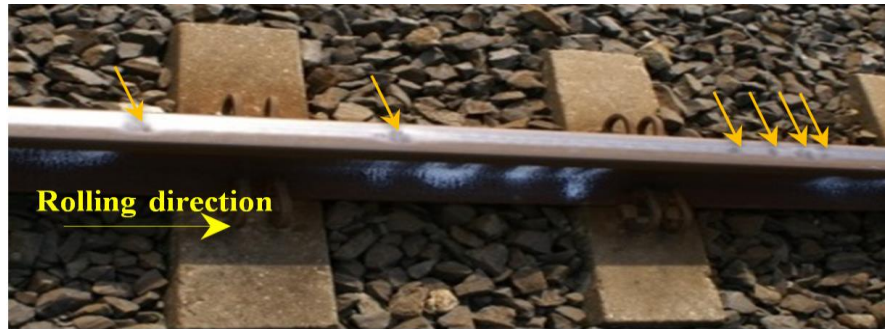


Figure 4.2. A straight track between Meppel and Leeuwarden with visible squat defects; the arrows show the locations of squats

Table 4.1 provides an overview of the selected defects, the corresponding specimens and the CT experiments conducted in this research. Three defects were chosen for CT examinations: one squat Class B, one squat Class A and one baby squat. The classification into classes A and B is according to [25], which is in line with UIC 712 and the Dutch rail defect guidelines. The third defect is smaller than a Class A squat and does not fall into any category in the current classification proposed by [25]. In this research, we use the term ‘baby squat’ for that type of defect.

Four specimens were prepared from the three defects: Specimen 1 with a moderate squat (Class B), Specimens 2a and 2b with a light squat (Class A) and Specimen 3 with a baby squat. Specimens 2a and 2b were made from the same defect (light squat) but had different dimensions to study the influence of sample size on the CT results. Specimen 2a is larger and was further cut to form Specimen 2b after finishing the CT experiment of Specimen 2a.

Table 4.1. Overview of the selected defects, prepared specimens and CT experiments

Rail Defects	Specimens	Visible Cracks at Surface According to Figure 4.3	CT Experiments
Class B squat (moderate squat)	Specimen 1	3 crack openings, sizes of 25, 9 and 18 mm	Scan-1
Class A squat (light squat)	Specimen 2a	2 crack openings, sizes of 10 and 2 mm	Scan-2
	Specimen 2b		Scan-3
Baby squat	Specimen 3	2 crack openings, sizes of 6 and 0.8 mm	Scan-4

Figure 4.3 shows the top view of the selected defects when photographed in the field, together with the final specimens prepared for the CT experiments. The dimensions of the specimens are also given. In the figure, RD is the rolling direction, GC is the gauge corner side on the railhead and small arrows indicate the location of the studied cracks. The moderate squat and its corresponding sample (Specimen 1) are shown in Figure 4.3 (a). Specimens 2a and 2b, prepared with a light squat, are shown in Figures 4.3 (b) and (c), respectively. In Specimen 2a, there is a moderate squat next to the small one. This moderate squat was not examined, and we focused on the small one. Figure 4.3 (d) shows the baby squat and its respective specimen (Specimen 3). All three squats contain surface crack openings visible to the naked eye. The surface features of these squats were characterized using an optical microscope. Prior to CT measurements, samples were lightly polished using 1  $\mu\text{m}$  diamond suspensions from Struers to remove dirt and rust. The corresponding images of the surface crack openings (alignments) in the selected squats are shown on the right side of Figure 4.3.

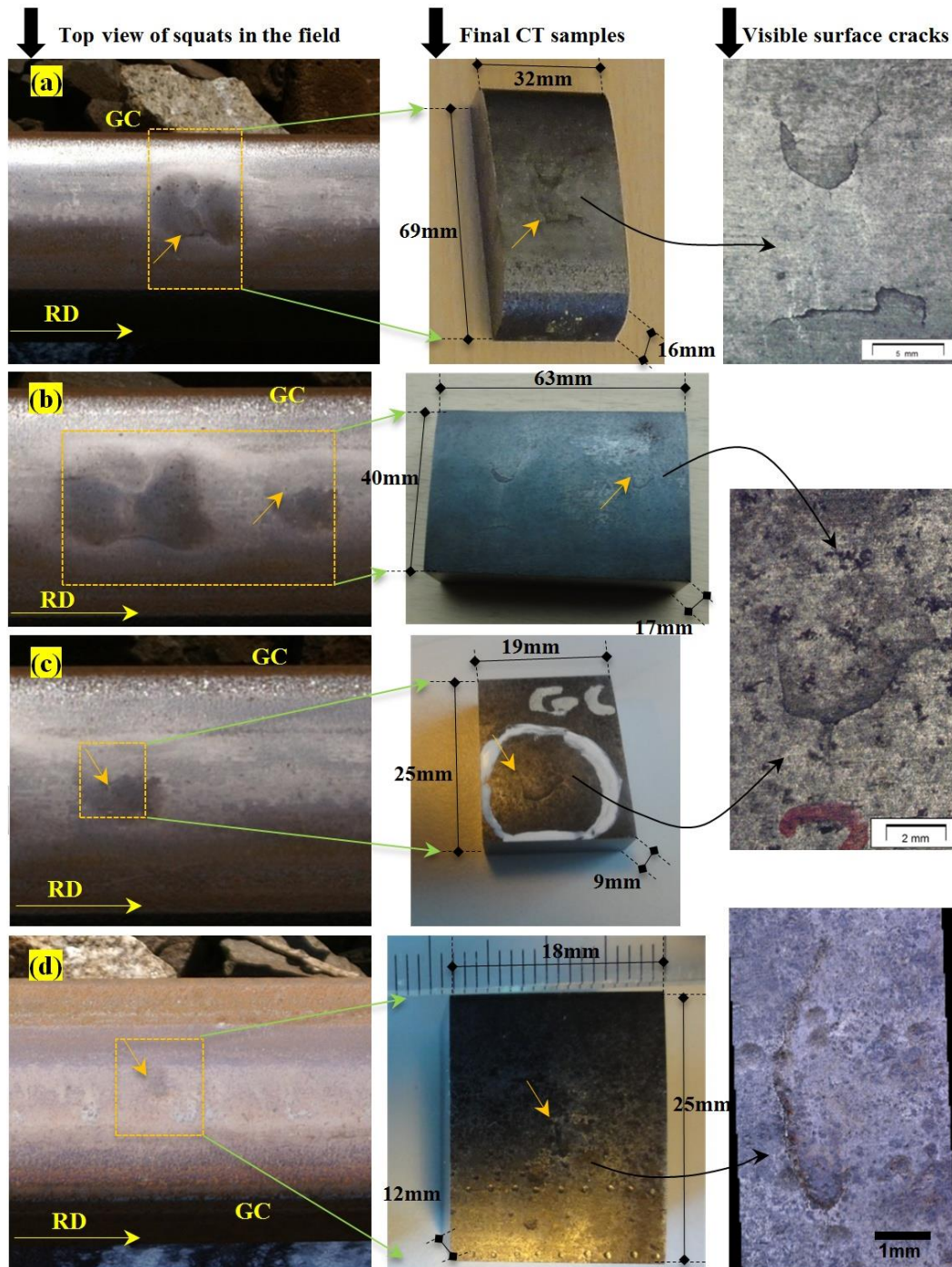


Figure 4.3. Top view of the selected squat defects and final samples prepared for CT; small arrows indicate the location of the studied cracks: (a) moderate squat, Specimen 1, (b) light squat, Specimen 2a, (c) light squat, Specimen 2b, and (d) baby squat, Specimen 3. The crack openings in the rail surface, seen under the microscope, are shown on the right.

### 4.3 CT scan settings

Electromagnetic radiation to objects is the basis of CT scanning. CT provides a non-destructive measurement of the geometry of the object by measuring the difference in the attenuation of the X-ray beams when passed through the object. The X-ray photons are generated, after the so-called target metal was hit by a beam of high-energy charged particles, e.g. electrons. Differences in material density and thickness can change the intensity

of the final penetrated photon beams. The penetrated photons are collected by the corresponding detector and the contrast is generated due to the variation of the photon beam intensities. Accordingly, if cracks exist in the bulk rail material, the density in the crack areas will be different from those crack-free areas, and therefore the cracks can be recognized in the recorded image. The detailed mechanism of CT technology can be found in classical medical CT works, e.g., by Godfrey Hounsfield [26].

In an industrial CT scanner, X-ray beams are radiated from the source to the object, and a series of two-dimensional (2D) X-ray images is progressively generated in an array detector; see Figure 4.4(a). The target sample rotates step-by-step through a full 360° revolution at increments of user-designed steps. The sample can also translate into the vertical and horizontal directions to provide a complete projection of the sample on the CT images. The 2D projections contain the object features within the absorbing sample, including bulk steel, fracture geometry, imperfections and non-uniformities. X-ray images are recorded in an array detector, located in the cabinet. The outputs are stored in a computer.

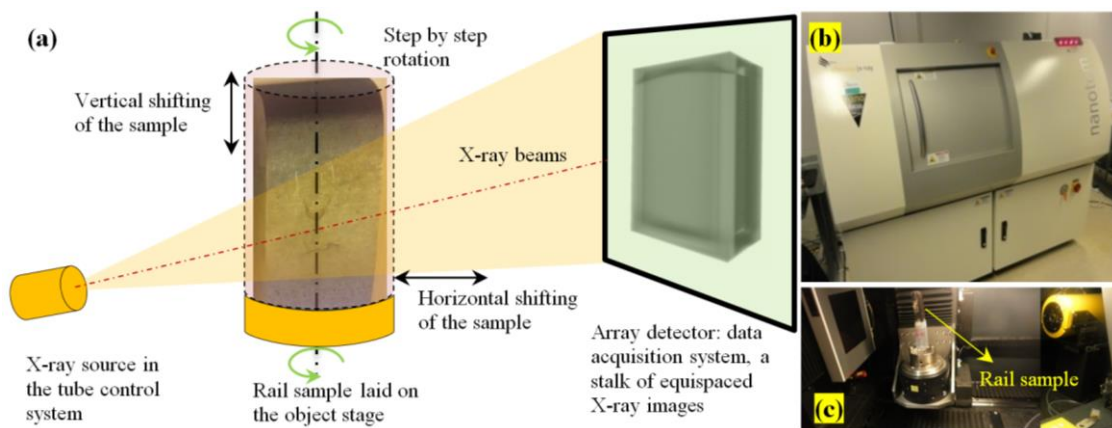


Figure 4.4. (a) Schematic of the X-ray CT scanning process showing X-ray beams emitted to the rail object and collected by the detector, (b) Phoenix Nanotom high-resolution CT scanner, and (c) inside view of the CT cabinet with the rail sample glued on the object support

A Phoenix Nanotom™ micro CT scanner, shown in Figure 4.4(b), was used in the present research. Rail samples are laid and glued on an object platform before being inserted into the CT scanner. The X-rays are generated at 180 kV, and the maximum spatial resolution (minimum voxel size) is 300 nm. Such a high resolution is the maximum nominal capability of the CT device; the actual resolution is dependent on the type of materials studied, sample size, radiation power, and storage capacities. A voxel size of  $12\ \mu\text{m} \times 12\ \mu\text{m} \times 12\ \mu\text{m}$  was used to study RCF cracks in the rail steel in the present research considering the size of the prepared specimens. The highest detectability of the facility is down to 200 nm. The object platform is located between the X-ray source and data acquisition screen, as shown in Figure 4.4(c).

Figure 4.5 shows the specimen configuration and applicable rotation axes in the CT scanner. Each specimen is a rectangular block with three dimensions ( $W$ ,  $D$  and  $L$ ), as shown in Figure 4.5(a). The longest dimension of each block ( $L$ ) is set along the rotation axis to allow X-ray beams to travel along a shorter distance through the specimen to arrive at the detector. Hence, the quality of measurements can be improved.



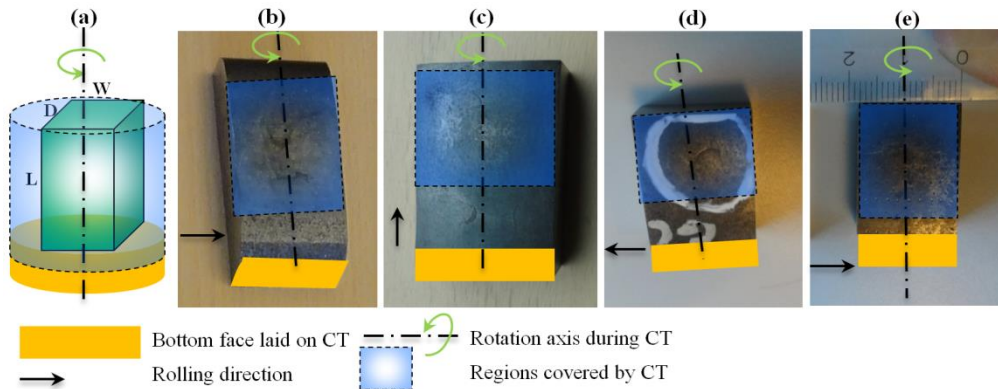


Figure 4.5. Positioning of the rail specimen in the CT apparatus: (a) general configuration and (b, c, d, e) positions of the four specimens studied in this research; the dimensions (W, D and L) are given in Figure 4.3

#### 4.4 Collection and process of the CT scan data

Figure 4.6 schematically illustrates the general procedure used for CT measurements in this research. Three main stages can be identified, with a brief description of each stage provided below.

In Stage I, the CT device scanned the rail specimen and X-ray images at different rotating steps recorded from the sample while the sample rotates inside the cabinet (acquisition of raw data). The data are stored in a high-capacity workstation next to the CT, in which the raw data are processed to generate 3D discretized cubes, called voxels (calculating the voxel data). The voxel data are not compatible with image processing codes, such as MATLAB and ImageJ. An intermediate data format known as DICOM (Digital Imaging and Communications in Medicines) is used to create readable CT data. DICOM-formatted files combine images and metadata to create a rich description of the studied material. DICOM files are generated in the three orthogonal directions, i.e., the longitudinal, transverse and normal directions; see the Cartesian coordinate system in Figure 4.7(a), which is used as a convention in this research.

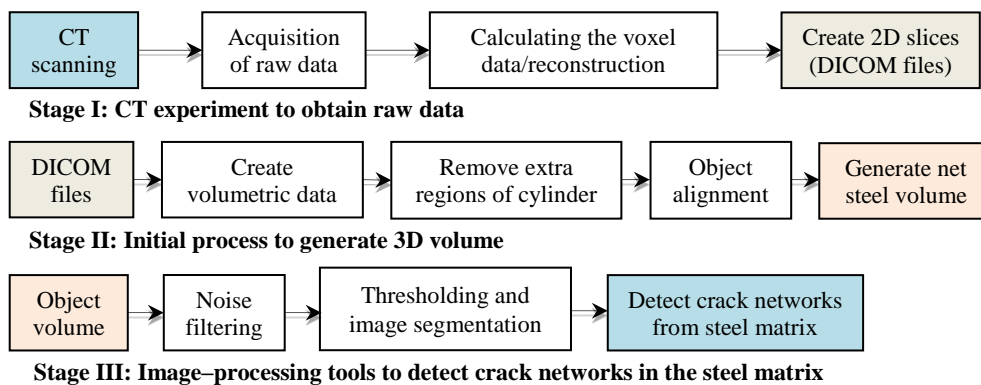


Figure 4.6. General procedure used for detecting and reconstructing internal crack networks in rails using the CT scan technique

In Stage II, DICOM files are compiled into image processing software to create the 3D visualization of the specimen (create volumetric data). As noted above, three sets of DICOM files are made available by the end of Stage I, and each of them can be uploaded to create the volumetric data. As shown in Figures 4.5(a) and 4.7(b), the initial volume created by the DICOM files is a cylinder due to sample rotation during the scan (full 360° rotation). The absolute steel volume is obtained by subtracting the rail block from the initial cylinder to acquire an absolute volume that is geometrically equivalent to the original objects (remove

additional regions of the volume). Then, the final volume is properly aligned along the main orthogonal axes (object alignment).

It should be noted that only one set of images in any orthogonal direction will contain the full data of the volume. Three sets were, however, generated as it provides high-quality 2D images in each orthogonal direction for the need of a user who only requires the 2D images and does not intend to perform the 3D defect reconstruction. Hence, a good directory of 2D images will be available for each defect prior to 3D reconstruction.

In Stage III, image processing tools are used to distinguish between the fracture and intact bulk steel. The employed tools are image filtration, image thresholding and image segmentation. Slight filtration is applied to the X-ray images to remove extremely high or low intensities that are locally generated in X-ray measurements. This noise mainly arises near the edges of the specimen due to the edge effect [27], originated from significant differences in the attenuation of the X-ray photon beam intensities when X-rays start to penetrate into the metal. The X-ray images acquired for the rail steel without fracture are homogeneous, with a uniform intensity level in the binary images. However, in fracture regions, the image intensities vary, making the cracks detectable. Image thresholding is applied to detect the internal crack alignments. The intensity of the X-ray images at cracks differs from that for the bulk steel. This difference in the intensity helps detect all crack alignments in X-ray images. Image segmentation divides the digitized images into multiple segments depending on the intensity level. After partitioning, different materials are labelled with specific identifications. In this research, segmentation is made only to distinguish between cracks and the bulk steel. Those pixels of the digitized images that have different intensities from surrounding materials are labelled as cracks. The remaining pixels are labelled as the bulk steel. This process helps detect all crack alignments in each image. The final 3D crack geometry is made by combining the crack alignments of the 2D images together and by creating 3D surfaces that encompass those 2D alignments. The results of the CT experiments for the studied defects are presented below.

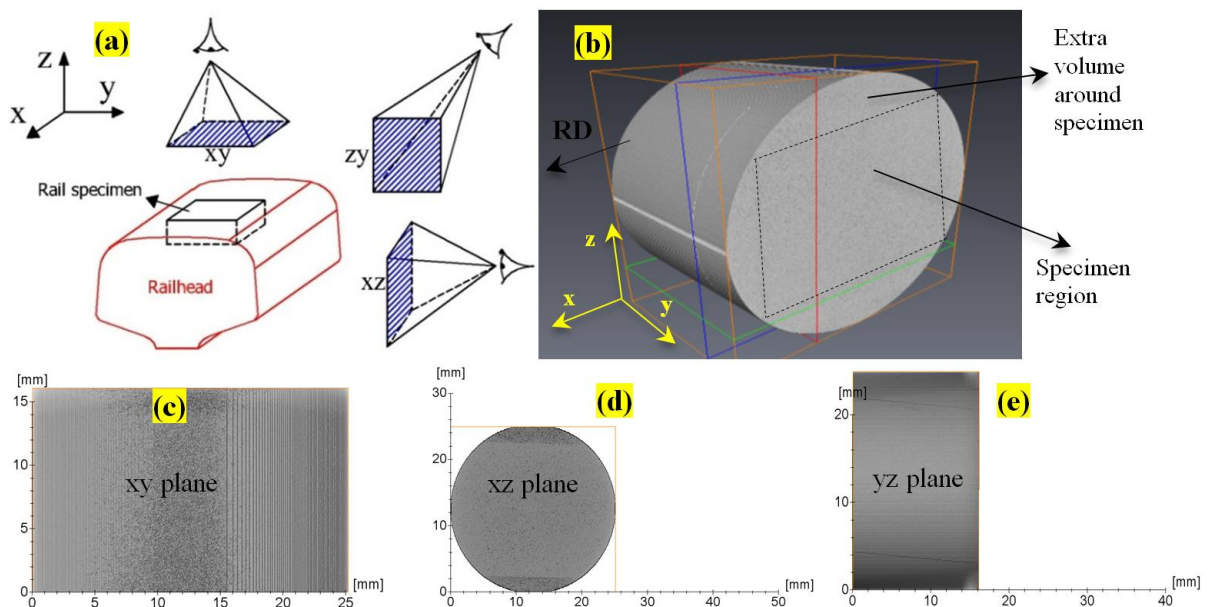


Figure 4.7. (a) Coordinate system adopted for 3D representation;  $x$ ,  $y$  and  $z$  are the main orthogonal axes, and  $xy$ ,  $yz$  and  $xz$  are the main orthogonal planes; (b) 3D visualization of the CT data in Specimen 1, which is a cylinder containing the specimen geometry. The dashed rectangle shows the absolute object in the initial cylinder; (c, d, e) 2D views of the object. The first specimen is given as an example.

#### 4.4.1 Crack reconstruction in the moderate squat

Figure 4.8 illustrates the 3D visualization of Specimen 1 based on the primary source of 2D images obtained from the CT measurement. All CT images are compiled into the global coordinate system to create the volumetric data. The reconstructed 3D object contains X-ray data on the rail steel material, external boundaries, potential defects and internal cavities. A blue interactive thresholding is used in Figure 4.8 to highlight the crack alignments within the sample. This figure also illustrates the main orthogonal axes (x, y, z) and the rolling direction (RD) of the trains on the rail. According to the above-mentioned description, the absolute rail object is located below the dashed line marked as the rail surface in Figure 4.8.

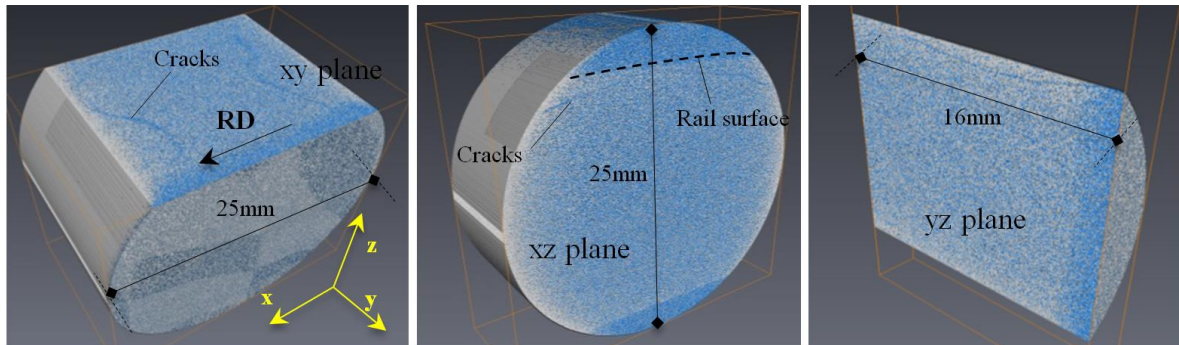


Figure 4.8. 3D visualization of Specimen 1; three orthogonal slices on the object, blue interactive thresholding is used to highlight the fracture

The post-processing results for Specimen 1 are shown in Figure 4.9. The 3D reconstructed rail object is shown in Figure 4.9(a). Figure 4.9(b) shows a magnified view of the RCF crack in Figure 4.9(a). In Figure 4.9(c), the same crack is shown with a higher magnification, at which image pixels can be identified. The pixel size in the X-ray measurements of the xy plane was  $12\ \mu\text{m} \times 12\ \mu\text{m}$ ; see Figure 4.9(c). The object in the Z direction was made using an adequate number of DICOM files (2,084 files) to reach cubic voxels with dimensions of  $12\ \mu\text{m} \times 12\ \mu\text{m} \times 12\ \mu\text{m}$ .

Figures 4.9(d, e, f) provide an example of crack detection in a 2D X-ray image, where the crack is labelled with a different colour (blue) using the thresholding and segmentation tools described above. Apart from crack zones, the bulk steel had a uniform and homogeneous structure. The crack alignment (blue pixels) was extracted and is shown with different magnifications in this figure.

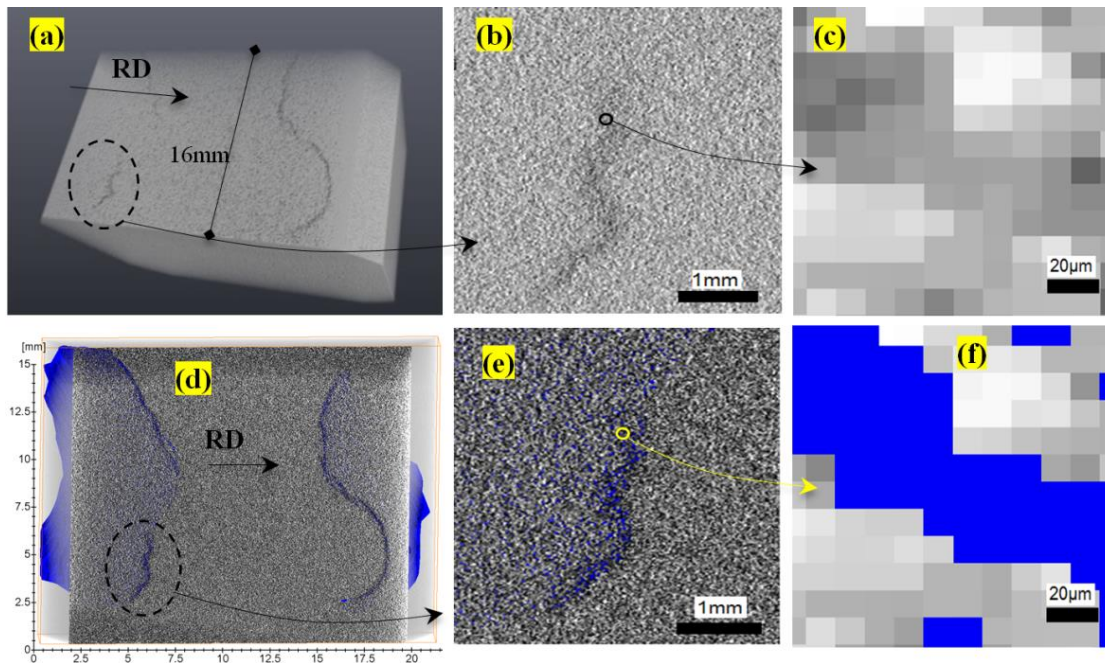


Figure 4.9. Post-processing of the CT data in Specimen 1: (a) the 3D reconstructed rail object; (b) magnified view of a sample crack in the X-ray measurements; (c) the same crack at higher magnification, where image pixels are detectable; (d) detecting and labelling the fracture (blue) in the bulk steel (grey) using thresholding and segmentation tools; (e) magnified view of the detected crack; and (f) crack-labelled regions at high magnification up to the pixel resolution.

After detecting crack alignments in all the 2D images and labelling them with the same identification, a 3D surface encompassing the 2D alignments was created. This 3D surface includes the internal crack networks detected by image segmentation. Figure 4.10 shows the 3D rail object with the internal crack network, where the blue crack is distinct from the grey bulk steel. Different transparency levels are used in the grey bulk steel in Figure 4.10(a, b, c) to highlight the internal fracture. In Figure 4.10(d, e, f), three orthogonal slices are displayed on the cracked volume with dimensioned gridlines.

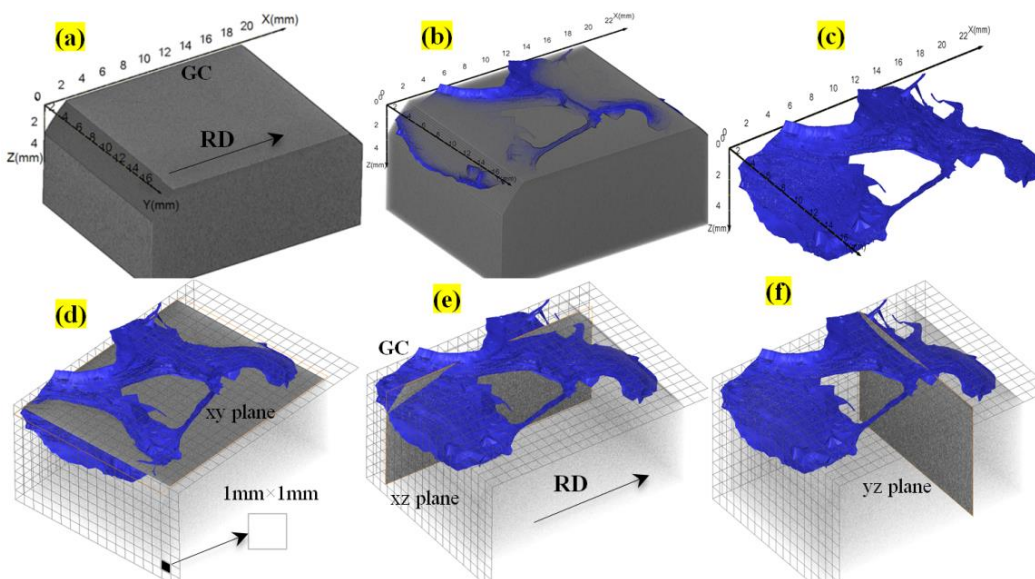


Figure 4.10. Reconstructed 3D object with an internal crack network in Specimen 1: (a) no transparency is applied on the grey bulk steel; (b) 50% transparency is applied on the grey bulk steel; (c) the internal fracture is made 100% visible by switching the bulk steel off; and (d, e, f) three orthogonal slices are displayed on the cracked volume with dimensioned gridlines.

#### 4.4.2 Crack reconstruction in the light squat

The same procedure was employed to assess Specimens 2a and 2b with a light squat. The post-experiment results of Specimen 2a are plotted in Figure 4.11. This figure shows a 3D representation of the bulk steel with an anticipated internal fracture. The bulk steel is represented by the grey colour, and the crack is represented in blue. Three orthogonal slices are shown in Figures 4.11(d, e, f).

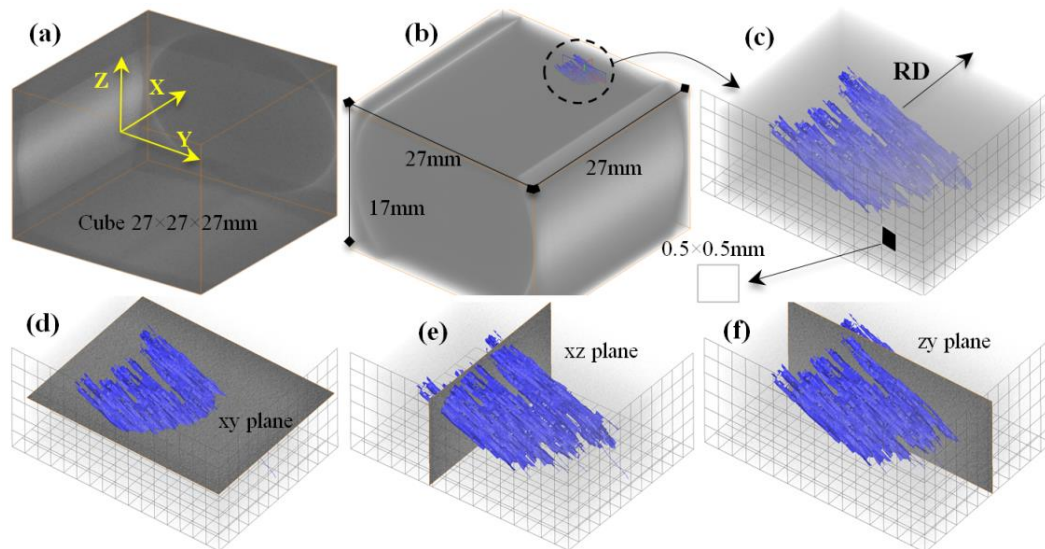


Figure 4.11. CT results of Specimen 2a: (a) 3D visualization of the object, including cracks; (b) detecting and labelling the internal cracks; (c) closer view of the crack at higher magnification with transparent grey steel; and (d, e, f) three orthogonal slices on fractured regions with dimensioned gridlines.

The reconstructed crack shown in Figure 4.11 has an incomplete and unexpected morphology. CT could roughly detect a subsurface crack; however, it failed to identify the complete geometry of the cracks due to the lack of penetration of the X-rays due to the large thickness of the sample. Then, we reduced the specimen dimensions by further cutting to improve the scanning and to obtain results with higher quality; see Specimen 2b in Figure 4.3 and the results in Figure 4.12. The post-experiment results of Specimen 2b are presented in Figures 4.12(a–f). The captured data on the cracks were adequate to create a complete 3D network. Figures 4.12(g, h, i) show the continuity of the reconstructed 3D crack network at the crack tip with different magnifications.

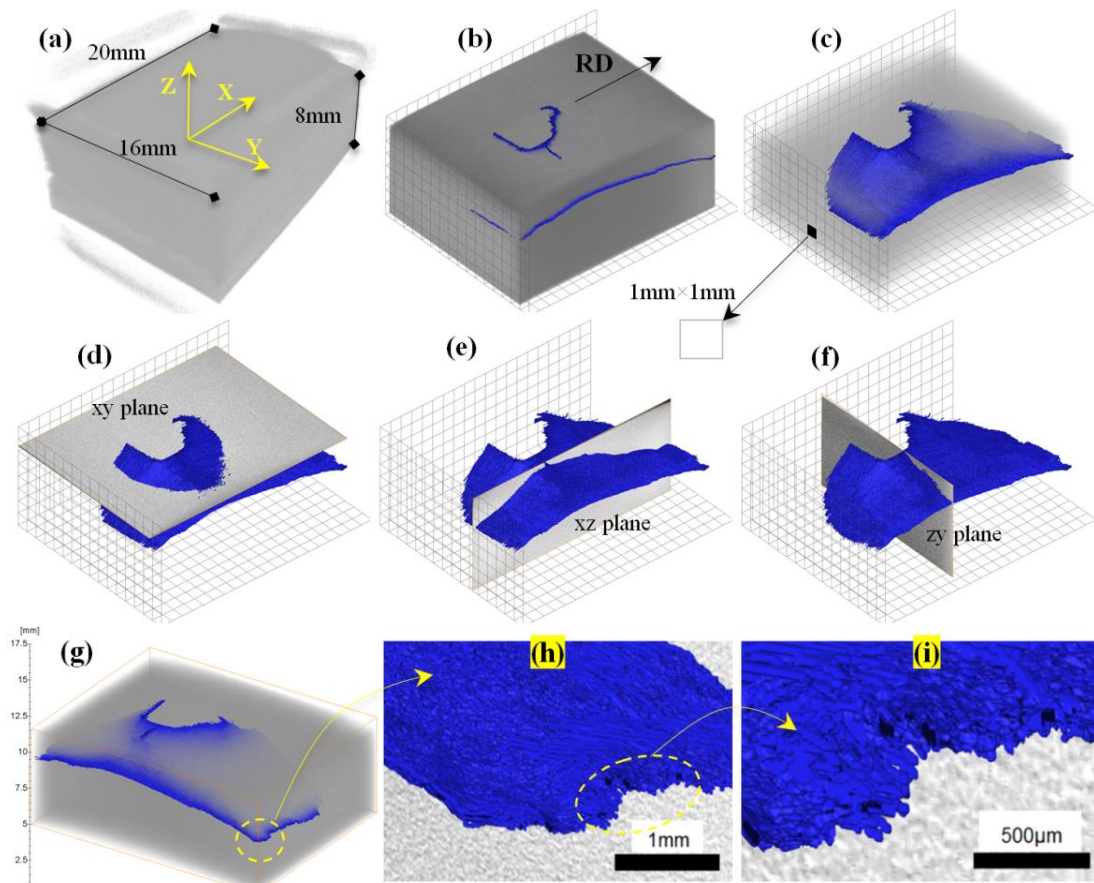


Figure 4.12. CT results of Specimen 2b: (a) 3D visualization of the CT object prior to applying image processing tools to crack detection; (b) the internal crack network is labelled in blue with no transparency on the grey steel; (c) the same object with 50% transparency is applied on the grey steel; (d, e, f) three orthogonal slices are displayed on the cracked volume with dimensioned gridlines; and (g, h, i) the crack tip at different magnifications

Figure 4.13 shows the crack reconstruction in Specimen 2b. Figure 4.13(a, b) demonstrates an example of 2D X-ray measurement, where the cracks can be detected with high quality. Two magnified views of the crack are shown in Figure 4.13(c, d). The image pixels are labelled in blue in Figure 4.13(e) to be distinguished from the bulk steel. Figure 4.13(f) shows the maximum detectability of X-ray measurements. Figure 4.13 shows that the pixel size is approximately  $12\ \mu\text{m}$ , which is approximately 60 lower than the maximum capability of the CT apparatus (detectability of  $200\ \text{nm}$ ). This detectability was sufficiently high to accurately detect the chosen RCF defects, as is further discussed in the validation section below. This level of detectability created X-ray images with the adequate contrast between the bulk steel and existing cracks.

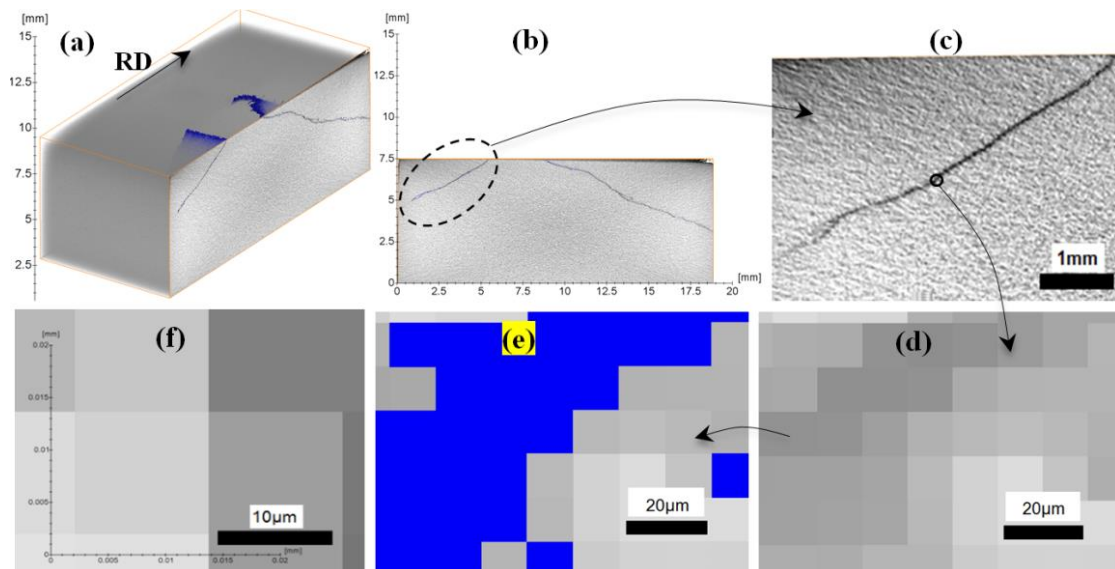


Figure 4.13. Crack detection in Specimen 2b: (a, b) example of 2D X-ray measurements in the xz plane; (c) magnified view of the crack; (d) magnified view of the crack up to the pixel resolution; (e) same image after the crack being segmented and labelled with blue; and (f) maximum resolution of the X-ray image with a visible pixel size.

#### 4.4.3 Crack reconstruction in the baby squat

The internal crack network was determined for the baby squat (Specimen 3) using the same procedure as described above. The post-processing results are shown in Figure 4.14. The original CT object prior to crack detection is shown in Figure 4.14(a). The internal crack network was determined and is shown in Figure 4.14(b, c). Similar to the other specimens, three orthogonal slices are illustrated in the cracked region to show the geometry of the cracks in different 2D planes. The 3D crack network in this specimen was highly accurate, as further discussed in the validation section. The two small white holes in the 3D crack network are negligible openings compared to the entire geometry.

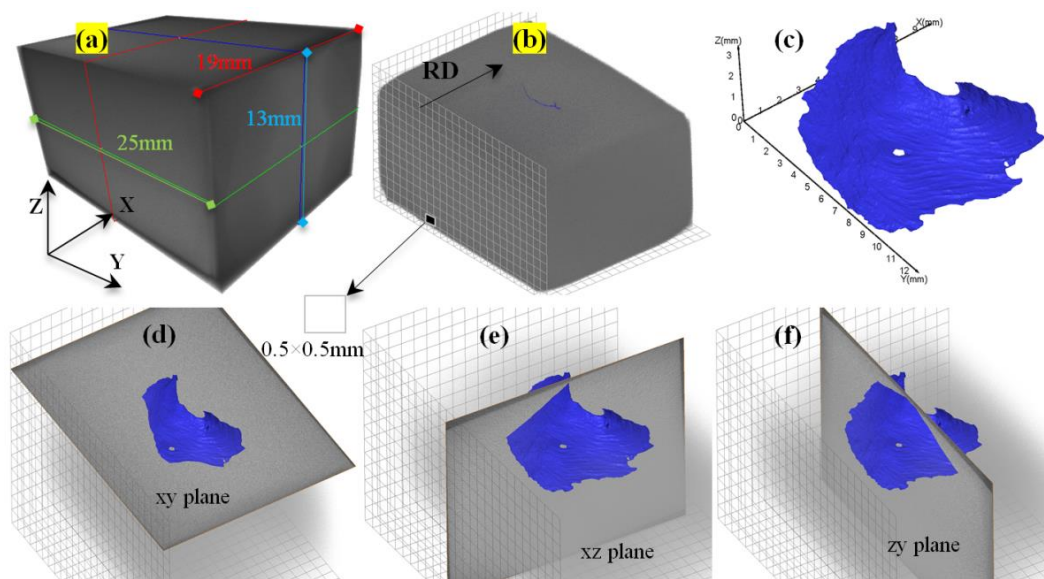


Figure 4.14. Reconstructed 3D object with an internal crack network in Specimen 3: (a) 3D visualization of the original CT data; (b) the rail object after detecting internal cracks with no transparency applied to the grey steel; (c) the 3D crack network is made visible by switching the steel off; and (d, e, f) three orthogonal slices are displayed on the cracked region with dimensioned gridlines

Figure 4.15 shows the crack detection and labelling in the high-contrast X-ray images. One 2D slice is shown here as an example. The X-ray image before and after the crack detection is illustrated in Figures 4.15(b, c), and Figures 4.15(d, e, f) show the high contrast of the X-ray images up to the pixel level. The blue regions in Figure 4.15(f) represent part of the detected crack network. The pixel size in Figure 4.15(d) was approximately 12  $\mu\text{m}$ , equal to the other studied specimens.

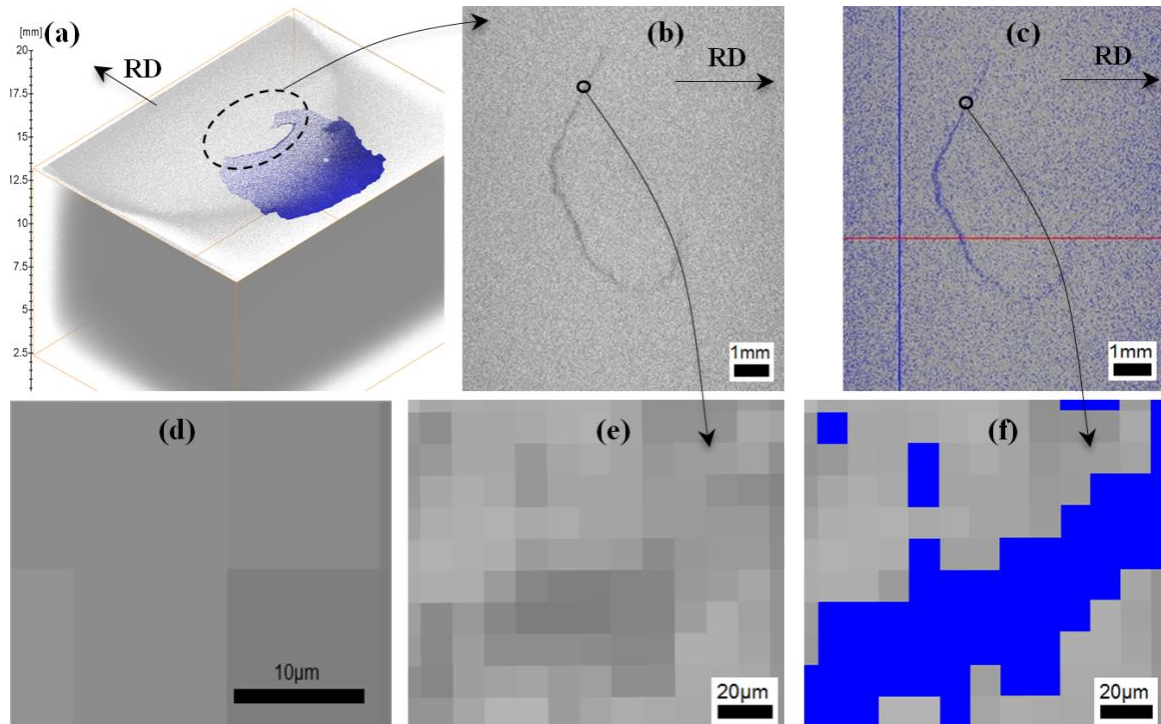


Figure 4.15. Crack detection procedure in Specimen 3: (a) the xy (railhead) view of the 3D reconstructed object; (b) magnified view of a sample crack in the X-ray measurements; (c) same image after the crack was detected and labelled with blue; (d) maximum resolution of the X-ray images with visible pixel size; and (e, f) magnified view of the crack up to the pixel resolution.

## 4.5 Validation

The quality of the CT measurement for detecting cracks can be evaluated by comparing the CT results with metallographic observations. Microscopy was performed on the top view of the specimens to observe the crack alignments of the rail surface. This section compares the fracture pattern of the rail surface between two measurements, i.e., CT and microscopy.

### 4.5.1 The moderate squat

Three crack alignments were identified on the rail surface of the moderate squat, i.e., C1, C2 and C3, as shown in Figure 4.16. These cracks were measured with microscopy (Figure 4.16(b)) and with CT (Figure 4.16(c)). Figure 4.16(d) compares the results of these two measurements. This figure shows that CT could accurately reconstruct these crack alignments. C2 and C3 were nearly identical in the two measurements. The extension of C1 at the top-right corner was not shown in the CT measurements, as the crack was considerably large and CT captured only the middle region. The rail sample can be shifted vertically, as shown in Figure 4.4(a), to capture the upper extensions of C1 by further scanning.



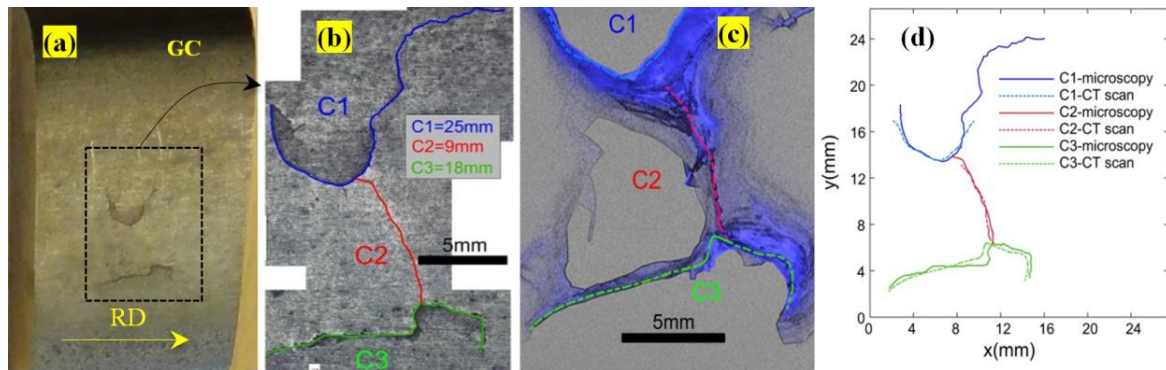


Figure 4.16. Measured surface crack alignments in the moderate squat: (a) top view of the specimen; (b) crack alignments C1, C2 and C3 measured with microscopy; (c) crack alignments detected by CT; and (d) comparing the results of the two measurements.

According to Figure 4.16, CT detected the surface cracks with a high quality. However, the 3D crack network given in Figure 4.17(a) has an internal cavity in the measured crack network (referred to as a missed region). Figures 4.17(b, c) illustrate an orthogonal slice crossing this region. There are two possibilities for why this result was obtained. The first possibility is that part of the real crack network was missed in the reconstructed crack in this region; see the dashed line in Figure 4.17(b). The second possibility is that there is no crack in this region. The scanned specimen was subsequently cut at sites of the missed region to clarify the existence of cracks. The specimen was checked under the optical microscope after cutting; see Figure 4.18(a, b). Figure 4.18(c) shows that there is a lunate crack in this section without crack discontinuity in the middle part, showing that the CT performed on the moderate squat was able to detect the crack network, but the defect at the subsurface was partially missed. According to these results, approximately 17% of the total crack network was missed due to the large size of the specimen used for the CT experiment; see the specimen size in Figure 4.3. The specimen size is further discussed in the following.

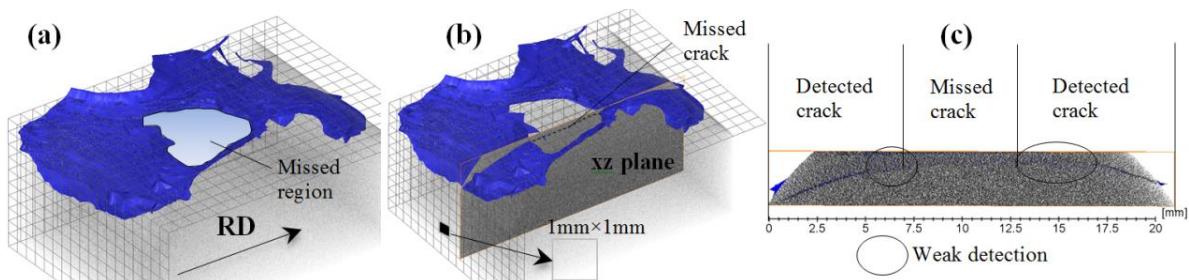


Figure 4.17. (a) Reconstructed 3D crack network with a region of the missing crack in Specimen 1; (b) orthogonal slice crossing at this region; and (c) 2D section (xz plane) with low crack detectability at the middle part.

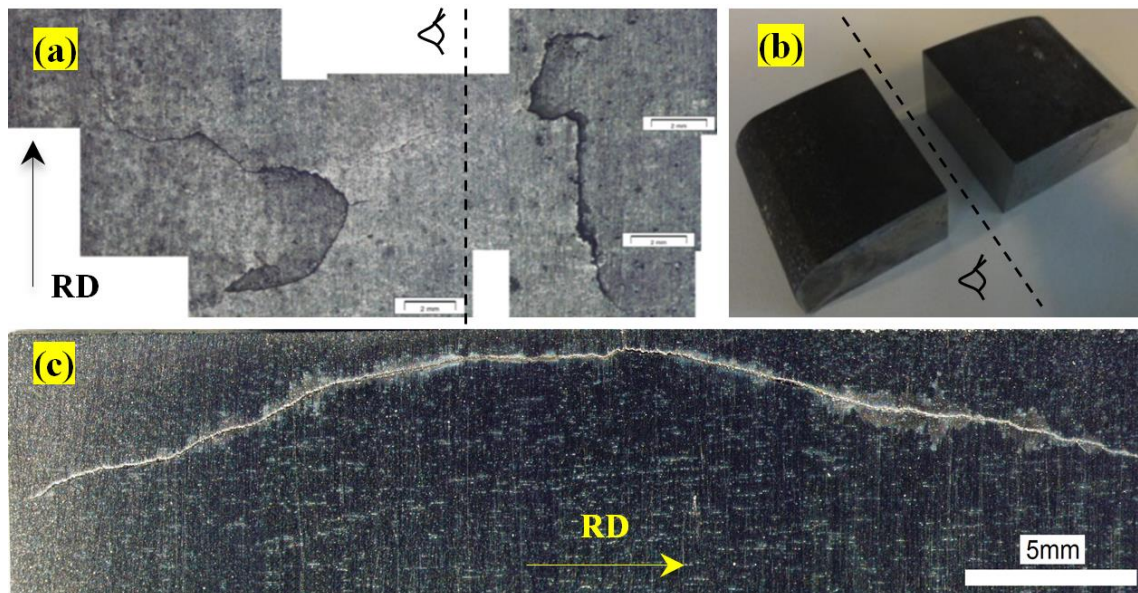


Figure 4.18. (a) Location of a cut in Specimen 1; (b) specimen after being cut; and (c) microscopic view of the rail section with a continuous lunate crack

#### 4.5.2 The light squat

Figure 4.19 compares the metallographic data of the surface cracks with the respective CT measurement of the light squat. A detailed geometry of the crack alignments is shown. According to these results, the crack alignments observed by microscopy were nearly identical to the cracks detected by CT. This measurement shows that CT could accurately detect the surface crack alignments in Specimen 2b; see the negligible differences in Figure 4.19(d). Such a high accuracy can be explained by the size of the specimen used in the experiment; see the dimensions in Figure 4.3. Specimens 2a and 2b contain the same defect (light squat). However, the quality of the CT measurement was significantly increased using the smaller specimen, as further explained in the discussion section.

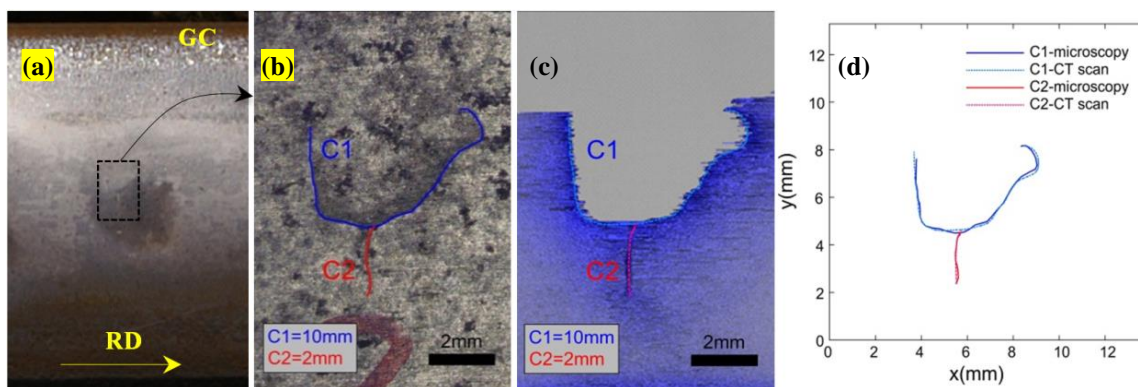


Figure 4.19. Validating the surface crack alignments in the light squat: (a) top view of the rail; (b) crack alignments C1 and C2 measured with microscopy; (c) crack alignments detected by CT; and (d) comparing the results of the two measurements

#### 4.5.3 The baby squat

The same validation procedure is adopted for the baby squat. Figure 4.20 shows the comparison between the metallographic data on the surface crack alignments and the CT result in this squat. As shown in Figure 4.20, the crack alignments reconstructed by CT were

nearly identical to the cracks observed under the microscope. This rail specimen, among all the specimens, yields the highest quality of CT measurements in this research.

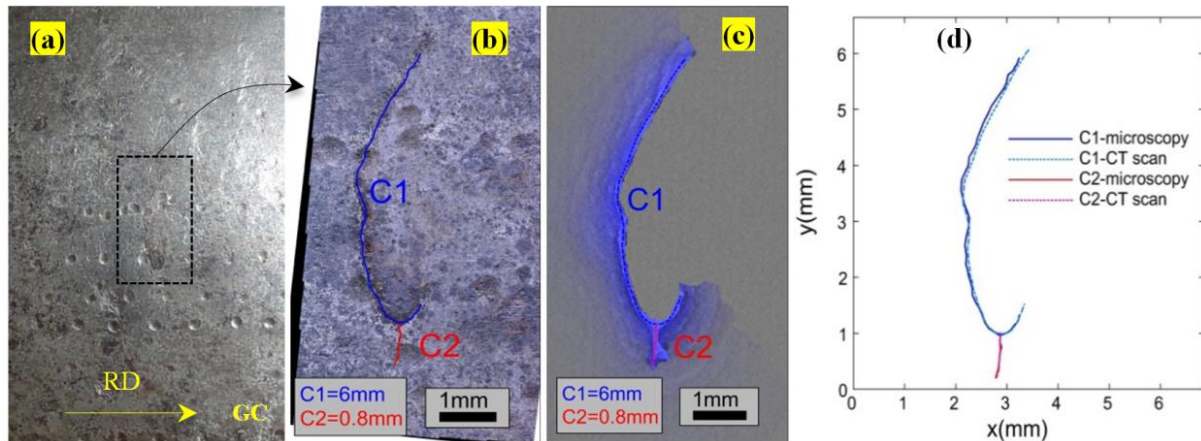


Figure 4.20. Comparing the microscopy results with CT measurement of the baby squat: (a) top view of the rail; (b) microscopy of the surface cracks; (c) CT measurement; and (d) comparing the crack geometries of the two measurements

## 4.6 Discussion

As noted above, the quality of the CT measurements in the different specimens is highly dependent on the specimen size. The maximum sample size, advised by the CT apparatus, is a cylinder with a radius of 240 mm and height of 250 mm. Such dimensions are considerably larger than the size of the rail specimens studied in this research. Large specimens with the advised size limits of the apparatus, if made of steel, yield low-quality CT measurements because the electromagnetic beams cannot easily penetrate through steel, which has a dense and homogeneous microstructure. Specimens 2b and 3, for which the CT measurements with the highest quality were obtained, were blocks of  $19 \times 8 \times 25$  and  $18 \times 12 \times 25$  mm<sup>3</sup>, respectively. Performing CT on the specimen with the moderate squat (dimensions  $32 \times 16 \times 69$  mm<sup>3</sup>) was not as good as performing CT on the other two measurements. Specimen 2a with dimensions of  $40 \times 17 \times 63$  mm<sup>3</sup> led to the weakest CT measurements due to the large specimen size.

In practice, the crack network in mature squats is relatively large, with crack branches and extensions. Such large cracks do not allow small specimens that contain the entire fracture to be made. The moderate and severe squats have cracks that are often larger than the size of the specimens with successful CT measurements in this research, i.e., Specimens 2b and 3. As an alternative solution, a severe squat can be divided (by cutting) into smaller specimens. High-quality CT results can then be obtained for each small specimen, and the complete crack network can finally be made by merging the results of separate divisions. Figure 4.21 compares the size of squat defects measured by CT scanning on different squats in this research. According to this figure, the size of the crack network in the baby squat (Figure 4.21(c)) was approximately  $12 \times 9 \times 2.5$  mm<sup>3</sup>, which fit well inside the chosen specimen (Specimen 3). However, the other squats were sufficiently large that they could not fit well in small specimens. Hence, part of the crack extensions at the subsurface have not been captured; see Figures 4.21(a, b).

A rough estimation of the boundaries of the complete cracks (crack tips at the subsurface) is shown in Figure 4.22. Only the top (railhead) views of the squats are shown. The three squat cracks are shown in a single graph to emphasize the size difference. This figure clearly shows that the crack tips are completely captured in the baby squat using one small CT specimen without crack loss at the cutting borders. As shown in the figure, parts of the cracks

at the other two squats (the moderate and light squats) were not measured, either due to cutting or due to the limits of the scanning region. In these squats, CT measured the regions inside the solid lines. A rough estimation of the crack tip locations in these squats is also provided by the dashed lines. These estimations were made by cutting and inspecting the remainder of the rail adjacent to the CT samples.

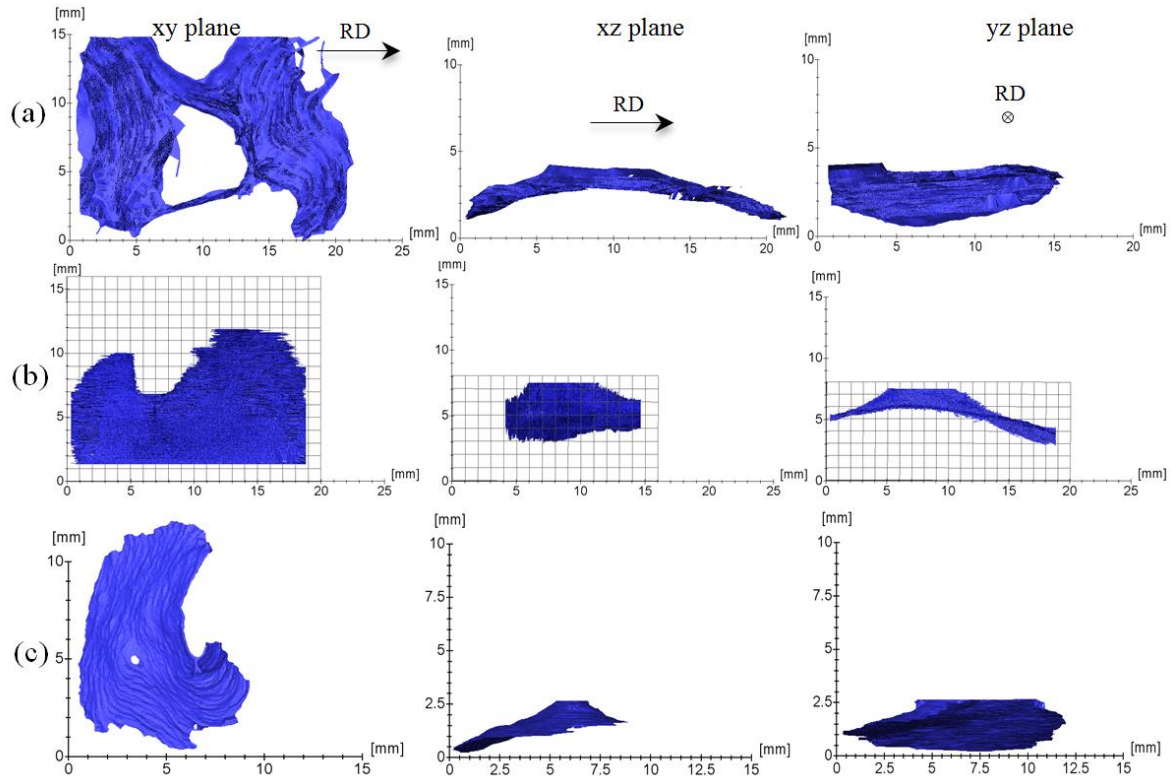


Figure 4.21. Size of the squat defects measured by CT scanning: (a) moderate squat; (b) light squat; and (c) baby squat

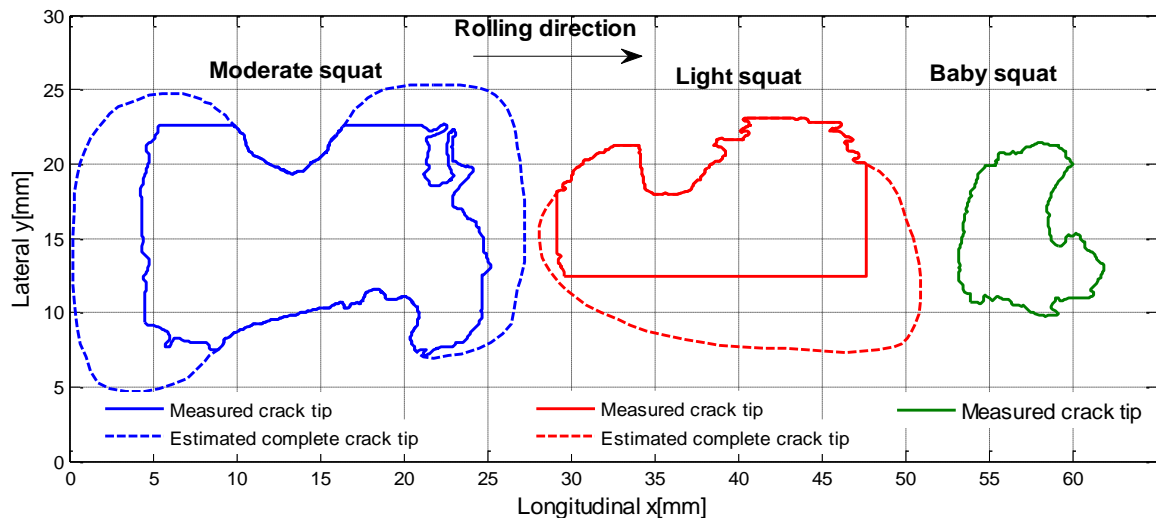


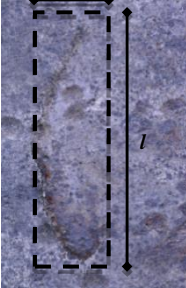
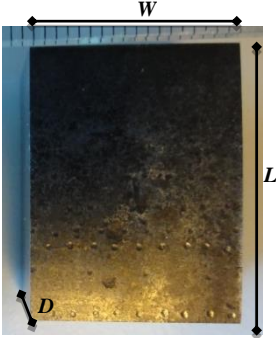
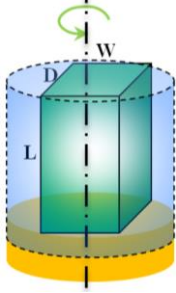
Figure 4.22. Crack tip alignments in the studied squats; continuous lines are the results of the CT scan, and the dashed lines are rough estimations of the crack tip locations made by the authors.

From the CT measurements performed in this research, a general recommendation is proposed in Table 4.2 for future CT experiments on rail steels. This recommendation will help obtain CT results with a high quality and reasonable post-experiment efforts. Three steps

have been formulated. In Step 1, a rectangular region including visible cracks in the rail surface is determined ( $w \times l$ ). Based on this crack region, two dimensions are determined for the final specimen ( $W$  and  $L$ ), with the size limits given in the table. The sample should be cut step-by-step, starting from large dimensions to smaller dimensions, to avoid cutting the sample at cracks. The last dimension ( $D$ ) is adopted within the rail depth direction.  $D$  is the minimum dimension, as squat defects often have shallow cracks. The final rectangular block of  $W \times L \times D$  will be a sufficiently small specimen to achieve a reconstruction of squat crack network with a high quality.

As explained, for one squat defect, part of the crack network is missed due to the large size of the specimen used for the CT experiment. Based on observations of different squats with various severities, we can conclude that if the rail sample would have been smaller (e.g. by cutting the original sample into several samples), the missing middle crack region could have been detected as well. Therefore, in this case, the large size of the sample accounts for the inaccuracy.

Table 4.2. Recommendations for the dimensions and CT scanning process for rail specimens with squats

Step 1	Step 2	Step 3
Measure the size of the visible crack on the rail surface: <ul style="list-style-type: none"> <li>• <math>l</math>: length</li> <li>• <math>w</math>: width</li> </ul> $w \times l$ : A rectangle that covers the visible crack $w$ : Smaller dimension of the rectangle $l$ : Larger dimension	Prepare the specimen with dimensions: <ul style="list-style-type: none"> <li>• <math>W \leq 25</math> mm</li> <li>• <math>L \leq 40</math> mm</li> <li>• <math>D \leq 15</math> mm</li> </ul> $W$ : Specimen width in the $w$ direction $L$ : Specimen length in the $l$ direction $D$ : Specimen depth	Assign $L$ to the CT rotation axis and perform the CT scan; the sample rotates around $L$ , and the largest travelling distance of the X-ray beams inside the sample in the $WD$ plane is $\sqrt{W^2 + D^2}$
		

## 4.7 Conclusions

This study investigated the use of CT for detecting and reconstructing rolling contact fatigue defects in rails. Four CT experiments were conducted on rail specimens with squat defects of different severities. A detailed description of the CT measurement and the post-experiment data processing was presented, followed by validating the CT reconstruction using metallographic observations of the rail surface cracks. The study revealed the potential of CT as a reliable technology for reconstructing RCF cracks. The following conclusions were drawn:

- 1) CT could detect the presence of squat cracks in all the studied specimens (crack detection).
- 2) Internal crack networks in the rail steel were accurately reconstructed using CT with proper specimen dimensions and with the described post-experiment processing (crack reconstruction).

- 3) The crack alignments observed by microscopy on the rail surface were nearly identical to the cracks detected by CT, which verified the reliability of CT observations.
- 4) The quality of the CT measurement for identifying the real geometry of internal cracks was dependent on the CT settings and the sample size. Crack geometries were rebuilt with a high quality in sufficiently small specimens (Specimens 2b and 3). The advised dimension limits for a cubic specimen of  $W \times L \times D$  is  $W \leq 25$  mm,  $L \leq 40$  mm, and  $D \leq 15$  mm, suggested for the available technological capability of industrial CT devices.
- 5) CT is more promising for young squats, i.e., squat Class A, baby squats and initiating squats, as they allow smaller specimens that could cover the entire crack network to be made. Young RCF cracks are within the size limits advised in this research. For squats of classes B and C, we suggest dividing the rail defect into multiple regions with sufficiently small dimensions for high-quality CT measurements. This partitioning will also allow mature squats to be measured with significantly high quality.

In general, CT was sufficiently potent and reliable for the non-destructive reconstruction of RCF crack networks. By choosing the appropriate settings and specimen size, CT could accurately reconstruct the 3D geometry of internal cracks in the baby, light and moderate squats, which enabled us to study different phases of squat crack development. The CT technique can be considered an intermediate detection and characterization tool between the methods for detecting macro cracks (cracks larger than 1 mm) and those for micro/nano cracks (cracks smaller than 10  $\mu\text{m}$ ) characterization. When the locations and orientations of the cracks are known using the CT scan, small samples encompassing the internal micro crack network can be prepared. These samples can be further analysed using advanced crystallographic characterization techniques, such as EBSD, SEM or TEM.

## 4.8 References

- [1] J.E. Garnham, D.I. Fletcher, C.L. Davis & F.J. Franklin, Visualization and modelling to understand rail rolling contact fatigue cracks in three dimensions, *Proceedings of the Institution of Mechanical Engineers, Part F: Journal of Rail and Rapid Transit*, 225 (2011) 165–178.
- [2] M.P. Papaelias, C. Roberts & C. Davis, A review on non-destructive evaluation of rails: state-of-the-art and future development, *Proceedings of the Institution of Mechanical Engineers, Part F: Journal of Rail and rapid transit*, 222 (2008) 367–384.
- [3] D. Cannon, K.O. Edel, S. Grassie & K. Sawley, Rail defects: an overview, *Fatigue & Fracture of Engineering Materials & Structures*, 26 (2003) 865–886.
- [4] Z. Popović, V. Radović, L. Lazarević, V. Vukadinović & G. Tepić, Rail inspection of RCF defects, *Metalurgija*, 52 (2013) 537–540.
- [5] J. Rajamäki, M. Vippola, A. Nurmikolu & T. Viitala, Limitations of eddy current inspection in railway rail evaluation, *Proceedings of the Institution of Mechanical Engineers, Part F: Journal of Rail and Rapid Transit*, (2016) 0954409716657848.
- [6] M. Lugg & D. Topp, Recent Developments and Applications of the ACFM Inspection Method and ASCM Stress Measurement Method, *ECNDT, 2006* (2006) 1–14.
- [7] H. Pirgazi, S. Ghodrati & L.A.I. Kestens, Three-dimensional EBSD characterization of thermomechanical fatigue crack morphology in compacted graphite iron, *Materials Characterization*, 90 (2014) 13–20.
- [8] T. Hashimoto, G.E. Thompson, X. Zhou & P.J. Withers, 3D imaging by serial block face scanning electron microscopy for materials science using ultramicrotomy, *Ultramicroscopy*, 163 (2016) 6–18.
- [9] S. Hughes, CT scanning in archaeology, computed tomography – special applications, Dr. Luca Saba (Ed.), *InTech*, DOI: 10.5772/22741.

- [10] O. Kuwazuru, Y. Murata, Y. Hangai, T. Utsunomiya, S. Kitahara & N. Yoshikawa, X-ray CT inspection for porosities and its effect on fatigue of die cast aluminium alloy, *Journal of Solid Mechanics and Materials Engineering*, 2 (2008) 1220–1231.
- [11] P.J. Schilling, B.R. Karedla, A.K. Tatiparthi, M.A. Verges & P.D. Herrington, X-ray computed microtomography of internal damage in fiber reinforced polymer matrix composites, *Composites Science and Technology*, 65 (2005) 2071–2078.
- [12] F. Zhu, J. Liao, S. Xue, W. Hartley, Q. Zou & H. Wu, Evaluation of aggregate microstructures following natural regeneration in bauxite residue as characterized by synchrotron-based X-ray micro-computed tomography, *Science of The Total Environment*, 573 (2016) 155–163.
- [13] D. Zhao, M. Xu, G. Liu, X. Yao, D. Tuo, R. Zhang, T. Xiao & G. Peng, Quantification of soil aggregate microstructure on abandoned cropland during vegetative succession using synchrotron radiation-based micro-computed tomography, *Soil and Tillage Research*, 165 (2017) 239–246.
- [14] X. Qin & Q. Xu, Statistical analysis of initial defects between concrete layers of dam using X-ray computed tomography, *Construction and Building Materials*, 125 (2016) 1101–1113.
- [15] Z. Yang, W. Ren, R. Sharma, S. McDonald, M. Mostafavi, Y. Vertyagina & T.J. Marrow, In-situ X-ray computed tomography characterisation of 3D fracture evolution and image-based numerical homogenisation of concrete, *Cement and Concrete Composites*, 75 (2017) 74–83.
- [16] T. Makino, Y. Neishi, D. Shiozawa, Y. Fukuda, K. Kajiwara & Y. Nakai, Evaluation of rolling contact fatigue crack path in high strength steel with artificial defects, *International Journal of Fatigue*, 68 (2014) 168–177.
- [17] T. Makino, Y. Neishi, D. Shiozawa, S. Kikuchi, S. Okada, K. Kajiwara & Y. Nakai, Effect of defect shape on rolling contact fatigue crack initiation and propagation in high strength steel, *International Journal of Fatigue*, 92, Part 2 (2016) 507–516.
- [18] A.C. Kak & M. Slaney, *Principles of computerized tomographic imaging*, SIAM, 2001.
- [19] T.M. Buzug, *Computed tomography: from photon statistics to modern cone-beam CT*, Springer Science & Business Media, 2008.
- [20] W.A. Kalender, *Computed tomography: fundamentals, system technology, image quality, applications*, John Wiley & Sons, 2011.
- [21] G. Nicholson, A. Kostryzhev, X. Hao & C. Davis, Modelling and experimental measurements of idealised and light-moderate RCF cracks in rails using an ACFM sensor, *NDT & E International*, 44 (2011) 427–437.
- [22] C. Jessop, J. Ahlström, L. Hammar, S. Fæster & H.K. Danielsen, 3D characterization of rolling contact fatigue crack networks, *Wear* 366, (2016) 392–400.
- [23] Y. Zhou, X. Zheng, J. Jiang & D. Kuang, Modeling of rail head checks by X-ray computed tomography scan technology, *International Journal of Fatigue*, 100, Part 1 (2017) 21–31.
- [24] S. Li, J. Wu, R.H. Petrov, Z. Li, R. Dollevoet & J. Sietsma, “Brown etching layer”: A possible new insight into the crack initiation of rolling contact fatigue in rail steels?, *Engineering Failure Analysis*, 66 (2016) 8–18.
- [25] Z. Li, X. Zhao, C. Esveld, R. Dollevoet & M. Molodova, An investigation into the causes of squats—correlation analysis and numerical modeling, *Wear*, 265 (2008) 1349–1355.
- [26] G.N. Hounsfield, Computerized transverse axial scanning (tomography): Part 1. Description of system, *The British journal of radiology*, 46 (1973) 1016–1022.
- [27] F.E. Boas & D. Fleischmann, Evaluation of Two Iterative Techniques for Reducing Metal Artifacts in computed tomography, *Radiology*, 259 (2011) 894–902.

# 5

## Chapter 5 Determining the angles of squat cracks via CT scanning and metallographic observations

*Using the process described in the former chapter, the present chapter investigates the angles  $\theta_1$ ,  $\theta_2$ , and  $\theta_3$  that squat crack faces form with respect to three orthogonal planes: the rail top, the longitudinal–vertical cross–section and the lateral–vertical cross–section. Rail samples with squats of various severities are obtained from the field. A 3D visualization method, together with the necessary geometric definitions, is developed for enabling effective measurement and characterization of the squat cracks (Section 5.2.1). The three–dimensional (3D) crack networks are reconstructed using computed tomography (CT) scanning and/or serial cutting (Section 5.2.2). In Section 5.3, the crack angles are estimated by numerical modelling. The crack orientations and variation of angle ranges are summarized and discussed in Section 5.4. Section 5.5 draws the conclusions on the occurrence frequency of the crack orientations, the angles and the order of V–shaped cracks associated with the squats.<sup>1</sup>*

---

<sup>1</sup> This chapter is based on the following publication:

M. Naeimi, Z. Li & R. Dollevoet, *Determining the angles of squat cracks via CT scanning and metallographic observations*, *Engineering Fracture Mechanics* 230 (2020) 107016.



## 5.1 Introduction

Squats are a type of rolling contact fatigue (RCF) that occurs in the railhead, and they can develop into rail fractures if they are not detected and treated effectively via maintenance measures. Squats occur mostly in the running band of rails and can create high dynamic forces. These defects are prevalent RCF defects in the Netherlands. They are often found in tangent tracks or shallow curves mostly in the form of isolated dark depressions in the railhead. They often have a two-lung shape appearance in their mature phase [1].

The severity of squats can be identified from their visual appearance in the rail surface as being light, moderate and severe [1]; the classification is explained in Section 5.2. Apart from dark depression, squat defects typically appear along with cracks in the rail surface and subsurface. In the present research, we consider the geometry of defect (dark depression and plastic deformation) as the “squat defect” or squat in short. The entire crack network (in the rail surface and subsurface) is considered as “cracks within squat” or squat cracks in short.

After initiation, squat cracks continue to grow. Researchers have studied the development process of squats when cracks were already present; see, e.g., [2, 3]. Squat cracks are numerically modeled in [2] to study the state of stress intensity factors in the vicinity of the crack front. A modeling approach is proposed in [3] for investigating the crack growth process. Both consider a plane oblique crack in the railhead and investigate its further development. Another example of the use of this approach can be found in [4].

Among the various stages of the squat crack evolution, the initiation phase is crucial. Researchers [5, 6] explained the fatigue initiation process using the microstructural features that are observed within squats. The early life of a rail squat is studied in [5], where three stages of crack formation have been identified for typical squats. They found that the early stage of crack initiation is due to ratcheting or to the formation of the white etching layer (WEL). According to a recent study [7], thermal effects could cause WEL formation and lower the shakedown limits. Metallurgical investigations were conducted on rails with squats in [6], where the influence of the microstructure was found to be crucial for the formation of squats.

Researchers [7–10] proposed numerical methods for estimating the stress–strain levels inside rails and for predicting the RCF initiation based on the finite element method (FEM) and contact mechanics. The material ratchetting response was found to be an initiation mechanism for RCF defects [8].

Squats typically have a complex crack network below the rail surface, especially when they are highly developed. The terms that are related to the crack geometry will be defined in Section 2.1. Among the various crack planes in a squat crack network, the crack planes that intersect the rail surface can potentially be the initiating cracks. Such crack planes must be studied to investigate the initiation phenomena that are behind the occurrence of squat defects.

The angles for the initiation of RCF cracks were calculated in [8] using the results from FEM simulations. Numerical predictions on crack angles for general RCF cracks can be found in [11, 12]. However, these references are not dedicated to rail squats but to crack initiation within the gauge corner contact, where head checks are more prevalent. Next to the experimental observations in the current research, a finite element model of the wheel–track system is employed for numerical calculation of the RCF crack angles.

A recent study [13] has investigated the formation of rail squats using five-year continual field monitoring data on many squats. Various stages of the complete life cycle of squats that were accompanied by cracks were analysed [13]. This analysis provides statistic observations of the locations and the angles of crack initiation of squats.

The visual appearance of squats varies from a single dark spot up to a complete two-lung shape footprint on the rail surface depending on the severity. Note that light and baby squats

(the classification is explained in Section 5.2) are sometimes difficult or even impossible to be identified by naked eyes. In the present study, we studied the subsurface state of squats (invisible part) using the proposed measurement techniques. This is possible by characterising the geometry of cracks that are associated with the squats.

The 3D geometry of the squat cracks under the rail surface has not been systematically investigated in the literature. Insufficient research has been conducted on measuring the crack angles of the squats via advanced methods such as metallography and computed tomography (CT). The present study seeks to remedy this lack of knowledge by offering metallographic and tomographic observations on squat defects of various severities.

Five rail samples with squat defects of various severities are obtained from the Dutch railway network and subjected to CT scanning and metallographic inspections. The 3D geometries of the subsurface squat crack networks are determined. Using these data, the crack angles are defined and measured. Afterwards, a categorization is proposed for the studied cracks and the characteristic ranges of the angles are determined for each category. The crack angles are also predicted by numerical simulations using a 3D model of the wheel–track system.

The focus in this chapter is on developing a 3D representation method for measuring the cracks through the following process: 1) the crack network is divided into a series of surface units; 2) the crack planes associated with each surface unit are determined, 3) conventions on the crack plane and crack angles are defined to create a common language for this research; 4) CT scanning and metallographic observations are performed on several squat defects (data collection); 5) the results are summarized, based on which, a classification for different cracks is presented; 6) numerical predictions on crack angles are presented to search for supporting evidence on the relationship between the crack initiation angles and the vehicle-track operational conditions. A reference multiaxial fatigue model is used in the last part for the fatigue initiation analysis.

## 5.2 Measuring squat crack angles that are formed at the rail surface

A straight track between Meppel and Leeuwarden in the Dutch railway network is selected for sampling the squats. The rail was manufactured in 1989 and was loaded with an annual gross tonnage of approximately 3.65 million tons [14]. Five rail samples that contain squats are obtained from various places along this track. Table 5.1 presents an overview of the studied defects and their classifications according to severity. The defects are classified into A and B (light and moderate squats) according to [1]. Severe squats (see Figure 5.1(c) of [1] for example) are not analyzed in the present study as their crack network are too complicated and not necessarily characteristic of squats anymore.

Two moderate squats and one light squat are studied; see Table 5.1. The term “baby squat” is suggested in [16]. The last defect (Sample–5) is smaller than a baby squat and does not fall into any category that was proposed by [1] or [16]. In this study, we use the term ‘initiating RCF crack’ for this type of defect as it is not certain whether this crack can grow to become a squat. Sample–1, Sample–3 and Sample–4 were used in [16] to demonstrate the CT scanning technique and Sample 3 was used in Figure 5.8(b) of [13] to show the 3D crack face of the peninsula.

Table 5.1. Overview of the selected samples and the crack reconstruction techniques

Sample	Internal TU Delft ID of the sample	Severity of squat/defect	Relevant figure	Reconstruction technique
Sample-1	TU-19	Moderate squat-Class B	Figure 5.2	CT Scanning
Sample-2	TU-17	Moderate squat-Class B	Figure 5.3	Serial cutting
Sample-3	TU-19	Light squat-Class A	Figure 5.4	CT Scanning
Sample-4	TU-10	Baby squat	Figure 5.5	CT Scanning
Sample-5	TU-10	Initiating RCF crack (potential squat)	Figure 5.6	CT Scanning-Serial cutting

According to Table 5.1, two techniques are used for the reconstruction of the crack networks: serial cutting and CT scanning. They are briefly described as follows. Serial cutting (or multisectioning) is a destructive metallographic method that can be used to reconstruct the geometry of subsurface cracks in defected rails. This method was used to inspect RCF cracks in [17], in which 3D data on crack shapes and characteristics were generated. Serial cutting involves the following steps: (i) a rail sample is sectioned in sequential slices by cutting; (ii) each section is recorded via optical microscopy (metallographic observation); and (iii) 2D cracks at separate sections are aligned and the final 3D volume is reconstructed.

CT is a nondestructive inspection tool that can produce a 3D visualization of an object, including its internal defects. This technique was recently used in [16] for the reconstruction of rail RCF defects. The CT scanning technique involves the following steps: (i) a rail sample is prepared and inserted into the CT scanner; (ii) X-ray images are captured of the object at various angles during the CT scan; (iii) the cross-sectional (tomographic) images are combined to form 3D volumetric data of the object, including its internal fractures; (iv) the tomographic data are further processed by using the image processing tools to detect all the surface and subsurface cracks in the bulk steel; and (v) the 3D geometry of the internal crack networks is reconstructed and is made available for quantification and visualization.

A Phoenix Nanotom™ micro CT scanner is used in the present research. Rail samples are laid and glued on an object platform before being inserted into the CT scanner. The X-rays are generated at 180 kV, and the maximum spatial resolution (minimum voxel size) is 300 nm. Such a high resolution is the maximum nominal capability of the CT device; the actual resolution is dependent on the type of materials to be studied, sample size, radiation power and storage capacities. A voxel size of  $12\ \mu\text{m} \times 12\ \mu\text{m} \times 12\ \mu\text{m}$  was used to study RCF cracks in the rail steel in the present research considering the size of the prepared specimens. The highest detectability of the facility is down to 200 nm. The object platform is located between the X-ray source and data acquisition screen [16]. More details of the measurement process and the subsequent data postprocessing are presented in [16]. By choosing the appropriate settings and specimen size, CT can accurately reconstruct the squat cracks at different growth stages. By using the procedure and the recommendations described in [16], researchers will be able to use CT as a reliable tool for the non-destructive reconstruction of squat crack networks and for the measurement of the crack geometries.

Both techniques can produce 3D geometries of the internal crack networks in squats. However, CT is used more frequently in this study due to the advantages that are described in [16], among them that the sample can be saved for further microstructural examinations after the nondestructive CT scanning. [16] has reported the development process of CT-technology for the rail application. Contrary to [16], we have used the results of the CT-technique in the present study for quantification purposes and calculation of the crack angles.

### 5.2.1 Definitions and conventions on the crack plane and crack angles

A 3D coordinate system (X, Y, Z) is introduced with

- X pointing in the rolling direction of the train wheels;
- Y pointing to the gauge side. Note: the left and right rails of the track have opposite Y-axes; hence, the XYZ coordinate system is not necessarily right-handed;
- Z pointing vertically and upward.

Figure 5.1 shows a schematic view of a squat crack and its intersection with the rail surface. Hereby, we define several terms regarding the crack geometry for characterizing and measuring the crack:

- Orthogonal planes: The three planes, namely, YZ, ZX, and XY (lateral-vertical, longitudinal-vertical and horizontal);
- Crack network: The entire 3D geometry of the crack. It may contain one or more crack faces;
- Crack mouth: The crack in the rail top view when the crack face is viewed at its intersection with the rail surface;
- Crack trajectory: The intersection of the crack face with the orthogonal planes;
- Crack face unit: A crack face is divided into several areas. Each such area is a crack face unit;
- Crack plane: The plane that is tangent to a crack face unit, denoted  $C_i$  ( $i = 1, \dots, 7$ );
- Crack angles  $\theta_1$ ,  $\theta_2$ , and  $\theta_3$ : The three angles at which the crack plane intersects with the three orthogonal planes, see Figure 5.1;
- Crack orientations: Four special categories of crack planes that can be identified when examining the orientation of the crack plane relative to the orthogonal planes; see Section 5.3.1.

Based on these definitions, we will be able to characterize the geometries of complex cracks. Figure 5.1(a) shows an oblique crack plane in the (X, Y, Z) coordinate system. The gauge corner side and the rolling direction of the train wheel are labeled as the GC side and RD, respectively. This oblique crack intersects the orthogonal planes with the angles  $\theta_1$ ,  $\theta_2$ , and  $\theta_3$ ; see Figure 5.1(b).

A squat crack in the very beginning stage of development can already have a curved surface, as observed in [13]. For the measurement and characterization, such a curved surface is divided into a series of surface units. The crack plane, namely, the plane that is tangent to a surface unit, intersects the orthogonal planes with the angles  $\theta_1$ ,  $\theta_2$ , and  $\theta_3$  as illustrated in Figure 5.1. These angles are the angles of the crack plane with respect to the axes X, Y and Z. The variation ranges of these angles are specified in Figure 5.1(b).

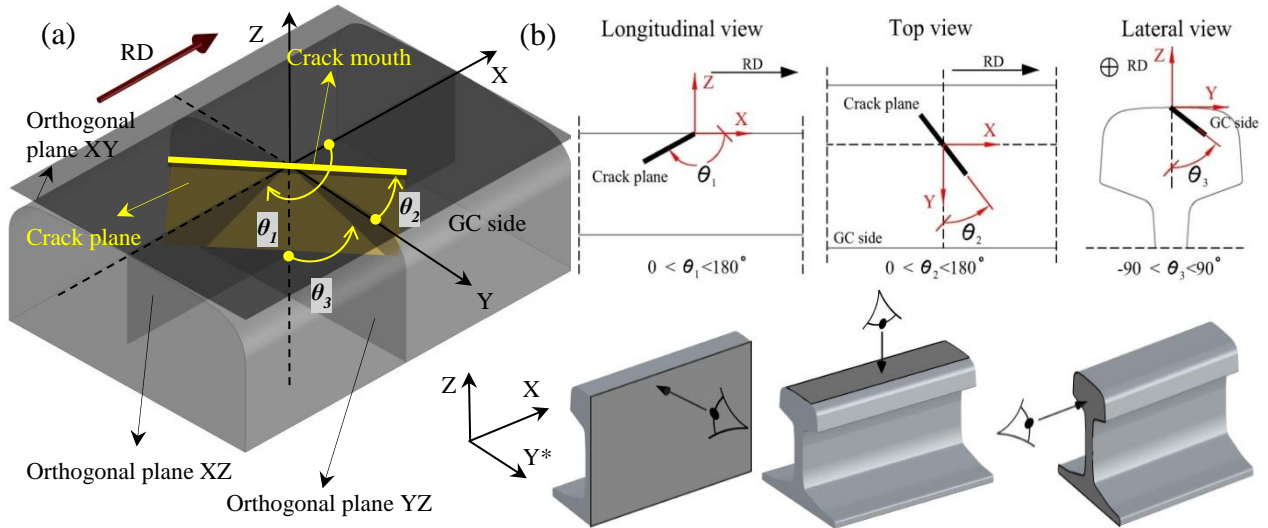


Figure 5.1. Schematic view of a squat crack plane and its intersections with the orthogonal planes: (a) A 3D view of the crack plane in the railhead, which shows the angles that are formed in the three orthogonal planes, namely, XY, XZ, and YZ; (b) The intersections of the crack planes with the three orthogonal planes at crack angles  $\theta_1$ ,  $\theta_2$ , and  $\theta_3$ ; the corresponding view of each orthogonal plane is shown in the lower part of (b). The viewing directions are marked with eye icons in (b). \* Y is the lateral axis toward the gauge corner; hence, the XYZ coordinate system is not necessarily right-handed.

### 5.2.2 Measurement of the crack angles in various squats

The 3D crack networks of the studied squats are reconstructed using serial cutting and CT scanning. The results are presented in this section and the crack angles  $\theta_1$ ,  $\theta_2$ , and  $\theta_3$  are measured.

#### 5.2.2.1 Sample-1

Details on the sample and the CT scan observations of Sample-1 are presented in Figure 5.2. Top views of the defect in the field and in the lab are shown in Figure 5.2(a) and (b), respectively. Figure 5.2(c) shows the 3D crack network of this squat that was reconstructed by CT, in which 50% transparency is applied to the gray bulk steel to highlight the internal crack face. Three examples of 2D tomographic images of the reconstructed rail object are shown in Figure 5.2(d, e, f), where the internal cracks are clearly visible in blue color. Figure 5.2(g) shows a top view of the rail sample under an optical microscope. As Sample-1 is a moderate squat with the typical two-lung appearance, the cracks have already grown both in the rail surface and in the subsurface. The crack mouths are divided into seven segments C1 – C7. With each segment a unique crack plane can be defined: the intersection of the crack plane with the rail surface is the segment. Thus we use  $C_i$  ( $i = 1, \dots, 7$ ) to denote both a segment and the uniquely associated crack plane, e.g., C1 signifies both segment C1 and crack plane C1. This applies for all the samples.

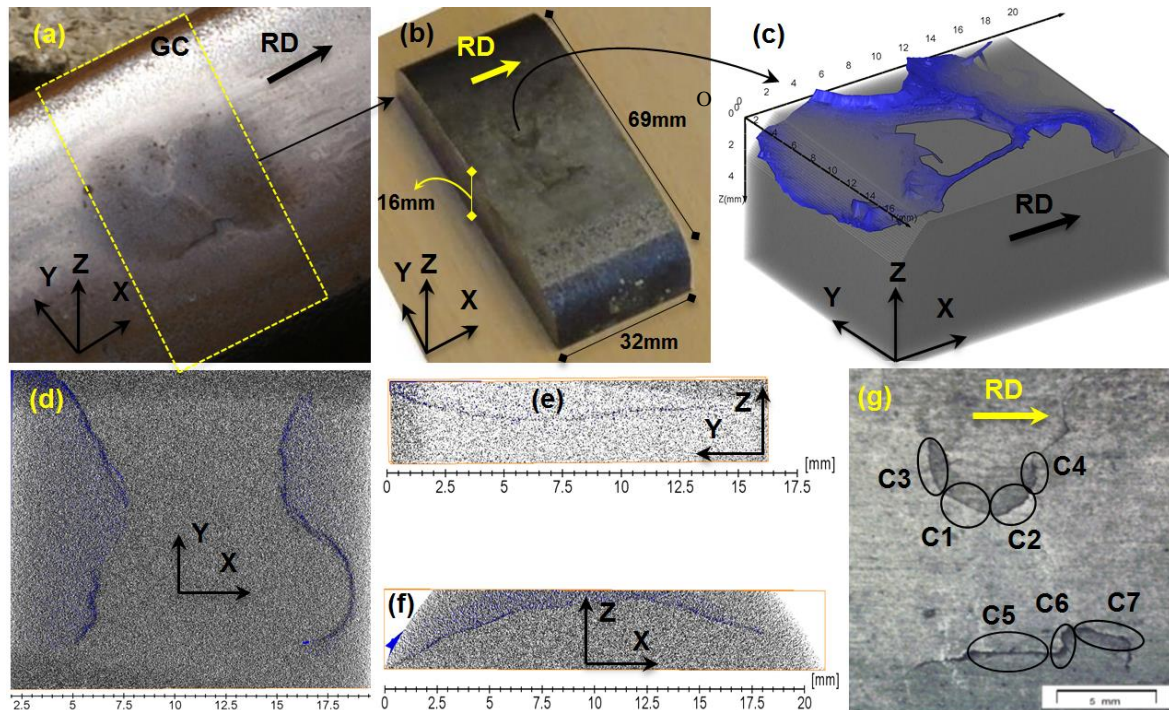


Figure 5.2. Details of the sample and the CT scan observations of Sample-1. (a) A top view of the squat when the rail was still in service; (b) the rail sample that was prepared for the CT scan; (c) a 3D visualization of the rail with its internal 3D crack network; (d, e, f) three examples of 2D tomographic images on the orthogonal planes that show the crack trajectories; (d) is a 2D image at approximately 3mm under the rail surface; (e) is approximately 15mm away from the origin of the coordinate system O; (f) is approximately 4mm away from the origin of the coordinate system O, see [16] for details about the location of 2D tomographic images in the rail bulk and (g) the rail surface with the crack mouths divided into seven segments that correspond to seven crack planes (C1–7) that the intersect the rail surface; C<sub>i</sub> s ( $i = 1, \dots, 7$ ) are shown next to the crack mouths because adding 3D crack planes into the existing rail picture is not possible.

The crack angles are measured for crack planes C1–C7. The results of the crack angle measurements including the 3D geometry of the internal cracks of all the rail samples are provided in Appendix 5.1. The results of crack angle measurements for all the rail samples are summarized at the end of Section 5.2.

### 5.2.2.2 Sample-2

Sample-2 is examined via serial cutting for reconstructing the internal crack networks. Details of the sample and the metallographic observations are presented in Figure 5.3. Figure 5.3(a) shows the moderate squat when the rail was still in service. A rectangular block of size 14×15×10 mm, which consists of seven sequential thin slices, is prepared from the railhead; see Figure 5.3(b, c). The direction of cutting is perpendicular to the direction of traffic and the slice thickness is 2 mm. The seven slices are ground and polished for the metallographic observations. Then, the cracks are observed under an optical microscope. The geometry of the cracks in each slice is examined and the crack tip locations, angles, sizes and depth are measured. In addition to the lateral sections (T1–T7), two longitudinal sections (L1, L2) are observed under the microscope. The results of metallographic observations on L1 and L2 are shown in Figure 5.3(d, e), and Figure 5.3(f) shows the corresponding results on T1–T7. Figure 5.3(g) shows the crack segments in the rail surface, where four crack planes (C1–C4) are defined. The crack trajectories of 2D slices T1–T7, L1, and L2 are combined with interpolation to generate 3D data on the internal crack network.

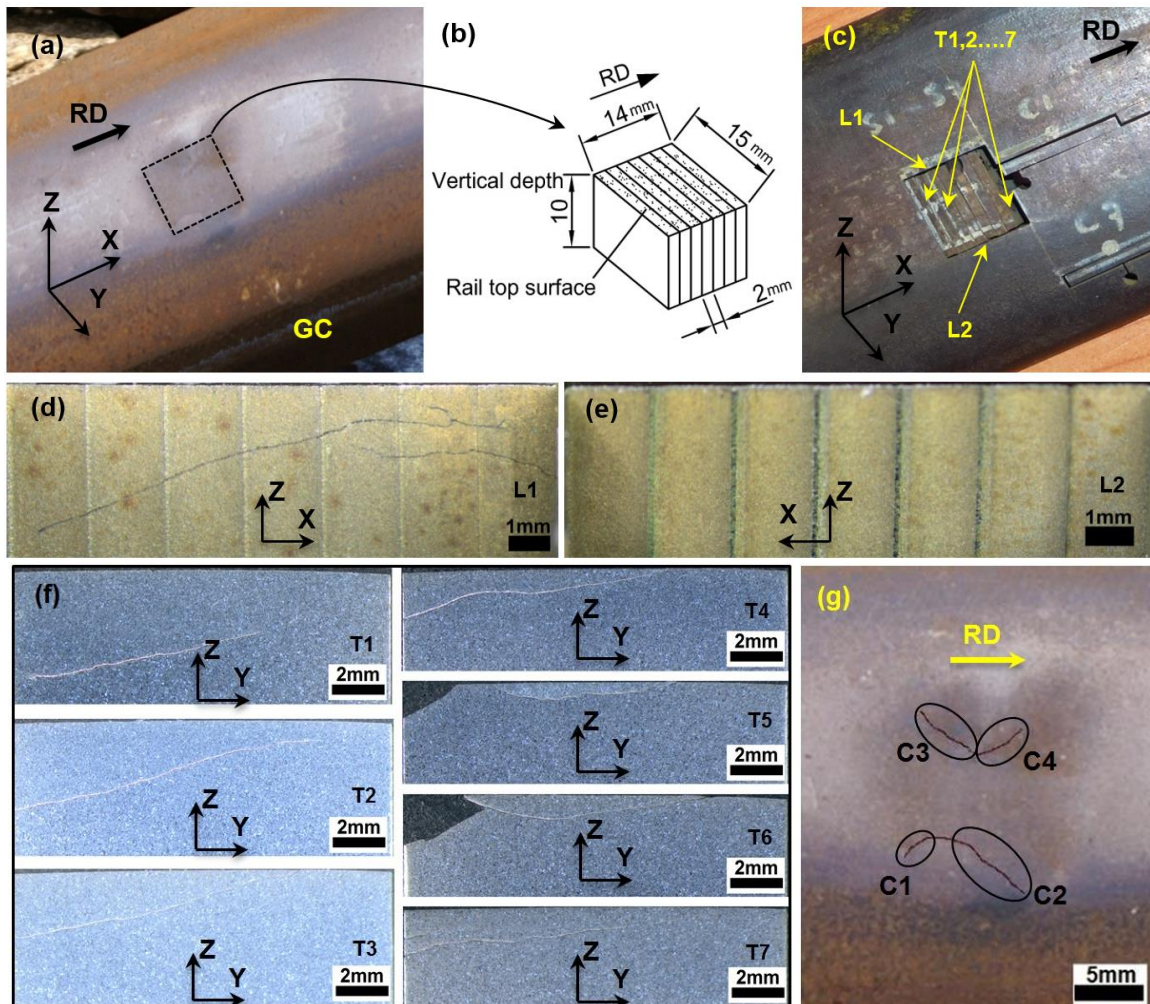


Figure 5.3. Details of the sample and the metallographic observations of Sample-2. (a) A top view of the squat when the rail was still in service; (b) the rail cutting pattern and dimensions of the sectioned slices; (c) seven slices after the cutting, lateral sections T1–T7 and longitudinal sections L1 and L2; locations of L1 and L2 are shown in (c); (d, e) metallographic observation of the cracks in the two longitudinal sections, namely, L1 and L2; (f) metallographic observations on the lateral sections, namely, T1–T7, locations of T1–T7 are shown in (c); and (g) the crack segments in the rail surface that correspond to crack planes C1–C4.

### 5.2.2.3 Sample-3

Details on the sample and the CT scan observations of Sample-3 are presented in Figure 5.4. The development process and the shape of this squat are discussed in [13]. Top views of the rail when it was still in the field and the prepared CT sample are shown in Figure 5.4(a, b). Figure 5.4(c) shows the 3D geometry of the internal crack networks in this squat and examples of 2D topographic images are shown in Figures 5.4(d, e, f). For this squat, five crack segments are considered in the rail surface, as shown in Figure 5.4(g).

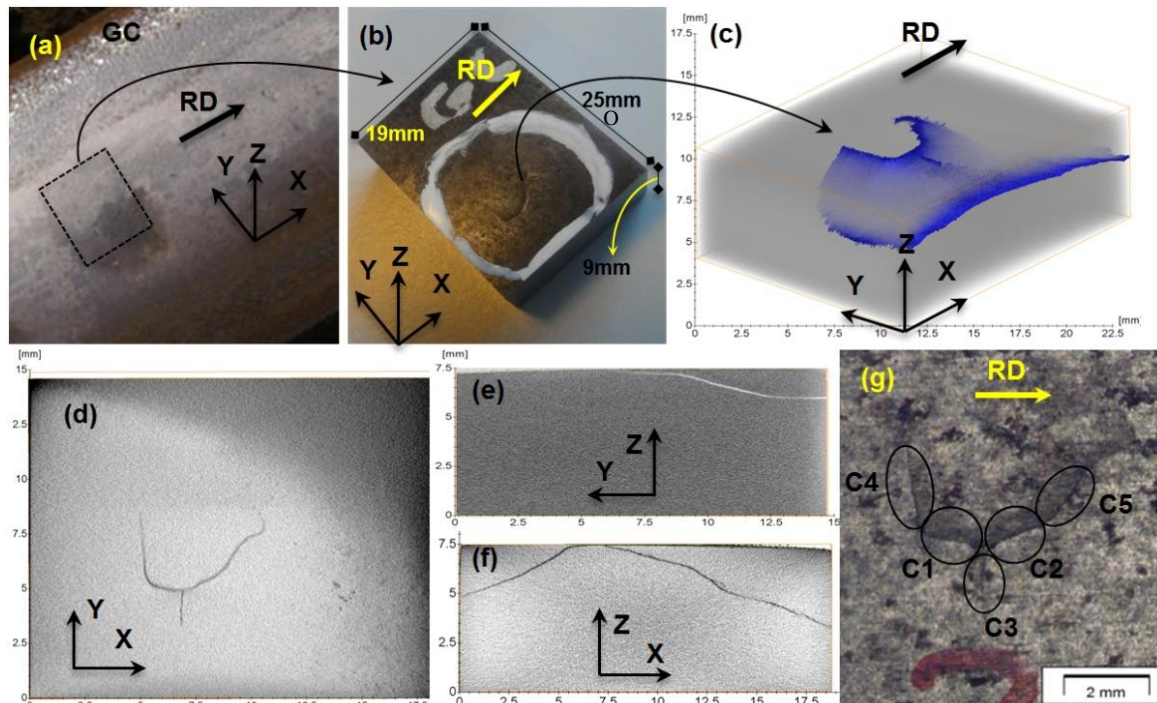


Figure 5.4. Details on the sample and the CT scan observations of Sample-3. (a) A top view of the squat when the rail was still in service; (b) the rail sample that was prepared for the CT scan; (c) a 3D visualization of the rail with the internal 3D crack network; (d, e, f) three examples of 2D tomographic images on orthogonal planes that show the crack trajectories; (d) is a 2D image at approximately 1mm under the rail surface; (e) is approximately 7 mm away from O; (f) is approximately 10 mm away from O, see [16] for details about the location of 2D tomographic images in the rail bulk and (g) a metallographic view of the rail surface with five crack segments as the intersections of the squat crack planes with the rail surface

#### 5.2.2.4 Sample-4

Details on the sample and the CT scan observations are presented in Figure 5.5. Figures 5(a, b) show top views of the rail in the field and the corresponding CT sample. Figure 5.5(c) shows the 3D crack network that is reconstructed for this squat and examples of 2D tomographic images are shown in Figures 5(d, e, f). For this squat, four crack segments (C1–C4) are considered in the rail surface, as shown in Figure 5.5(g).



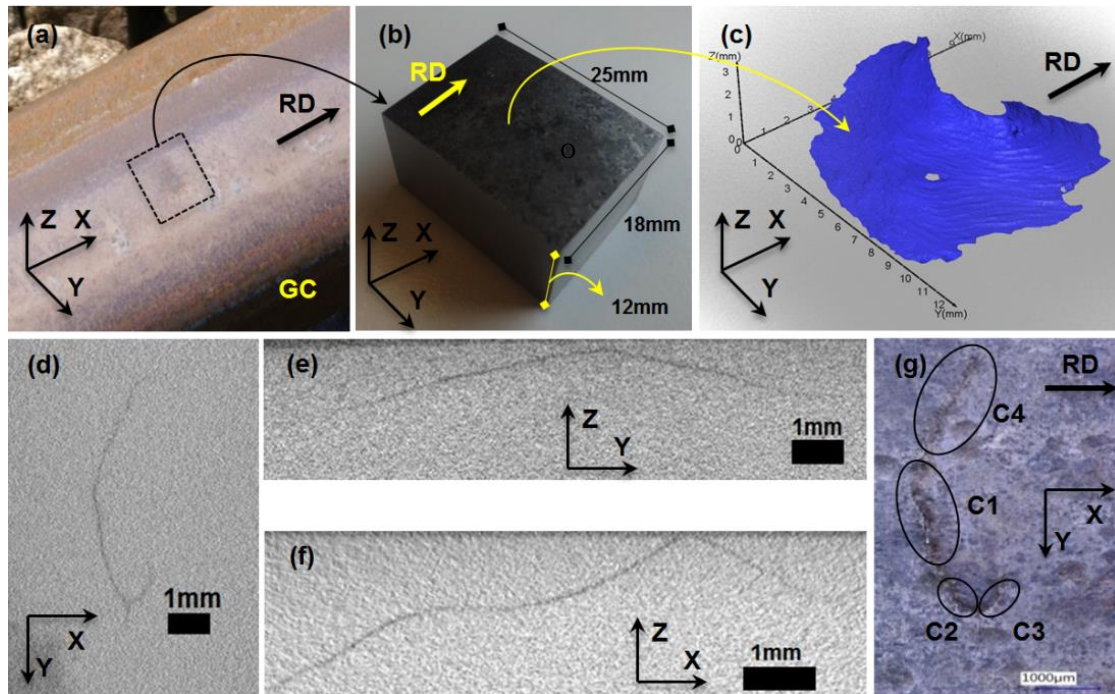


Figure 5.5. Details on the sample and the CT scan observations of Sample-4; (a) A top view of the squat defect when the rail was still in service; (b) the rail sample that was prepared for the CT scan; (c) a 3D visualization of the rail with the internal 3D crack surface; (d, e, f) three examples of 2D sections on orthogonal planes that show the crack trajectories; (d) is a 2D image at approximately 0.5 mm under the rail surface; (e) is approximately 9 mm away from O; (f) is approximately 13 mm away from O, see [16] for details about the location of 2D tomographic images in the rail bulk and (g) a metallographic view of the rail surface with four crack segments as the intersections of the crack planes with the rail surface

#### 5.2.2.5 Sample-5

The last defect (Sample-5) is not visible to the naked eye; however, we predicted the occurrence of initiating RCF cracks in the chosen area. We suspected that this place could have RCF cracks in an early stage of development since squats and corrugation were found nearby; one of the squats was Sample-4.

A rectangular block is obtained from the railhead next to Sample-4; see Figures 6(a, b). In the beginning, we inspected a length of approximately 120 mm around Sample-4 under the optical microscope and the choice on the block of Sample-5 (Figure 5.6(b)) was made when we were sure of the presence of cracks in the area. Figure 5.6(d) shows the sample under an optical microscope with the resolution of 20x. No cracks are visible at this resolution. Performing CT on the sample of Figure 5.6(b) also provided no information on the cracks in the bulk steel.

Then, this sample is cut smaller (Figure 5.6(c)) to generate CT results of higher resolution; see the discussion on the sample size in [16]. A high-resolution optical microscope (500x) is used to inspect the surface of the new sample. This time, two tiny cracks (size of approximately 80  $\mu\text{m}$ ) are found; see Figure 5.6(e). These surface cracks are observed in the longitudinal orthogonal plane (XZ), as shown in Figure 5.6(f). The CT scan on the new sample provided data on the 3D geometry of these cracks; they are presented in Figures 5.6(g, h). Three examples of 2D tomographic images are presented in Figure 5.6(g). Figure 5.6(h) presents the 3D geometries of these two cracks (C1 and C2). This observation cannot confirm that the tiny cracks in Sample-5 will further develop into a squat, as they might disappear due to, e.g., natural wear or spalling.

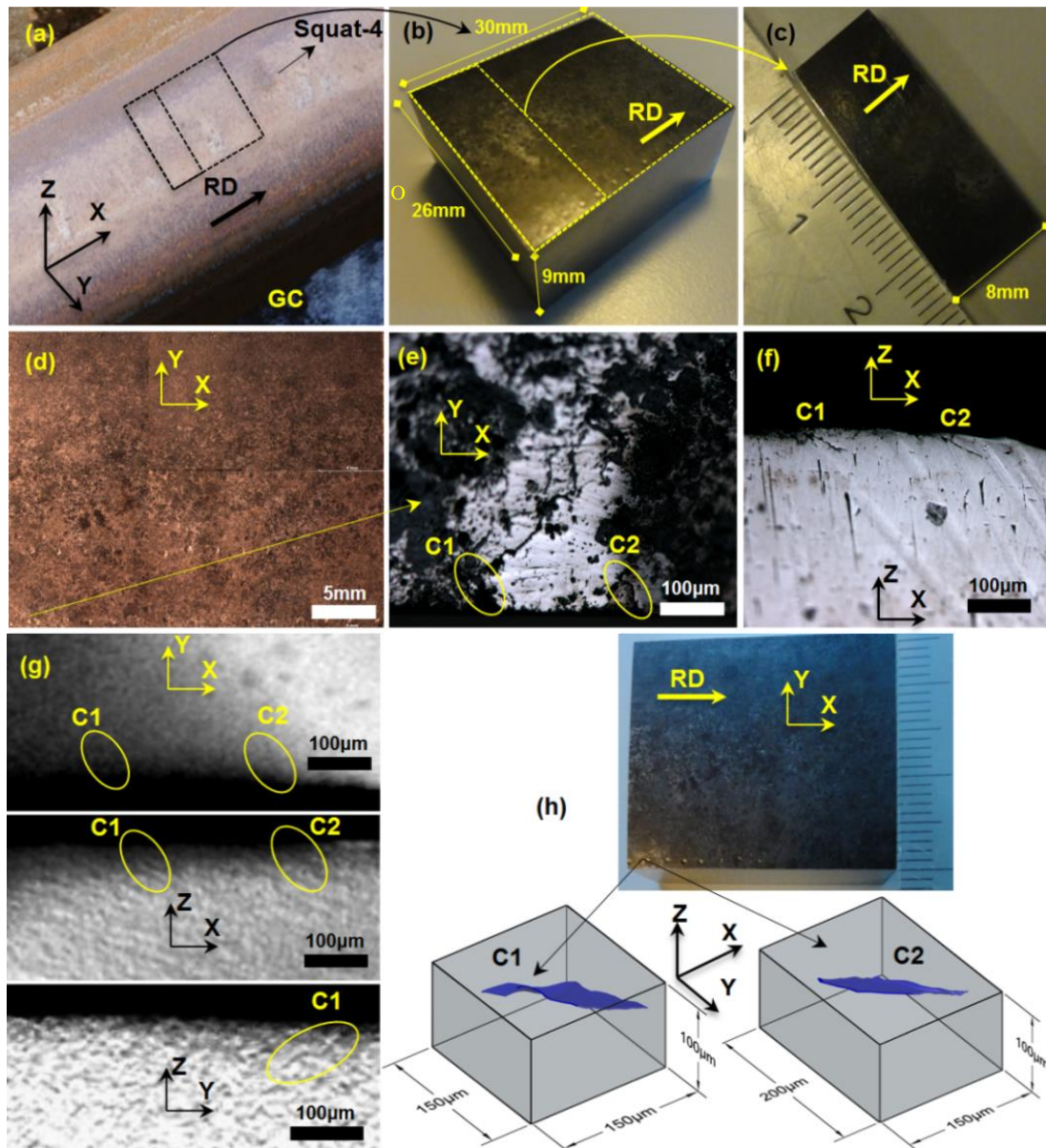


Figure 5.6. Reconstruction of the two tiny cracks in Sample-5. (a) A top view of the rail when the rail was still in service; (b, c) two rail samples that were prepared for the CT scan; (d) the large sample of (b) under the microscope at 20x resolution; (e) a microscopic view of the rail sample with two tiny cracks at 500x resolution; (f) the same cracks in the longitudinal orthogonal plane; (g) three examples of the 2D tomographic images from the CT scan; XY image is a 2D image at approximately 0.1 mm under the rail surface; (e) XZ image is approximately 2 mm away from O; YZ image is approximately 2 mm away from O and (h) 3D visualization of the rail with internal cracks C1 and C2

Table 5.2 summarizes the crack angles of the crack planes in all the rail samples. Detailed discussions on the characteristic angle ranges are provided in Section Discussion.

Table 5.2: Results of measuring the crack angles for the crack planes that intersect the rail surface per rail sample

Sample-1							
Crack plane:	C1	C2	C3	C4	C5	C6	C7
$\theta_1$	171°	13°	155°	17°	174°	93°	16°
$\theta_2$	67°	122°	28°	150°	89°	176°	79°
$\theta_3$	70°	70°	76°	80°	81°	-53°	-56°
Sample-2							
Crack plane:	C1	C2	C3	C4			
$\theta_1$	167°	14°	168°	13°			
$\theta_2$	59°	112°	124°	53°			
$\theta_3$	69°	58°	-73°	-73°			
Sample-3							
Crack plane:	C1	C2	C3	C4	C5		
$\theta_1$	141°	12°	71°	132°	28°		
$\theta_2$	79°	114°	177°	6°	147°		
$\theta_3$	77°	64°	81°	83°	71°		
Sample-4							
Crack plane:	C1	C2	C3	C4			
$\theta_1$	139°	150°	19°	262°			
$\theta_2$	10°	36°	127°	155°			
$\theta_3$	81°	67°	65°	-73°			
Sample-5							
Crack plane:	C1	C2					
$\theta_1$	17°	23°					
$\theta_2$	58°	41°					
$\theta_3$	-63°	-69°					

### 5.3 Calculation of crack angles by numerical modelling

The experimental observations made in this research are phenomena related to the fracture mechanical behaviour of the rails in RCF conditions. To understand the observations, a finite element model of the wheel-track system is employed for a preliminary numerical analysis of the RCF angles in an attempt to correlate the stress state to the cracks. The FE model and the crack initiation mechanism (based on the stress states) cannot necessarily distinguish between the types of the RCF (e.g., between squat and head check [22], whose crack angles can be similar); therefore, we use the general term “RCF crack” in the numerical part.

Contact mechanics and multi-axial fatigue analysis are used to study the crack initiation stress state in rails. Various loading conditions are modelled. Employing the critical plane concept [23], the rail elements with the highest potential for crack initiation are determined, based on which, the 3D geometry of the potential RCF cracks are estimated. The results of the crack angles are then presented.

#### 5.3.1 Finite element modelling

The finite element model of the wheel-track system considers a single wheel running over a length of a straight railway track; see Figure 5.7(a). The standard rail profile UIC 54E1 with an inclination of 1:40 at the rail foot is used. By employing an adaptive meshing method, the smallest element size in the wheel-rail contact interface is 0.4mm. The contact surfaces of

both the wheel and rail are smooth. The sprung mass of the vehicle, which together with the unsprung wheel mass form the wheel loads, is lumped and supported by a group of springs and dampers of the primary suspension. The track system is modelled of the typical ballasted railway track, in which, the rail is resting on sleepers with in-between spring/dampers serving as the fasteners. The sleepers are laid on the underlying spring/dampers as the ballast.

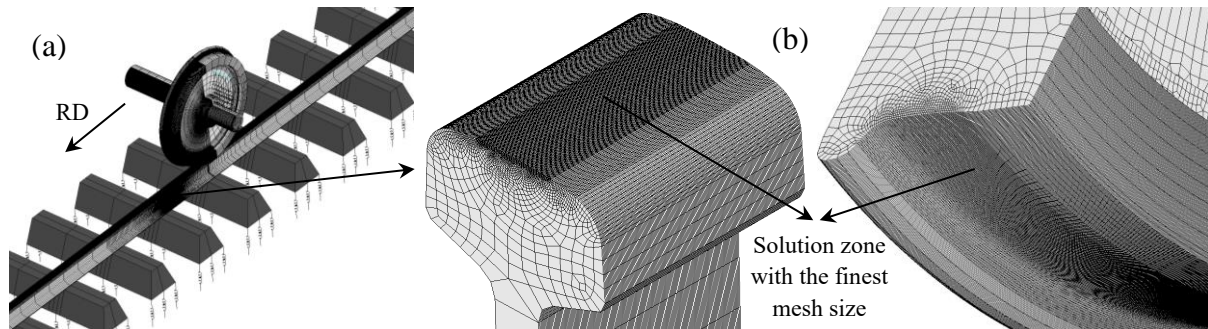


Figure 5.7. (a) 3D finite element model of the wheel–track system; (b) magnified view of the rail surface and the wheel tread with the finest mesh arrangement in the solution zone

A time–domain finite element analysis with the explicit algorithm is employed using the approach described in [15, 18]. The parameters of the finite element model are listed in Table 5.3. The materials in the contact interface are considered elastic–plastic with the properties given in Table 5.3.

Table 5.3: The values of parameters used in the numerical simulations

Parameters (unit)	Values	Parameters (unit)	Values
Static wheel load, $M_c$ (kN)	116.8	Stiffness of primary suspension, $K_c$ (kN/m)	880
Wheel weight, $M_w$ (kg)	900	Damping of primary suspension, $C_c$ (N.s/m)	4000
Wheel diameter (mm)	920	Young's modulus of wheel–rail material, $E_r$ (GPa)	210
Rail weight per length (Kg/m)	54.42	Poisson's ratio of wheel–rail material, $\nu_r$	0.3
Sleeper mass, $M_s$ (kg)	280	Density of wheel–rail material, $\rho_r$ (kg/m <sup>3</sup> )	7800
Friction coefficient, $f$	0.5	Yield stress of the work hardened rail (MPa)	800
Longitudinal traction coefficient, $\mu_x$	–0.35, 0, 0.35	Tangent modulus of elastic–plastic rail, $E_p$ (GPa)	21
Rolling speed, $V$ (km/h)	100	Young's modulus of concrete material, $E_c$ (GPa)	38.4
Stiffness of ballast, $K_b$ (kN/m)	45000	Poisson's ratio of concrete sleeper material, $\nu_c$	0.2
Damping of ballast, $C_b$ (N.s/m)	32000	Density of sleeper material, $\rho_c$ (kg/m <sup>3</sup> )	2520
Stiffness of rail pad, $K_p$ (kN/m)	1300000	Constant $J$ in the fatigue criterion	0.2
Damping of rail pad, $C_p$ (N.s/m)	45000		

Different values of the traction coefficient ( $\mu$ ) are used to simulate the braking and traction behaviour of the train wheel. The positive value ( $\mu=0.35$ ) represents the tractive wheel, while the negative ( $\mu=-0.35$ ) simulates braking. The case  $\mu=0$  simulates free rolling contact of the wheel over the rail.

### 5.3.2 Fatigue initiation criteria

Up to now, various fatigue criteria have been employed to quantify fatigue initiation life of materials, mostly by using calculated stresses and strains out of numerical models. Some critical reviews on different predictive models of fatigue crack initiation in engineering materials including metals are provided in [19, 20]. Wheels and rails are subjected to a non–proportional multiaxial stress condition, which causes variation in the directions of the principal stresses and the maximum shear stresses. Therefore, a multiaxial fatigue criterion that could consider the non–proportional loading condition is more applicable [21].

In the current research, we used the multiaxial fatigue model proposed by Jiang and Sehitoglu [23] for the fatigue initiation analysis. This fatigue criterion is used for the wheel–rail contact application in [21] and the fatigue predictions by using that have been reported to

be in good agreement with the test results and field observations [21]. This criterion has also been used in [24] for predicting fatigue initiation life of the rail under RCF conditions, in which, reasonable correlations with laboratory test data and field observations were seen. The fatigue parameter in this model is expressed by [23]:

$$FP_{\max} = \left( \langle \sigma^{\max} \rangle \frac{\Delta \varepsilon}{2} + J \Delta \tau \Delta \gamma \right)_{\max} \quad 5.1$$

where, in each loading cycle,  $\Delta \varepsilon$  is the normal strain range,  $\sigma_{\max}$  the maximum normal stress,  $\Delta \gamma$  the shear strain range,  $\Delta \tau$  the shear stress range,  $J$  a material-dependent constant and  $\langle \rangle$  the McCauley bracket  $\langle x \rangle = (|x| + x)/2$ . This model considers the influence of normal and shear loadings on damage occurrence. The first term of this equation considers the mean stress effect in the normal direction, while the second term incorporates the shear stress–strain effects. The stress–strain responses, needed for this equation, are obtained from the finite element analysis.

According to [23], the stress and strain responses in 5.1 need to be obtained at the critical plane, in which, the largest fatigue parameter ( $FP_{\max}$ ) occurs. The critical plane approach searches for the most potential damage plane, where, a fatigue crack tends to initiate. Any rotation in the global axes, shown in Figure 5.1(a), leads to a new fatigue parameter. In this approach, the fatigue parameter is calculated by inspecting all the possible plane orientations by tensor rotations. The crack initiation plane, with angles shown in Figure 5.1, corresponds to the orientation which creates the maximum fatigue parameter. The stress components when the coordinate system is subjected to a spatial rotation are shown in Figure 5.8 (a, b). As shown in Figure 5.8 (c, d) two forms of demonstrations are available for crack plane angles. Figure 5.8 (c) shows the spatial angles of the critical plane ( $\varphi_1, \varphi_2, \varphi_3$ ) with respect to the global axes. Figure 5.8 (d) shows the corresponding 2D angles ( $\theta_1, \theta_2, \theta_3$ ), formed by intersection with the orthogonal planes. These 2D planar angles are the same crack angles used for the experimental observations.

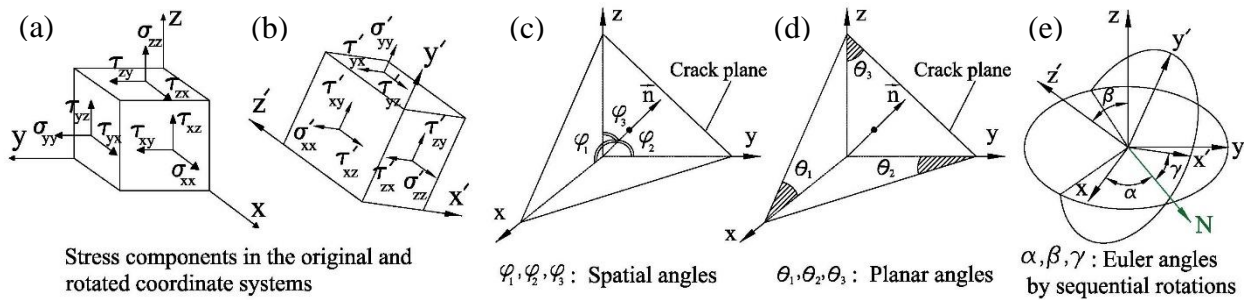


Figure 5.8. (a) Stress components of a single element in the original coordinate system; (b) stress components after spatial rotation; (c) spatial angles of the critical plane (crack initiation plane); (d) the corresponding planar angles of the crack plane; (e) Euler angles corresponding to sequential axes rotations

The relationship between the spatial angles and the 2D planar angles is written by:

$$\theta_1 = \arctan\left(-\frac{\cos \varphi_3}{\cos \varphi_1}\right), \theta_2 = \arctan\left(-\frac{\cos \varphi_1}{\cos \varphi_2}\right), \theta_3 = \arctan\left(-\frac{\cos \varphi_2}{\cos \varphi_3}\right) \quad 5.2$$

The spatial angles are related to each other by the spherical law of cosines:

$$\cos^2 \varphi_1 + \cos^2 \varphi_2 + \cos^2 \varphi_3 = 1 \quad 5.3$$

and the 2D planar angles are related by:

$$\tan \theta_1 \cdot \tan \theta_2 \cdot \tan \theta_3 = 1 \quad 5.4$$

which means, if two of the 2D angles are known, the third angle can be calculated. The planar angles are calculated in this research, which complies with the experimental observations.

When a Cartesian coordinate system XYZ (the original state, in which the stresses are obtained) is subjected to the transformation, the transformation matrix of the stress tensor is related using:

$$\boldsymbol{\sigma} = \begin{pmatrix} \sigma_x & \tau_{xy} & \tau_{xz} \\ \tau_{xy} & \sigma_y & \tau_{yz} \\ \tau_{xz} & \tau_{yz} & \sigma_z \end{pmatrix}, \quad \boldsymbol{\sigma}' = \begin{pmatrix} \sigma'_x & \tau'_{xy} & \tau'_{xz} \\ \tau'_{xy} & \sigma'_y & \tau'_{yz} \\ \tau'_{xz} & \tau'_{yz} & \sigma'_z \end{pmatrix} \quad 5.5$$

$$\boldsymbol{\sigma}' = \mathbf{Q} \cdot \boldsymbol{\sigma} \cdot \mathbf{Q}^T, \quad \mathbf{Q} = \mathbf{Q}_z \cdot \mathbf{Q}_y \cdot \mathbf{Q}_x \quad 5.6$$

$$\mathbf{Q}_x = \begin{pmatrix} 1 & 0 & 0 \\ 0 & \cos\alpha & \sin\alpha \\ 0 & -\sin\alpha & \cos\alpha \end{pmatrix}, \quad \mathbf{Q}_y = \begin{pmatrix} \cos\beta & 0 & -\sin\beta \\ 0 & 1 & 0 \\ \sin\beta & 0 & \cos\beta \end{pmatrix}, \quad \mathbf{Q}_z = \begin{pmatrix} \cos\gamma & \sin\gamma & 0 \\ -\sin\gamma & \cos\gamma & 0 \\ 0 & 0 & 1 \end{pmatrix} \quad 5.7$$

where  $\boldsymbol{\sigma}$  is the original stress tensor,  $\boldsymbol{\sigma}'$  is the transformed stress tensor and  $\mathbf{Q}$  is the transformation matrix. The angles  $\alpha$ ,  $\beta$  and  $\gamma$  are the Euler angles (see Figure 5.8) which are connected to the spatial angles ( $\varphi_1, \varphi_2, \varphi_3$ ) using:

$$\sin\beta \cdot \cos\gamma = \cos\varphi_1, \quad \cos\alpha \cdot \sin\beta = -\cos\varphi_2, \quad \beta = \varphi_3 \quad 5.8$$

The procedure for calculating the crack angles is as follows: (i) A random time step is selected in the solution zone of the finite element model. (ii) The stress and strain components in rail elements are calculated for the chosen time step (when the wheel is running over the rail, the stresses can be calculated in the rail elements at any time step). (iii) The rail element that experienced the largest equivalent von Mises stress under the wheel passage is determined; the von Mises stress here determines the most critical material point (critical damage location, susceptible to fatigue damage and crack initiation) in the rail. (iv) Possible variations with respect to the planar angles are searched and the fatigue parameter is calculated by varying two of these angles ( $\theta_1, \theta_2$ ) from zero to  $180^\circ$ ; note that  $0 \leq \theta_1, \theta_2 \leq 180$  as shown in Figure 5.1(b). (iv) The angles, by which the highest fatigue parameter is achieved, are reported as the potential crack angles, while, their corresponding plane is considered as the crack initiation plane.

### 5.3.3 Results of numerical simulations

The time histories of stresses and strains of the wheel running over the rail are obtained from the finite element simulations and the corresponding fatigue parameters ( $FP$ ) are calculated. Figure 5.9 shows the time histories of the V–M stresses experienced by an element in the rail surface during the wheel passage.

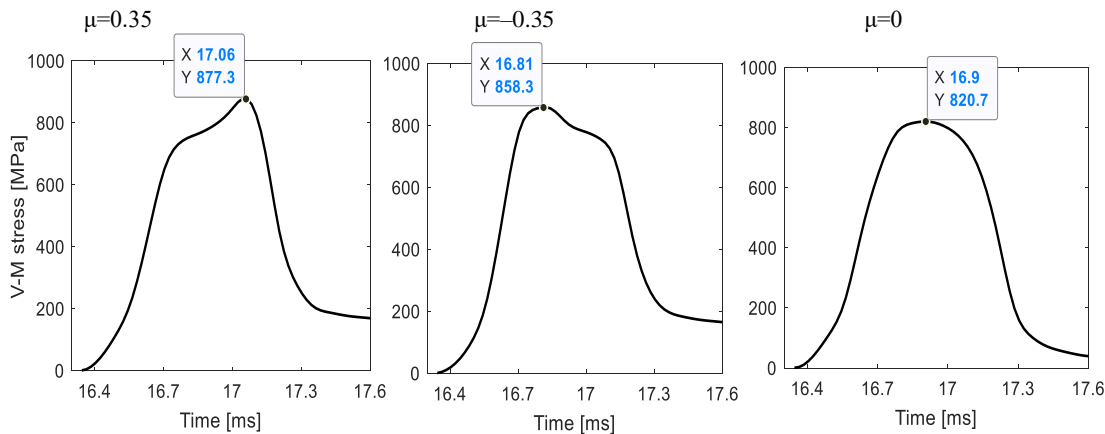


Figure 5.9. Time histories of von Mises (V–M) stresses in the rail surface during wheel passage; the results are for different traction coefficients

The stress components of the rail element when the maximum von Mises stress occur during the wheel passage are calculated (see the given times and peak stress values in Figure 5.9). The  $FP$  parameter is calculated using Equation 5.1. For the search of the critical plane, the angles  $\theta_1, \theta_2$  are varied and the corresponding (transformed) stresses and strains are determined. The values of  $FP$  with respect to these angles are calculated. Figure 5.10 shows the results of the  $FP$  for the three cases. The dimensionless  $FP$  values are calculated by normalizing the fatigue parameters over the peak value of  $FP$ ; the values of  $FP$  are indicative and we only search for the angles, by which, the peaks occur.

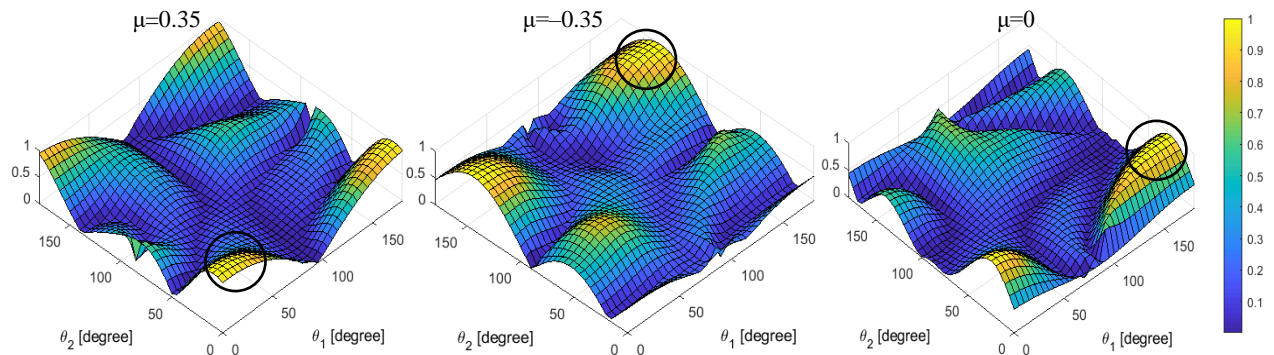


Figure 5.10. Searching for the critical plane with the maximum  $FP$  in the rail element; the higher  $FP$  (dimensionless) is shown with brighter in yellow and the lower  $FP$  with darker in blue; the black circles show the regions where the peaks occur.

Based on the  $FP$  distributions with respect to the angles, the angles of crack initiation are estimated for the element at the centre of the contact area where the pressure is the largest. They are listed in Table 5.4.

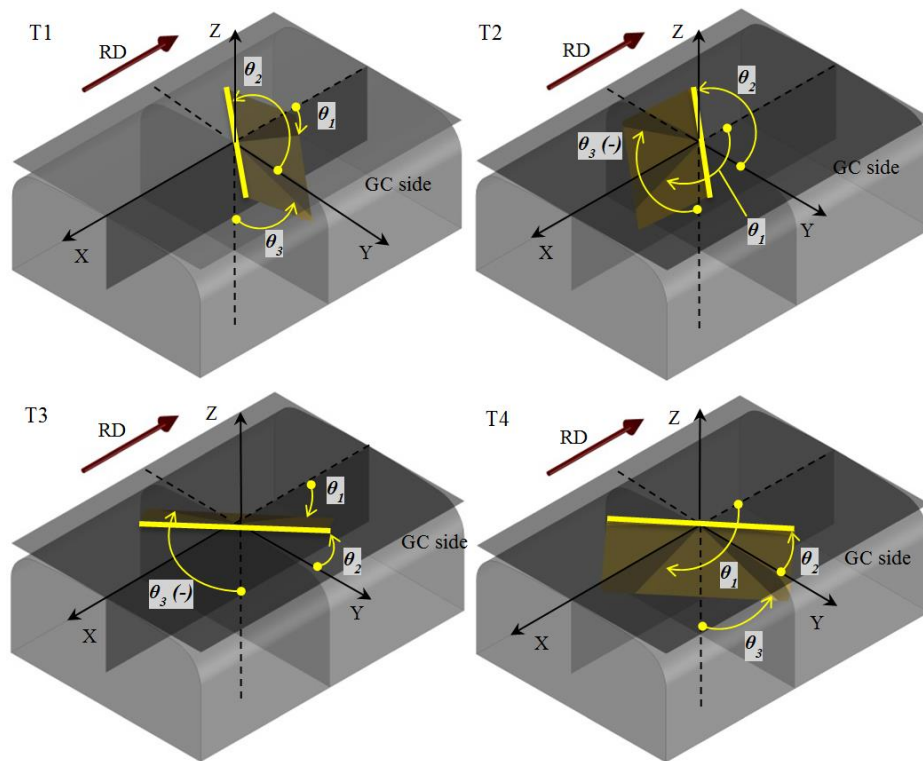
Table 5.4: Crack angles calculated by the numerical simulations

Angle	$\mu=0.35$	$\mu=-0.35$	$\mu=0$
$\theta_1$	19.8	159.9	158.6
$\theta_2$	17.6	167.3	36.9
$\theta_3$	-83.5	-85.3	73.6

## 5.4 Discussion

### 5.4.1 Categorization of the crack planes into orientations

The crack planes that intersect the rail surface have been measured and their crack angles distribute over a wide range. In this section, four crack orientations are identified to better categorize and characterize the cracks. These 4 types of orientations, namely, T1 – T4, are illustrated in Figure 5.11 in terms of their relative positions and the corresponding angles  $\theta_1$ ,  $\theta_2$ , and  $\theta_3$ . The nominal variation ranges of the angles that correspond to each category are specified at the bottom of this figure. All the crack planes that were measured for the five samples in this research are classified in Table 5.5 according to the orientation categories.



Nominal variation ranges of  $\theta_1$ ,  $\theta_2$ , and  $\theta_3$  for the identified categories:

Orientation category	T1	T2	T3	T4
Angle range $\theta_1$	$0^\circ < \theta_1 < 90^\circ$	$90^\circ < \theta_1 < 180^\circ$	$0^\circ < \theta_1 < 90^\circ$	$90^\circ < \theta_1 < 180^\circ$
Angle range $\theta_2$	$90^\circ < \theta_2 < 180^\circ$	$90^\circ < \theta_2 < 180^\circ$	$0^\circ < \theta_2 < 90^\circ$	$0^\circ < \theta_2 < 90^\circ$
Angle range $\theta_3$	$0^\circ < \theta_3 < 90^\circ$	$-90^\circ < \theta_3 < 0^\circ$	$-90^\circ < \theta_3 < 0^\circ$	$0^\circ < \theta_3 < 90^\circ$

Figure 5.11. Four orientations (T1–T4) of the crack planes that intersect the rail surface

The proposed crack types (T1–T4) in Figure 5.11 are in fact all possible situations, where, a crack plane in the railhead can be located by looking at the defined angle variations in the lower part of Figure 5.11.

Table 5.5: Categorization of the crack planes that intersect the rail surface into 4 orientations

Sample–	Crack plane	C1	C2	C3	C4	C5	C6	C7
1	Orientation category	T4	T1	T4	T1	T4	T2	T3
2	Crack plane	C1	C2	C3	C4			
	Orientation category	T4	T1	T2	T3			
3	Crack plane	C1	C2	C3	C4	C5		
	Orientation category	T4	T1	T1	T4	T1		
4	Crack plane	C1	C2	C3	C4			
	Orientation category	T4	T4	T1	T2			
5	Crack plane	C1	C2					
	Orientation category	T3	T3					

Table 5.6 lists the occurrence frequencies of all the crack orientations in the 5 samples. T4 is the most prominent (40%), followed by T1 (30%). T3 and T2 are less frequent with occurrence percentages of 20% and 10%, respectively.

After classifying the crack orientations into the four categories, the variation ranges of the crack angles are calculated; see Table 5.6. Crack planes C3 in Sample–3 and C6 in Sample–1 are excluded from the results in Table 5.6, as their corresponding angles deviate substantially from the orientation ranges that were obtained for the other crack planes. Possible explanations for such deviations are that these crack planes are probably not the primary



cracks (C3 of Sample–3) or they are due to local disturbances (C6 of Sample–1). The symbol “(–)” in Table 5.6 indicates that  $\theta_3$  is negative for orientations T2 and T3.

Table 5.6: Occurrence frequency of each crack orientation category and the variation ranges of  $\theta_1$ ,  $\theta_2$ , and  $\theta_3$

Crack orientation category	T1	T2	T3	T4	Total
Occurrence frequency	6	2	4	8	20
Occurrence percentage	30%	10%	20%	40%	100%
Angle range $\theta_1$	12°–28°	154°–168°	13°–23°	132°–150°	–
Angle range $\theta_2$	112°–150°	124°–155°	41°–79°	6°–36°	–
Angle range $\theta_3$	58°–80°	73°–77° (–)	56°–73° (–)	67°–81°	–

The ranges of the orientation angles are plotted in Figure 5.12 with the view angles specified on the top. The ranges of T4, which is the most prevalent crack orientation, are plotted in Figure 5.12(d).

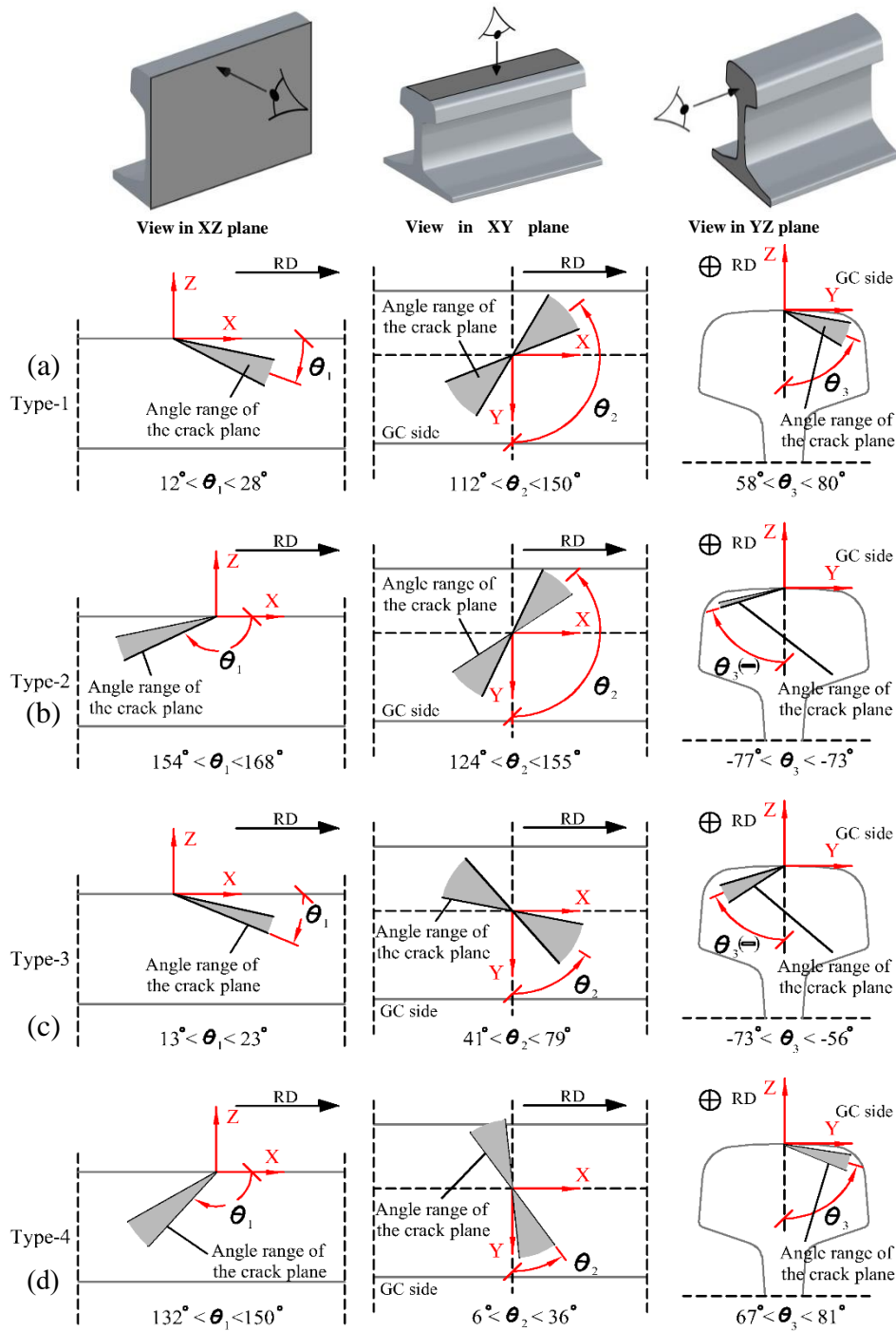


Figure 5.12. Ranges of the four crack orientations

#### 5.4.2 Order of crack initiation in multiple cracks

The crack plane is defined as the plane that is tangent to a crack face unit (Section 5.2.1). Such a definition applies to the cracks in their initiation phase. Because we are not sure which planar face happens earlier in a grown squat, we have studied all the possibilities and calculated all the corresponding angles. The planar faces of the cracks can meet each other and create V-shape or more complex cracks, even in the early stage of crack development. Characterization of such complex cracks seems only possible by discretising them into the planar units as suggested in this study. In this section we discuss the development of cracks.

Squat cracks are reported to initiate from the rail surface; see, e.g., [5] and [13]. The cracks of Sample-5 would support this if they would grow into a squat. The cracks of the other 4 samples are deep and it is not possible to determine their initiation locations from the data that are available. If the 4 orientations, namely, T1 – T4, are ordered according to descending frequency of occurrence as shown in Figures 5.13 (i, j, k, l), then T4 and T1, which represent two crack planes, will together form a V-shaped peninsula with a V-shaped crack mouth; see Figure 5.13(j) for an idealization and Figure 5.13(g) for a real case. In practice, the tip of V may be rounded to become a U, so that the crack mouth appears U-shaped; see Figure 5.13(f) for a typical example. Then, T2 and T3 will together form another V-shaped (or U-shaped) peninsula, although much more obtuse. The tips of the two V-shaped peninsulas face each other. Since T4 and T1 have a much higher joint occurrence (70%) than T2 and T3 (30%), it is reasonable to conclude that the peninsula that is formed by T4 and T1 appeared earlier than that by T2 and T3. Thus, the crack that was formed by T4 and T1 is the primary crack and the crack by T2 and T3 the secondary. When a squat develops further in its growth process, the crack network becomes larger and more complex, and additional crack mouths appear in the rail surface. According to these results and Figure 5.13, the primary cracks of Sample-1, Sample-3 and Sample-4 are on the gauge side and that of Sample-2 is on the field side. These findings accord with the angle predictions by other researchers, e.g., [8], [11] and [13]. As was concluded from the extensive field monitoring observations of [13], most of the primary cracks started on the gauge side with U-shaped peninsula-like crack faces.

The initiating primary crack in [13] had an angle of approximately  $20^\circ$  with the rail surface; the crack propagated into the rail toward the field side at an angle of approximately  $20^\circ$ ; see  $\alpha$  in Figure 5.7(c) of [13]. Using the methodology that is proposed in this study, we can approximate such a U-shaped peninsula-like crack face with two main crack orientation planes (T4 and T1). The angle of  $\alpha = 20^\circ$  is found to accord with the measured angles of the two crack orientation planes in this study, namely,  $\theta_I$  is  $12^\circ$ – $28^\circ$  for T1 and  $132^\circ$ – $150^\circ$  for T4; see Figure 5.12.

#### 5.4.3 Numerical results compared to measured crack angles

In Table 5.7, the crack angles are compared between the experimental (Table 5.6) and the FE results (Table 5.4). Among the four crack types seen from the experimental observations (T1–T4), 3 crack types (T2, T3 and T4) were observed from the FE modelling, for  $\mu = -0.35$ ,  $0.35$  and  $0$ , respectively; crack type T1 was not seen. This indicates that the crack angles should probably depend on the loading conditions, although the precise loading conditions of the analysed samples are impossible to trace back. According to the results of T2, T3 and T4, it can be seen that the crack angles calculated by the FE modelling are in reasonable agreement with the experiment observation.

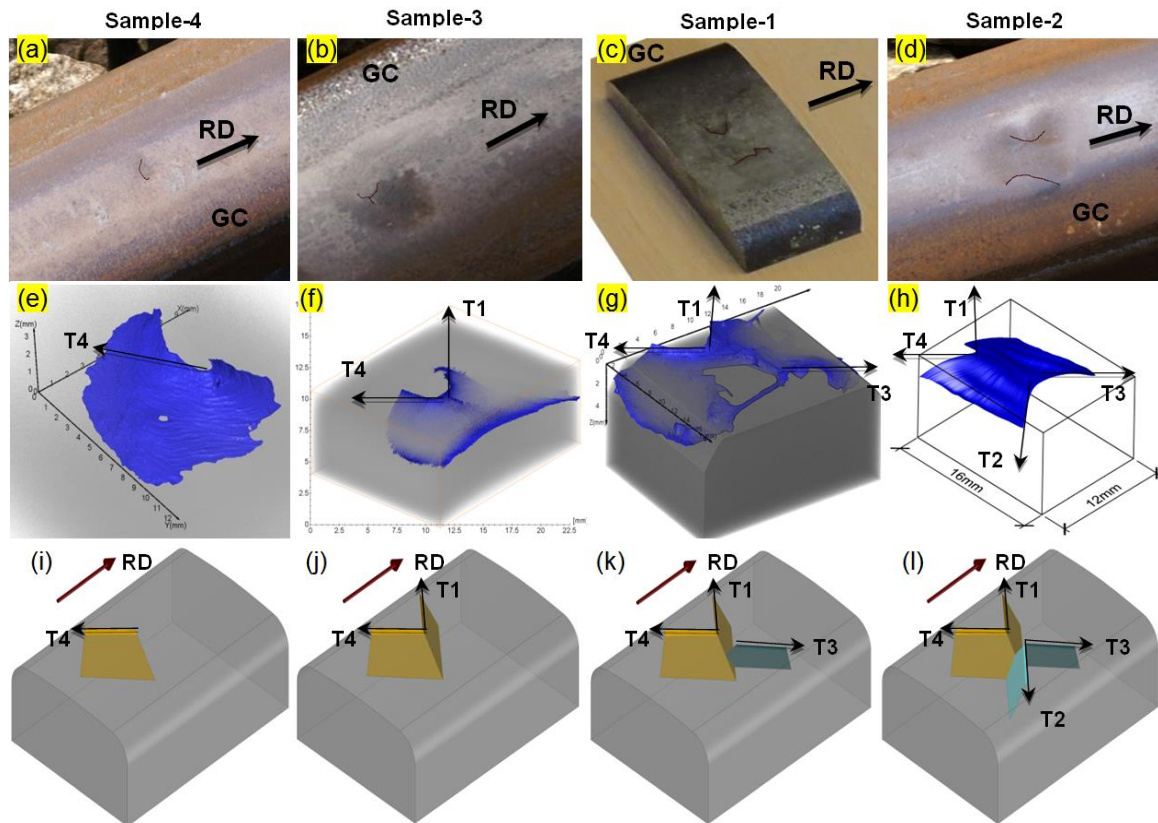


Figure 5.13. Four squats (Samples 1–4) with characteristic V-shaped (or U-shaped) peninsula-like crack faces. (a, b, c, d) Top views with the crack mouths highlighted; (e, f, g, h) the reconstructed 3D crack networks; and (i, j, k, l) with increasing crack complexity, the cracks form the characteristic single V-shaped (Sample-3) and double V-shaped (Sample-2) peninsula-like crack faces.

Table 5.7: Comparison of the variation ranges of  $\theta_1$ ,  $\theta_2$ , and  $\theta_3$  between experiments and FE results. The data are from Tables 5.4 and 5.6.

Crack type/angle	T1		T2 $\mu=-0.35$		T3 $\mu=0.35$		T4 $\mu=0$	
	Experiments	FEM	Experiments	FEM	Experiments	FEM	Experiments	FEM
$\theta_1$	12°–28°	Not seen.	154°–168°	159.9	13°–23°	19.8	132°–150°	158.6
$\theta_2$	112°–150°	Not seen.	124°–155°	167.3	41°–79°	17.6	6°–36°	36.9
$\theta_3$	58°–80°	Not seen.	73°–77° (-)	-85.3	56°–73° (-)	-83.5	67°–81°	73.6

The angle ranges  $\theta_1$ ,  $\theta_2$ , and  $\theta_3$  in Table 5.7 (experimental part) are obtained from the observations on the five squats and cannot be generalized to all squats; however, the other facts mentioned in Discussion support the validity of the results obtained i.e. 1) agreement with the angle predictions by other researchers in the literature and 2) reasonable agreement with the numerical results. The facts mentioned aid in concluding that the crack units of the squat defects appear to form within the ranges indicated in this study.

## 5.5 Conclusions

By defining crack planes, this study measured the angles of squat cracks that intersected the rail surface and identified the characteristic orientations of the cracks. CT scanning and metallographic observations were used to reconstruct the complex geometries of crack networks in squats of various severities. Finite element modelling is employed to relate the stress state to the crack angles. The following conclusions were drawn:

- 1) Using the proposed 3D visualization method, including the definitions of crack planes and angles, we were able to define and measure the 3D geometries of squats with complex crack networks. The method was successfully applied to squat defects of various severities.
- 2) Four crack orientations, namely, T1–T4, were identified and visually demonstrated.
- 3) The ranges of the characteristic crack angles of the four orientations were measured for 5 samples. The cracks have an angle of  $132^{\circ}$ – $150^{\circ}$  relative to the  $X$ -axis ( $\theta_1$ ). The angle in the rail surface relative to the  $Y$ -axis ( $\theta_2$ ) was in the range of  $6^{\circ}$ – $36^{\circ}$ . In the rail vertical–longitudinal cross–section, the angle of the crack relative to the  $Z$ -axis ( $\theta_3$ ) was in the range of  $67^{\circ}$ – $81^{\circ}$ . These findings accorded with angle predictions by other researchers, e.g., [8], [11], and with the field monitoring research of [13].
- 4) The occurrence frequencies of the orientations were calculated for the samples, based on which it was found that orientations T4 and T1 together form a V-shaped (or U-shaped) peninsula, which is the primary crack of squats and accords with the findings in the literature [13]. T2 and T3 together form V-shaped secondary cracks.
- 5) The crack angles calculated by the FE modeling were in agreement with the experimental observations. The angle types T2, T3 and T4 seem to correspond to braking, traction and free rolling loading, respectively. This indicates that the crack initiation angle depends on the loading conditions. Further investigation on this is needed.

## 5.6 References

- [1] Z. Li, X. Zhao, C. Esveld, R. Dollevoet & M. Molodova, An investigation into the causes of squats—correlation analysis and numerical modeling, *Wear*, 265 (2008) 1349–1355.
- [2] S. Bogdanski, M. Olzak & J. Stupnicki, Numerical modelling of a 3D rail RCF 'squat'-type crack under operating load, *Fatigue & Fracture of Engineering Materials & Structures*, 21 (1998) 923–935.
- [3] M. Farjoo, W. Daniel & P.A. Meehan, Modelling a squat form crack on a rail laid on an elastic foundation, *Engineering Fracture Mechanics*, 85 (2012) 47–58.
- [4] S. Bogdanski, M. Olzak & J. Stupnicki, Numerical stress analysis of rail rolling contact fatigue cracks, *Wear*, 191 (1996) 14–24.
- [5] S. Pal, W.J.T. Daniel & M. Farjoo, Early stages of rail squat formation and the role of a white etching layer, *International Journal of Fatigue*, 52 (2013) 144–156.
- [6] S. Simon, A. Saulot, C. Dayot, X. Quost & Y. Berthier, Tribological characterization of rail squat defects, *Wear*, 297 (2013) 926–942.
- [7] M. Naeimi, S. Li, Z. Li, J. Wu, R.H. Petrov, J. Sietsma & R. Dollevoet, Thermomechanical analysis of the wheel–rail contact using a coupled modelling procedure, *Tribology International*, 117 (2018) 250–260.
- [8] J. Ringsberg, M. Loo–Morrey, B. Josefson, A. Kapoor & J.H. Beynon, Prediction of fatigue crack initiation for rolling contact fatigue, *International Journal of Fatigue*, 22 (2000) 205–215.
- [9] X. Deng, Z. Li, Z. Qian, W. Zhai, Q. Xiao & R. Dollevoet, Pre-cracking development of weld-induced squats due to plastic deformation: five-year field monitoring and numerical analysis, *International Journal of Fatigue* 127 (2019) 431–444.
- [10] F. Franklin & A. Kapoor, Modelling wear and crack initiation in rails, *Proceedings of the Institution of Mechanical Engineers, Part F: Journal of rail and rapid transit*, 221 (2007) 23–33.

- [11] M. Akama, H. Matsuda, H. Doi & M. Tsujie, Fatigue crack initiation life prediction of rails using theory of critical distance and critical plane approach, *Journal of Computational Science and Technology*, 6 (2012) 54–69.
- [12] J. Ringsberg & B. Josefson, Finite element analyses of rolling contact fatigue crack initiation in railheads, *Proceedings of the Institution of Mechanical Engineers, Part F: Journal of Rail and Rapid Transit*, 215 (2001) 243–259.
- [13] X. Deng, Z. Qian, Z. Li & R. Dollevoet, Investigation of the formation of corrugation–induced rail squats based on extensive field monitoring, *International Journal of Fatigue*, 112 (2018) 94–105.
- [14] S. Li, J. Wu, R.H. Petrov, Z. Li, R. Dollevoet & J. Sietsma, “Brown etching layer”: A possible new insight into the crack initiation of rolling contact fatigue in rail steels?, *Engineering Failure Analysis*, 66 (2016) 8–18.
- [15] X. Deng, Z. Qian & R. Dollevoet, Lagrangian Explicit Finite Element Modeling for Spin–Rolling Contact, *Journal of Tribology*, 137 (2015) 041401–041401.
- [16] M. Naeimi, Z. Li, Z. Qian, Y. Zhou, J. Wu, R.H. Petrov, J. Sietsma & R. Dollevoet, Reconstruction of the rolling contact fatigue cracks in rails using X–ray computed tomography, *NDT & E International*, 92 (2017) 199–212.
- [17] J.E. Garnham, D.I. Fletcher, C.L. Davis & F.J. Franklin, Visualization and modelling to understand rail rolling contact fatigue cracks in three dimensions, *Proceedings of the Institution of Mechanical Engineers, Part F: Journal of Rail and Rapid Transit*, 225 (2011) 165–178.
- [18] Z. Yang, X. Deng & Z. Li, Numerical modeling of dynamic frictional rolling contact with an explicit finite element method, *Tribology International* 129 (2019) 214 – 231.
- [19] J. Das & S. Sivakumar, An evaluation of multiaxial fatigue life assessment methods for engineering components, *International Journal of Pressure Vessels and Piping*, 76 (1999) 741–746.
- [20] B.R. You & S.B. Lee, A critical review on multiaxial fatigue assessments of metals, *International Journal of Fatigue*, 18 (1996) 235–244.
- [21] J.W. Ringsberg, Life prediction of rolling contact fatigue crack initiation, *International Journal of Fatigue*, 23 (2001) 575–586.
- [22] A. Zoeteman, R. Dollevoet & Z. Li, Dutch research results on wheel/rail interface management: 2001–2013 and beyond. *Proceedings of the Institution of Mechanical Engineers, Part F: Journal of Rail and Rapid Transit*, 228/6, (2014) 642–651.
- [23] Y. Jiang & H. Sehitoglu, A model for rolling contact failure, *Wear*, 224 (1999) 38–49.
- [24] M. Akama, Development of finite element model for analysis of rolling contact fatigue cracks in wheel/rail systems, Railway Technical Research Institute, Quarterly Reports, 48 (2007).

### Appendix 5.1: The 3D geometry of the internal cracks and measuring the crack angles in all the rail samples

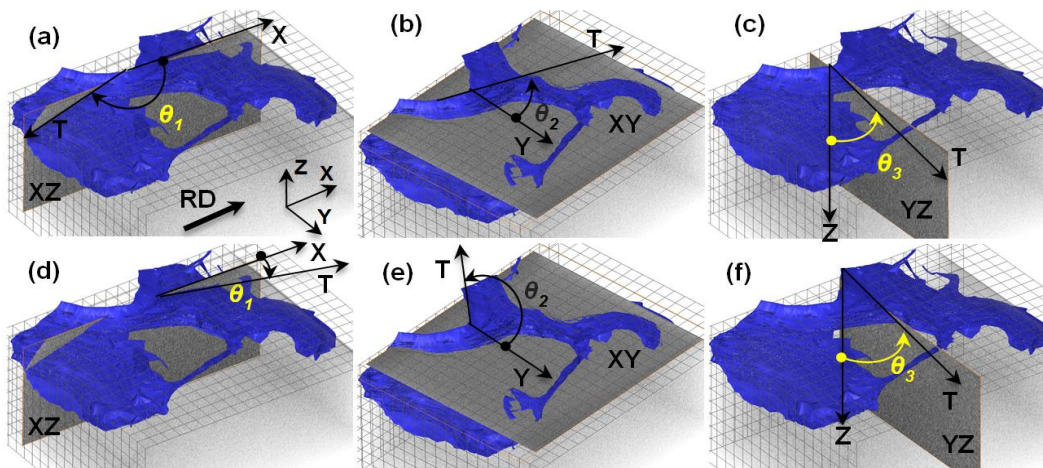


Figure 5.14. Measuring the crack angles of the crack planes in Sample-1. (a, b, c) the angles for C1 and (d, e, f) the angles for C2. Arrow T represents the average tangent line to the crack segments in the rail surface. The angles that are associated with C1 and C2 are shown here as examples.

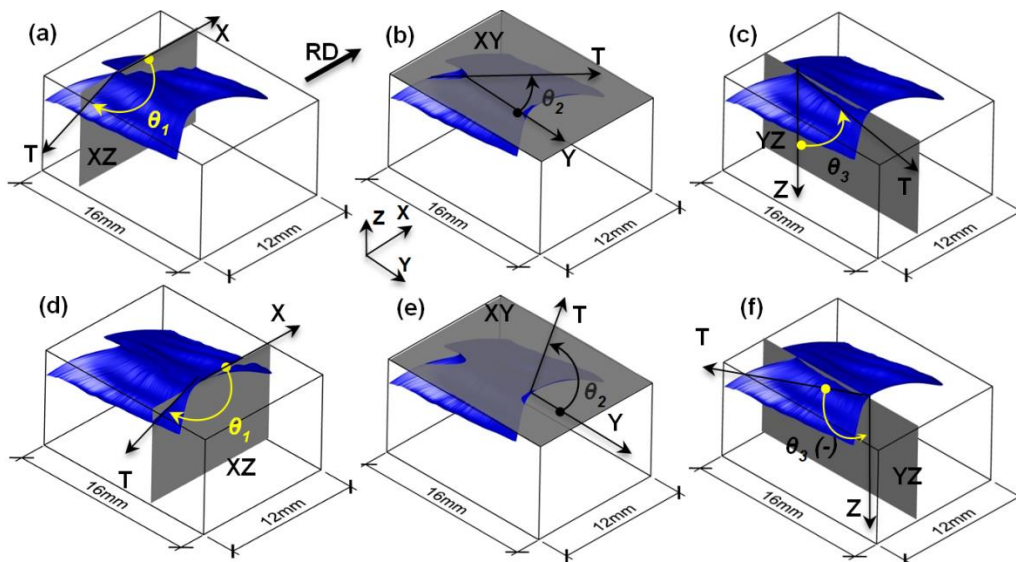


Figure 5.15. Measuring the crack angles in Sample-2. (a, b, c) The angles that are associated with C3 and (d, e, f) the angles that are associated with C1; the crack angles that are associated with C3 and C1 are shown here as examples.

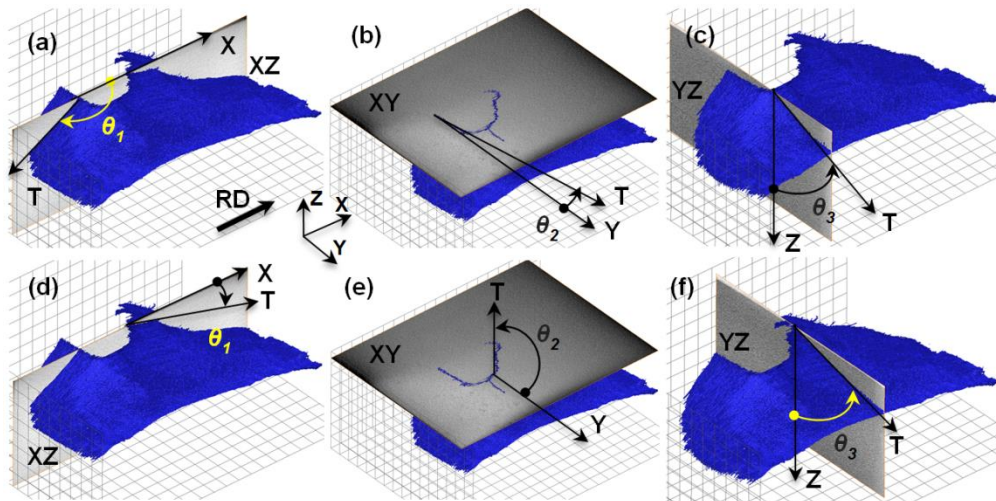


Figure 5.16. Measuring the angles of the crack planes that intersect the rail surface in Sample-3; (a, b, c) the angles for C4 and (d, e, f) the angles for C5; the results for C4 and C5 are presented as examples.

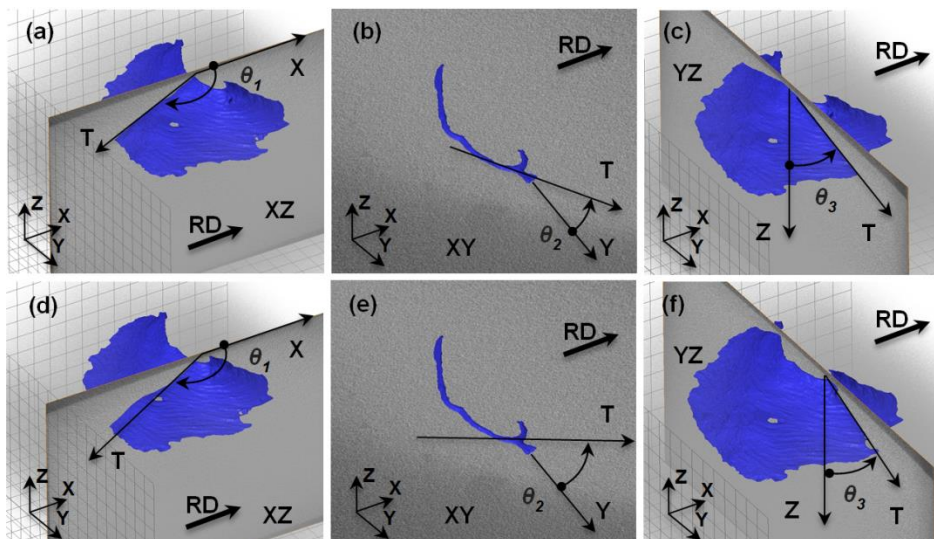


Figure 5.17. Measuring the angles for the crack planes in Sample-4; (a, b, c) the angles for C1 and (d, e, f) the angles for C2

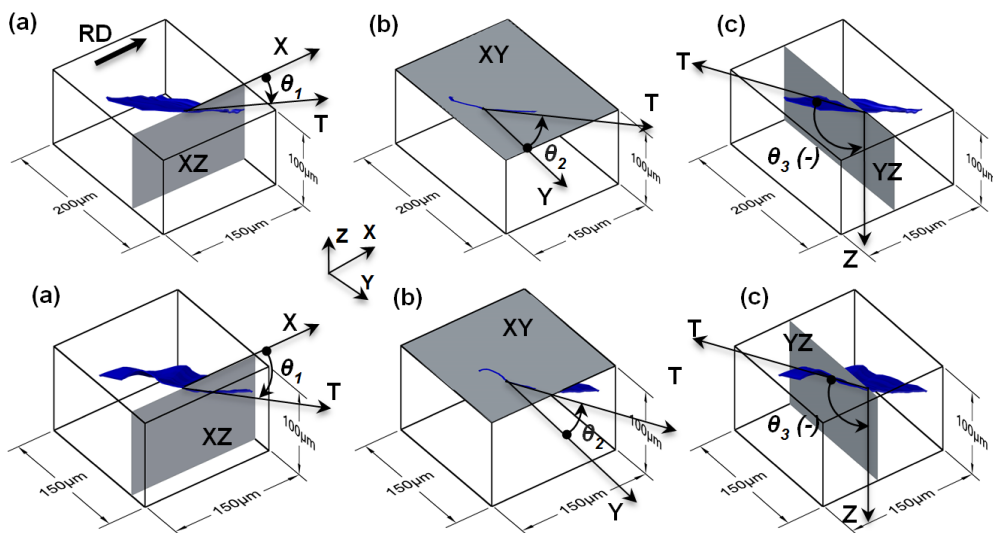


Figure 5.18. Measuring the crack angles for the two tiny cracks in Sample-5; (a, b, c) The angles for C1 and (d, e, f) the angles for C2





# 6

## Chapter 6 Conclusions and recommendations

### 6.1 Conclusions

The research presented in this dissertation has focused on the development of three advanced methods for obtaining a better understanding of the formation mechanism of RCF defects and, more specifically, squats in rails: 1) A new thermomechanical tool for modelling the wheel–rail contact; 2) A new experimental setup for testing the wheel–rail contact and 3) A new computed tomography (CT) procedure for characterizing the wheel–rail defects. The most significant findings from this research are summarized as follows:

- 1) The coupled thermomechanical modelling procedure that is developed in **Chapter 2** was able to predict the temperature in the rail material at the contact interface under various creepage scenarios. TEPS (thermo–elasto–plastic with thermal softening) was the most advanced material model in this research, for which, thermomechanical coupling and temperature–dependency of materials were considered.
- 2) The comparison between the purely mechanical and the coupled thermomechanical solvers revealed that the coupling solver produces higher peak stresses and higher plastic deformations in the rail material. The comparison between the temperature–independent and the thermal–softened materials revealed that thermal softening causes higher von–Mises stresses and higher plastic deformations in materials. Among the different nonlinear material models, TEPS produced the highest equivalent von–Mises stress and the highest plastic deformation. It happened due to the combined effects of thermal softening and thermal coupling, which caused higher thermal stresses. These stresses were superimposed on the mechanical contact stresses and amplified the total stresses. TEPS produced the least flash–temperature (498 °C) in the rail surface. This happened because, in this model, a higher fraction of the total energy contributed to form the high plastic deformation.
- 3) The temperature distribution in the wheel and rail surface consisted of two regions, i.e., a rapid increase in the contact patch and a fast decay in the opposite side of the running direction. The peak occurred near the trailing edge of the contact patch.
- 4) The temperature in the wheel–rail contact was significantly influenced by creepage; for the creepage of 10%, 18% and 26%, the peak temperatures were 284 °C, 498 °C and 756 °C, respectively. The higher creepage increased the flash–temperature (in a significant manner) and residual stresses (to the lower extent), while it had a negligible influence on the peak von–Mises stresses.

- 5) The peak temperature in the rail surface calculated for the 26% creepage (756 °C) was sufficient to transform pearlite to austenite. According to equilibrium quasi-binary iron-carbon phase diagrams, the temperature above 700 °C was considered as the supercritical temperature, at which, the potential of WEL formation via martensitic phase transformation was confirmed. Creepage as high as 26% has been measured with some passenger trains of the Dutch railway and high occurrence of squats have been reported in the rails, on which, these passenger trains being in-service.
- 6) Thermal effects were also important at subcritical temperatures (below 700 °C). Thermal effects, on the one hand, caused a reduction in the elastic and shakedown limits, due to thermal softening. On the other hand, when thermal stresses were superimposed on the mechanical contact stresses, higher stresses and deformations were expected. The results indicated a synchronization effect i.e. the lower yielding limits and higher stresses, which may cause earlier RCF damage.
- 7) The new test rig that is developed in **Chapter 3** was able to help investigate the wheel-rail contact problem under impact-like loading conditions which is suggested to be the case for squats.
- 8) Using transient finite element modelling, it was confirmed that the new test rig can reproduce high-frequency dynamic characteristics of the wheel-track system when a typical w-shape squat is present on the railhead.
- 9) Dynamic effects induced by the presence of a rail joint were properly reflected in both the full-scale system and the downscale test rig. This was confirmed by transient finite element modelling and by test and measurement on the newly built setup.
- 10) After about 41300 preliminary test revolutions of the new test rig, some potential corrugation wave patterns were observed on the railhead, which is considered to be generated by the impact due to the rail joint. The wave pattern of this was in good agreement with those of the real-life systems.
- 11) By performing impact hammer test measurement on a prototype ballasted railway track with the scale of 1:5, the scalability of the dynamic characteristics of the system was confirmed.
- 12) **Chapter 4** revealed the potential of CT as a reliable technology for reconstructing RCF cracks and more specifically squats with complex crack networks under the rail surface. The presence of squat cracks in the studied specimens is detected by CT and the internal crack networks were accurately reconstructed. The CT measurements were validated using metallographic observations of the rail surface cracks. The crack geometries observed by microscopy on the rail surface were nearly identical to the cracks detected by CT, which verified the reliability of the CT observations.
- 13) The quality of the CT measurement for identifying the real geometry of internal cracks was dependent on the CT settings and the sample size. Crack geometries were rebuilt with a high quality in sufficiently small specimens. The advised dimension limits for a cubic specimen of  $W \times L \times D$  is  $W \leq 25$  mm,  $L \leq 40$  mm, and  $D \leq 15$  mm, suggested for the available technological capability of the industrial CT devices.
- 14) The CT was more promising for young squats, i.e., squat Class A, baby squats and initiating squats, as they allow smaller specimens that could cover the entire crack network. Young RCF cracks are within the size limits advised in this research. For squats of classes B and C, it is suggested to divide the rail defect into multiple regions

with sufficiently small dimensions for high-quality CT measurements. This partitioning will also allow mature squats to be measured with significantly high quality.

- 15) The CT technique can be considered as an intermediate detection and characterization tool between the methods for detecting macro cracks (cracks larger than 1 mm) and those for micro/nano cracks (cracks smaller than 10  $\mu\text{m}$ ). When the locations and orientations of the cracks are known by using the CT scan, smaller samples encompassing the internal micro crack network of interest can be prepared. These samples can then be further analysed using advanced crystallographic characterization techniques, such as EBSD, SEM or TEM.
- 16) In **Chapter 5** we were able to successfully reconstruct and measure the complex geometries of crack networks in squats of various severities using CT scanning and metallographic observations. Using the proposed 3D visualization method, including the definitions of crack planes and angles, we were able to define and measure the 3D crack geometries of squats.
- 17) Four crack orientations, namely, T1–T4, were identified and visually demonstrated. The ranges of the characteristic crack angles of the four orientations were measured. The cracks have an angle of  $132^\circ$ – $150^\circ$  relative to the  $X$ -axis ( $\theta_1$ ). The angle in the rail surface relative to the  $Y$ -axis ( $\theta_2$ ) was in the range of  $6^\circ$ – $36^\circ$ . In the rail vertical–longitudinal cross–section, the angle of the crack relative to the  $Z$ -axis ( $\theta_3$ ) was in the range of  $67^\circ$ – $81^\circ$ . These findings were in agreement with angle predictions by other researchers and with the field monitoring results.
- 18) The occurrence frequencies of the orientations were calculated for the samples, based on which, it was found that orientations T4 and T1 together form a V-shaped (or U-shaped) peninsula, which is the primary crack of squats. T2 and T3 together form V-shaped secondary cracks.
- 19) The crack angles calculated by the FE modelling were in agreement with the experimental observations. The angle types T2, T3 and T4 seem to correspond to braking, traction and free rolling loading, respectively. This indicates that the crack initiation angle depends on the loading conditions.
- 20) Based on this research, the main new insights into the formation of rail squats are as follows: i) the WEL formation via martensitic phase transformation turned out to be possible; this was confirmed through the thermomechanical wheel–rail contact modelling; ii) the impact–like loading conditions and high–frequency dynamic characteristics of the wheel–track system appeared to be essential for the squat formation; this was confirmed through the vehicle–track testing using the new test rig; and iii) the occurrence of different crack orientations followed by the primary and secondary V-shaped cracks turned out to be important in the squat formation; this was confirmed through the CT scanning and metallographic observations.

## 6.2 Recommendations

Besides the insights into the squat formation presented in this dissertation, the following aspects are recommended to be further investigated to better understand the causes of the squat damage formation and development:

- 1) It is recommended to experimentally investigate the possibility of high temperature (adequate for the martensitic transformation) in the contact interface of the wheel–rail materials. Besides validation of the presented thermomechanical model, such study can also experimentally verify under which operational and contact conditions e.g. creepage, speed, friction etc. the high temperature can occur.
- 2) In the current model, developed with ANSYS/LS–DYNA, the user has to provide values for the main parameters (Young's modulus, hardening modulus, Poisson's ratio, yield strength and the coefficient of thermal expansion) at various temperatures. The modelling of plasticity using advanced plasticity models of materials is not yet incorporated. This is considered as recommendation for the future research in order to make the modelling tool more advanced and realistic.
- 3) Modern locomotives and motorised wagons with advanced slip/spin control systems have, in general, a better traction/creepage performance. It is recommended to investigate the amount of creepage between the wheel and rail by the operation of such trains. It would be interesting to investigate the occurrence frequency of squats in the tracks where these trains operate.
- 4) The new test rig developed in this research can be equipped with the high precision temperature sensors to measure the flash temperature in the wheel–rail materials. However, measuring the temperature at or very close to the contact patch will be a challenge.
- 5) It is recommended to compare the microstructures of the potential RCF defects generated by the test rig and of the real defects to verify that the test rig can indeed generate defects representative of real-life RCF.
- 6) Quantitative analysis of the WEL formation and squat initiation is recommended. The high temperature and the mentioned synchronization effect can explain the formation of WEL but not necessarily the initiation of squat defects. To verify this, quantitative research using microstructural observations of the rails with squat defects is needed.
- 7) It is recommended to study of the possible formation of WEL and RCF defects by laboratory simulations using the new test rig. Various wheel–rail material grades and various contact geometries can be tested. Comparing the RCF performance of pearlitic and bainitic rail steels in terms of WEL formation and crack initiation in the lab environment using the new test rig will provide insightful evidence.
- 8) Developing mobile CT scanners (e.g. mounted on a train and operated by a robot) to detect and measure potential rail damage looks to be ambitious but not unfeasible.
- 9) The crack angles calculated by the FE modelling are related to the loading conditions. Further investigation on the loading conditions that are used in the FE models and the potential links to the crack types, angles and geometries will provide insightful evidence on the formation mechanism and the nature of RCF defects.

- 10) It is recommended to investigate the influence of microstructure and stress fields on the initial crack growth directions. It would be interesting to model the RCF cracks using 3D approaches for modelling of the rail steel microstructure based on the geometrical data of RCF cracks obtained by CT scanning. This investigation can simulate the early stages of RCF crack growth and can address the combined effect of microstructure and loading on crack growth rates and angles. When the loading behaviour of the rail is adapted with the microstructure model, the residual stresses e.g. at the top surface of the rail can also be incorporated in the crack growth predictions.
- 11) It is recommended to address the remaining life of defective rails by investigating the crack propagation angles and directions and by predicting the rail fatigue life through advanced modelling, characterization and testing methods. Using the new test rig, it is possible to perform simultaneous tests of different loading, geometry, construction and materials under controlled and repeatable conditions in order to trace back the total life of RCF defects from initiation to (almost) fracture. Sample defects at various development phases can be investigated using CT scan and metallography to measure the size, angles and directions of crack developments. Numerical simulations can, next to these, predict the crack propagation rates, angles and directions.



## Curriculum Vitæ

### Meysam Naeimi

03-02-1985

Born in Tehran, Iran



### Education

2013 – 2017

PhD, Delft University of Technology, Civil engineering  
Dissertation: “An investigation into the formation of squats in rails: modelling, characterization and testing”

2007 – 2009

MSc, Iran University of Science & Technology (IUST), Railway Track Engineering  
Dissertation: “Dynamic response of sleepers in railway track”

2003 – 2007

BSc, Iran University of Science & Technology (IUST), Railway Track and Structures Engineering  
Dissertation: “Evaluation of railway bridge superstructures”

### Experience

2020 – present

Senior Inspector Rail, Inspectie Leefomgeving en Transport (ILT)

2019 – 2020

Consultant Railway Infrastructure, Royal HaskoningDHV

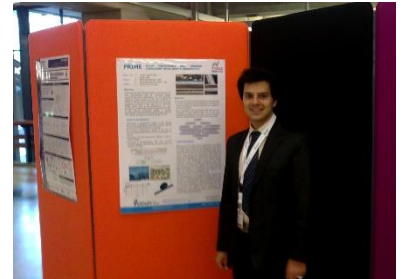
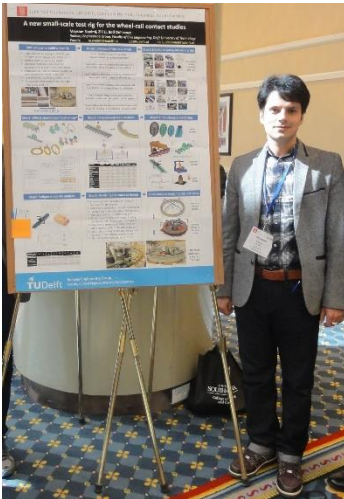
2017 – 2019

Specialist Civil, Mechanics & Certification, DEKRA Rail bv.

2009 – 2013

Civil Engineer (Railways & Structures), HEXA Co.





The jury of RailTech 2015 Young Innovation Award herewith confirms that

*TU Delft – A novel test rig for wheel-rail contact studies*

**Meysam Naeimi**  
was awarded

**2<sup>nd</sup> place**

at the

**RailTech 2015**  
**Young Innovation Award competition**

on 19 March 2015  
at The Royal Jaarbeurs Utrecht

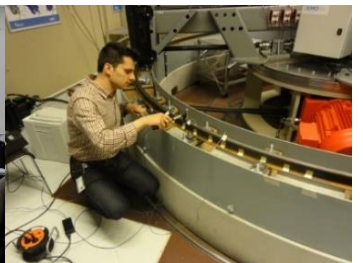
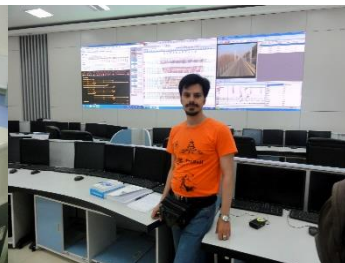


**Some highlights during PhD study at TU Delft, date of photos 2013-2017**



**EUROPOINT**  
Rail Technology  
Conferences & Exhibitions

**ProMedia**  
group.nl



## List of Publications

### Journal Papers

[J1] M. Naeimi, S. Li, Z. Li, J. Wu, R.H. Petrov, J. Sietsma & R. Dollevoet, Thermomechanical analysis of the wheel–rail contact using a coupled modelling procedure, *Tribology International*, 117 (2018) 250–260.

[J2] M. Naeimi, Z. Li, R.H. Petrov, J. Sietsma & R. Dollevoet, Development of a new downscale setup for wheel–rail contact experiments under impact loading conditions, *Experimental Techniques*, 42 (2017) 1–17.

[J3] M. Naeimi, Z. Li, Z. Qian, Y. Zhou, J. Wu, R.H. Petrov, J. Sietsma & R. Dollevoet, Reconstruction of the rolling contact fatigue cracks in rails using X–ray computed tomography, *NDT & E International*, 92 (2017) 199–212.

[J4] M. Naeimi, Z. Li & R. Dollevoet, Determining the angles of squat cracks via CT scanning and metallographic observations, *Engineering Fracture Mechanics* 230 (2020) 107016.

### Collaboration journal papers

[J5] J. Wu, R.H. Petrov, M. Naeimi, Z. Li, R. Dollevoet & J. Sietsma, Laboratory simulation of martensite formation of white etching layer in rail steel, *International Journal of Fatigue*, 91 (2016) 11–20.

[J6] A. Jamshidi, Z. Su, S. Hajizadeh, M. Naeimi, A. Núñez, R. Dollevoet, B. De Schutter & Z. Li, A decision support approach for condition–based maintenance of rails based on big data analysis”. *Transportation Research Part C: Emerging Technologies*, 95 (2018) 185–206.

### Conference papers

[C1] M. Naeimi, Z. Li & R. Dollevoet, Computation of stress intensity factors in an initiating RCF crack using a 3D modelling approach, in: *Proceedings of the First International Conference on Rail Transportation, China, Chengdu, 2017*.

[C2] M. Naeimi, Z. Li, R. Dollevoet, J. Wu, R. Petrov & J. Sietsma, Thermo–mechanical effects in the formation mechanism of rail squats, in: J. Pombo (Ed.) *Proceedings of the Third International Conference on Railway Technology: Research, Development and Maintenance*, Civil–Comp Press, Stirlingshire, UK, 2016.

[C3] M. Naeimi, Z. Li & R. Dollevoet, A new small–scale test rig for the wheel–rail contact studies, poster presentation, *Joint Rail Conference (JRC 2016)*, Columbia, South Carolina, 2016.

[C4] M. Naeimi, Z. Li & R. Dollevoet, Nucleation of squat cracks in rail, calculation of crack initiation angles in three dimensions, in: *Journal of Physics: Conference Series*, IOP Publishing, 2015, 012043.

- [C5] M. Naeimi, Z. Li, R. Dollevoet, J. Wu, R. Petrov & J. Sietsma, Computation of the flash-temperature at the wheel-rail contact using a 3D finite element model and its comparison with analytical methods, in: Proceedings of the 10th International Conference on Contact Mechanics (CM 2015), Colorado Springs, Colorado, USA, 2015.
- [C6] M. Naeimi, Z. Li & R. Dollevoet, Preliminary results on dynamic analysis of a new test rig for wheel-rail contact studies, in: Proceedings of the 4th International Conference on Recent Advances in Railway Engineering (ICRARE2015), Tehran, Iran, 2015.
- [C7] M. Naeimi & R. Dollevoet, Preliminary results on multi-body dynamic simulation of a new test rig for wheel-rail contact, *Advances in Railway Engineering, An International Journal*, 3 (2015) 27–37.
- [C8] M. Naeimi, Z. Li & R. Dollevoet, Scaling strategy of a new experimental rig for wheel-rail contact, *International Journal of Mechanical, Aerospace, Industrial and Mechatronics Engineering*, 8 (2014) 1787–1794.
- [C9] M. Naeimi, Z. Li, R. Petrov, R. Dollevoet, J. Sietsma & J. Wu, Substantial fatigue similarity of a new small-scale test rig to actual wheel-rail system, *International Journal of Mechanical, Aerospace, Industrial and Mechatronics Engineering*, 8 (2014) 1795–1803.
- [C10] J. Wu, R. Petrov, M. Naeimi, Z. Li & J. Sietsma, A microstructural study of rolling contact fatigue in rails, in: J. Pombo (Ed.) Proceedings of the Second International Conference on Railway Technology: Research, Development and Maintenance, Civil-Comp Press, Ajaccio, France, 2014.
- [C11] X. Deng, M. Naeimi, Z. Li, Z. Qian & R. Dollevoet, Residual fatigue life evaluation of rail at squats seeds using 3D explicit finite element analysis, in: AMS 14: Proceedings of the 1st Ageing of Materials & Structures Conference, DCMat Ageing Centre, Delft University of Technology, Delft, The Netherlands, 2014.
- [C12] A. Jamshidi, S. Hajizadeh, M. Naeimi, A. Nunez & Z. Li, Influencing factors for condition-based maintenance in railway tracks using knowledge-based approach, in: Proceedings of the First International Conference on Rail Transportation, China, Chengdu, 2017.

# **Propositions**

Accompanying the dissertation

## **An investigation into the formation of squats in rails: modelling, characterization and testing**

by

**Meysam Naeimi**

1. Rolling contact fatigue in rails needs multidisciplinary contact mechanics, material science as well as thermodynamics to understand and to synergize so as to solve.  
("This proposition pertains to this dissertation.")
2. The mechanical wheel-rail contact problem looks like kung fu and taekwondo; the thermo-mechanical contact resembles wrestling.  
("This proposition pertains to this dissertation.")
3. No high rail temperature, less squat occurrence.  
("This proposition pertains to this dissertation.")
4. The three steps to new products are to see/learn at a producer, to innovate in laboratory, and to test in practice.
5. Learn from other fields (even if they may seem irrelevant) for solutions to your problems.
6. Hard-working is important to complete a doctoral research; creativity and innovation make it distinctive.
7. When a route in research is identified to be closed, publish even the negative results and limitations to help others.
8. Even if you prefer to stay in academia as a scientist, learn engineering and design skills.
9. You don't have to be an expert in all the involved disciplines of the research, collaborate well.
10. It is vital to speak the local language of the place where you study.

These propositions are regarded as opposable and defendable, and have been approved as such by the promoters Prof.dr. Z. Li and Prof.dr.ir. R.P.B.J. Dollevoet.

